



HAL
open science

Development of Accurate Dosimetry for Microbeam Radiation Therapy

Dimitri Reynard

► **To cite this version:**

Dimitri Reynard. Development of Accurate Dosimetry for Microbeam Radiation Therapy. Bioengineering. Université Grenoble Alpes; University of Swansea (Swansea (GB)), 2018. English. NNT : 2018GREAS038 . tel-02418662

HAL Id: tel-02418662

<https://theses.hal.science/tel-02418662>

Submitted on 19 Dec 2019

HAL is a multi-disciplinary open access archive for the deposit and dissemination of scientific research documents, whether they are published or not. The documents may come from teaching and research institutions in France or abroad, or from public or private research centers.

L'archive ouverte pluridisciplinaire **HAL**, est destinée au dépôt et à la diffusion de documents scientifiques de niveau recherche, publiés ou non, émanant des établissements d'enseignement et de recherche français ou étrangers, des laboratoires publics ou privés.



THÈSE

Pour obtenir le grade de

DOCTEUR DE LA COMMUNAUTÉ UNIVERSITÉ GRENOBLE ALPES

Spécialité : BIS - Biotechnologie, instrumentation, signal et imagerie pour la biologie, la médecine et l'environnement

Arrêté ministériel : 25 mai 2016

Présentée par

Dimitri REYNARD

Thèse dirigée par **François ESTEVE**, Communauté Université Grenoble Alpes

et codirigée par **Richard HUGTENBURG**

et **Elke BRAUEUR-KRISCH**

préparée au sein du **Laboratoire Rayonnement Synchrotron et Recherche Médicale**

dans **l'École Doctorale Ingénierie pour la santé la Cognition et l'Environnement**

Développement d'une dosimétrie précise pour la radiothérapie par micro faisceaux

Development of Accurate Dosimetry for Microbeam Radiation Therapy

Thèse soutenue publiquement le **27 novembre 2018**,
devant le jury composé de :

Madame JENNY SPIGA

PROFESSEUR ASSOCIE, UNIVERSITE DE WARWICK - GRANDE BRETAGNE, Rapporteur

Monsieur JAMES CRONIN

PROFESSEUR ASSOCIE, UNIVERSITE DE SWANSEA AU PAYS DE GALLES, Président

Monsieur DANIEL SANTOS

DIRECTEUR DE RECHERCHE, CNRS DELEGATION ALPES, Examineur

Monsieur ALBERT E. SIEGHAN

PROFESSEUR ASSOCIE, UNIV-INSTITUT KAROLINSKA A STOCKHOLM, Rapporteur

Madame KEN MEISSNER

PROFESSEUR, UNIVERSITE DE SWANSEA AU PAYS DE GALLES, Examineur



Prifysgol Abertawe
Swansea University



THESIS

Submitted to

**SWANSEA UNIVERSITY and UNIVERSITÉ
GRENOBLE ALPES**

**In fulfilment of the requirements for the Degree of
Doctor of Philosophy**

Field : **Medical Physics, Biotechnologie instrumentation,
signal**

Presented by

Dimitri D.H. REYNARD

Directors **Richard P. HUGTENBURG** and **François ESTÈVE**
Co-Directors **Ihsan AL-AFFAN** and **Elke BRAUER-KRISCH**
Prepared in the **Medical Physics Department** and the **EA 7442
RSRM - ID17 /ESRF-CLUNI**

In the **College of Medicine** and **l'École Doctorale d'Ingénierie
pour la Santé, la Cognition et l' Environnement**

Accurate dosimetry for microbeam radiation therapy

Thesis defended in **2018**,
Before a jury composed of :

Dr Jenny SPIGA

Associate professor, University of Warwick, external examiner

Pr Gareth J. JENKINS

Professor , Swansea University, internal examiner

Pr Daniel SANTOS

Research director, LPSC, Université Grenoble Alpes, internal examiner



Declaration

I hereby declare that except where specific reference is made to the work of others, the contents of this dissertation are original and have not been submitted in whole or in part for consideration for any other degree or qualification in this, or any other university. This dissertation is my own work and contains nothing which is the outcome of work done in collaboration with others, except as specified in the text and Acknowledgements. This dissertation contains fewer than 47,000 words including appendices, bibliography, footnotes, tables and equations and has fewer than 55 figures.

Dimitri Reynard
September 2018

Abstract

Microbeam Radiation Therapy (MRT) is an emergent treatment modality that uses spatially fractionated synchrotron x-ray beams. MRT has been identified as a promising treatment concept that might be applied to patients with malignant central nervous system (CNS) tumors for whom, at the current stage of development, no satisfactory therapy is available yet. The use of a fractionated beam allows a better skin sparing and a better tolerance of healthy tissue to high dose rates. MRT consists of a stereotactic irradiation with highly collimated, quasi-parallel array of narrow beams 50 μm wide spaced with 400 μm made of synchrotron generated x-rays at an energy ranging from 0 to 600 keV [1]. The European Synchrotron Radiation Facility (ESRF) as an x-ray source allows a very small beam divergence and an extremely high dose rate. The dose deposited on the path of the primary photons (peak dose) of several hundred grays (Gy) is well tolerated by normal tissues and provides at the same time a higher therapeutic index for various tumor models in rodents. The high dose rate forces us to develop an accurate and reproducible dosimetry protocol to ensure the matching between the prescribed and the delivered dose. MRT is by definition a non-conventional irradiation method, therefore the number of dosimetric errors becomes larger than in conventional treatments due to two reasons (i) the reference conditions recommended by the Association of Physicists in Medicine (AAPM) or the International Atomic Energy Agency (IAEA) cannot be established, (ii) the measurement of absorbed dose to water in composite fields is not standardized.

This PhD is focused on bridging the gap between MC simulated values of output factors (OF) and peak-to-valley dose ratios (PVDR) and experimental measurements. Several aspects of the irradiation setup such as insertion devices on the path of the x-ray beam are accounted for as well as the internal structure of the dosimeters. Each contribution to OF and PVDR is quantified to correct for the measurements.

Preface

This thesis is divided into 4 chapters. The motivations that led to the idea of Microbeam Radiation Therapy (MRT) are presented as follows:

Chapter 1 introduces the MRT project in terms of technique and scientific outputs. Emphasis is put on the technical aspects of MRT as well as SSRT for which a scientific paper has been published in 2018 and addressed in Annexe A.

Chapter 2 presents the Monte Carlo technique in general before focusing on the radiation transport specificities. Issues related to calculation time are presented along with solutions to overcome this issue. A benchmark of three widely used MC codes is presented, with a particular attention on the calculation of OF and PVDR in MRT reference conditions.

Chapter 3 presents a benchmark of three dosimeters, the PTW microDiamond detector, HDV2 films and fluorescent nuclear track detectors for the measurement of the PVDR in MRT reference conditions. The observation of the result lead to two different studies of potential phenomenon that influence the dosimetry; the total reflection on the inner surfaces of the multislit collimator and the wobble of the goniometric table.

Chapter 4 presents a method to quantify and correct dose measurements for effects due to the intrinsic geometry and material composition of a dosimeter. This method is applied to the HDV2, FNTD and microDiamond. Finally, the influence of the presence of the MSC, the air and several other inserted devices on the path of the primary photons, is quantified and combined with previously found results to bridge the gap between MC simulations and experimental measurements.

This PhD is part of the MRT project and aims at improving the experimental dosimetry or the existing protocol. To that end, experimental dosimetry studies along with Monte-Carlo (MC) simulations are performed to improve the understanding of the beam characteristics and the accuracy of the modelling of such techniques.

Contents

| | |
|---|-------------|
| List of Figures | VIII |
| List of Tables | XI |
| 1 Introduction | 1 |
| 1.1 Motivations | 1 |
| 1.2 Microbeam Radiation Therapy | 2 |
| 1.2.1 Dose Volume Effect | 2 |
| 1.2.2 MRT technique | 3 |
| 1.3 MRT preclinical results | 5 |
| 1.4 Optimization of the MRT parameters | 8 |
| 1.4.1 Microbeam c-t-c spacing | 8 |
| 1.4.2 Microbeam width | 8 |
| 1.5 Dosimetry | 9 |
| 1.5.1 Reference Dosimetry in MRT | 13 |
| 1.5.2 Relative Dosimetry | 14 |
| 1.6 Synchrotron Source | 15 |
| 1.6.1 ID 17 MRT beam line characteristics | 17 |
| 1.6.2 MRT experimental hutch | 20 |
| 1.6.3 SSRT experimental hutch | 21 |
| 1.7 Project overview | 22 |
| 1.8 Project Aims | 23 |
| 1.9 Challenges | 24 |
| 1.10 Introduction of the PTW microDiamond | 26 |
| 2 Monte Carlo Simulations | 28 |
| 2.1 Introduction of Monte Carlo simulations | 28 |
| 2.2 Monte Carlo in radiation transport | 29 |
| 2.2.1 Random Sampling Methods | 30 |
| 2.2.1.a The inverse-transform method | 30 |
| 2.2.2 Geometry description | 32 |
| 2.2.3 Cross-section data | 33 |
| 2.3 Time issue in MC simulations | 33 |
| 2.3.1 Speed-up through the geometry | 35 |

| | | |
|----------|--|-----------|
| 2.3.1.a | Applying Semi-adjoint MC simulation in MRT . . . | 35 |
| 2.3.1.b | Adapting the geometry and particle cut-offs | 38 |
| 2.3.2 | Speed-up by mimicking the scanned irradiation | 38 |
| 2.3.3 | Speed-up through the Parallelization of PENELOPE | 40 |
| 2.3.3.a | Structure of the parallel code | 41 |
| 2.3.3.b | Parallelization of the PENMAIN subroutines | 42 |
| 2.3.3.c | Parallelization of the Main Program PENMAIN . . | 43 |
| 2.3.4 | Quantification of speed enhancement | 45 |
| 2.3.5 | Particle splitting simulations | 47 |
| 2.4 | Benchmark of the MC codes | 49 |
| 2.4.1 | Material and methods | 50 |
| 2.4.2 | Results | 52 |
| 2.4.3 | Discussion | 56 |
| 2.4.4 | Conclusion | 57 |
| 3 | Simulation vs Experiment | 58 |
| 3.1 | Dosimeter Benchmark | 58 |
| 3.1.1 | Material and Methods | 58 |
| 3.1.2 | Results | 59 |
| 3.1.3 | Conclusion | 60 |
| 3.2 | Study of Potential Total Reflection on Inner Surfaces of the MSC | 61 |
| 3.2.1 | Motivation and Preliminary study | 61 |
| 3.2.2 | Modelling | 64 |
| 3.2.3 | Geometry | 65 |
| 3.2.4 | Results | 66 |
| 3.3 | Wobble study | 67 |
| 3.3.1 | Extraction of the Wobble | 68 |
| 3.3.2 | Wobbling source model for MC simulations | 70 |
| 3.3.3 | Impact of the wobble on dosimetric quantities | 73 |
| 3.3.3.a | Methods | 73 |
| 3.3.3.b | Results | 74 |
| 3.3.4 | Conclusion | 75 |
| 4 | Application of the Bouchard method on dosimeters | 76 |
| 4.1 | Bouchard Method | 76 |

| | | |
|----------|---|------------|
| 4.2 | Bouchard on films and FNTD | 79 |
| 4.2.1 | Methods | 79 |
| 4.2.2 | Results | 81 |
| | 4.2.2.a HDV2 films | 81 |
| | 4.2.2.b FNTD | 83 |
| | 4.2.2.c Conclusion | 84 |
| 4.3 | Bouchard on PTW microDiamond | 85 |
| 4.3.1 | Methods | 85 |
| 4.3.2 | Results | 86 |
| 4.3.3 | Conclusion | 88 |
| 4.4 | Bridging the gap between MC and experiments | 89 |
| 4.4.1 | Methods | 89 |
| 4.4.2 | Results | 91 |
| 5 | Conclusion | 94 |
| 6 | Scientific production | 98 |
| 7 | Résumé du travail de thèse en français | 99 |
| 7.1 | Contexte du projet de thèse | 99 |
| 7.1.1 | Challenges | 100 |
| 7.1.2 | Présentation du microDiamond | 102 |
| 7.2 | Présentation des principaux résultats | 103 |
| 7.2.1 | Comparaison des principaux codes MC utilisés en MRT | 103 |
| 7.2.2 | Influence de l'oscillation de la table goniométrique sur la dosimétrie | 104 |
| 7.2.3 | Quantification de l'influence du détecteur et des éléments sur le trajet du faisceau sur la dosimétrie | 105 |
| 7.3 | Conclusion | 107 |
| | References | 111 |
| | Appendices | 122 |
| A | Towards <i>in vivo</i> dosimetry for contrast enhanced synchrotron stereo- tactic radiation therapy based on iodine x-ray spectroscopy | 123 |
| B | Flow chart for the Parallelized Penelope | 136 |

List of Figures

| | | |
|----|--|----|
| 1 | Histological images of a mouse brain irradiated with a 22.5 MeV deuterium beam. On the left image, the mouse brain tissue, irradiated with a 1 mm diameter beam and an entrance dose of 280 Gy (120-day post-irradiation), is completely destroyed while on the right image the tissue irradiated with a 25 μm beam and an entrance dose of 4000 Gy is preserved (28-day post-irradiation) [2]. | 3 |
| 2 | Beam collimation using two MSC's to adjust microbeams width [3] | 4 |
| 3 | Simulated absorbed dose at 2 cm depth for CRT and MRT | 5 |
| 4 | Histological images of a piglet brain 15 months after MRT irradiation with a skin dose of 300 Gy [4]. | 7 |
| 5 | Photoelectric absorption [5] | 10 |
| 6 | Compton scattering [5] | 11 |
| 7 | Rayleigh scattering [5] | 12 |
| 8 | Pair production [5] | 13 |
| 9 | Definition of OF and PVDR. | 15 |
| 10 | Diagram of a synchrotron. | 16 |
| 11 | Bending magnet(left) and insertion device(right) | 16 |
| 12 | ID 17 medical beam line. The optical hutch is located in the experimental hall. A tunnel connects the MRT hutch to the satellite building where the SSRT is performed. | 18 |
| 13 | MRT optical hutch. | 19 |
| 14 | Design of the fast shutter [6]. | 20 |
| 15 | Technical drawing of the MRT hutch [6] and the associated picture. | 21 |
| 16 | Technical drawing of the MSC [7]. | 21 |
| 17 | Patient positioning system in SSRT. The field is conformed by cerobend masks and the flux is monitored by two plate IC. | 22 |
| 18 | Single microbeam measured with the PTW microDiamond detector. The asymmetry in the lateral dose gradient and the inclined top are the due to the non-sensitive components in the detector. | 25 |
| 19 | High resolution radiograph of the internal structure of the microDiamond [8]. | 27 |
| 20 | Random sampling using the inverse transform method [5] | 31 |
| 21 | Water interaction cross sections [9] | 34 |
| 22 | Comparison forward calculation/ semi-adjoint theorem [10] | 36 |

| | | |
|----|--|----|
| 23 | OF versus microbeam width calculated with the semi-adjoint MC. | 37 |
| 24 | Diagram of cut-off repartitions in a target media. Cut-offs are decreased with distance to the sensitive volume | 39 |
| 25 | Integrated PVDR over 2 cm from an irradiation with a 0.52 mm high beam and central profile from a 2 cm high beam irradiation | 40 |
| 26 | Diagram of the PTW microDiamond detector displayed from PENGEOM. jar | 46 |
| 27 | FOM for enhanced MC simulation normalized to the full simulation. | 47 |
| 28 | ID 17 medical beamline MRT polychromatic spectrum | 51 |
| 29 | PVDR and OF versus depth for EGSnrc, Geant4 and Penelope | 54 |
| 30 | Dose profile at 2 cm depth compared to EGSnrc. | 55 |
| 31 | Central microbeams obtained for three different rotation angles of the MSC (-0.02°, 0° and 0.02°) [11]. | 61 |
| 32 | Particle orientation at the entrance of the PMMA tank. The red curve represents photons that underwent a Rayleigh interaction. | 63 |
| 33 | Energy fluence at the entrance of the PMMA dosimetric tank after tilted MSC (natural logarithm scale). | 64 |
| 34 | Irradiation geometry used in the python script. | 65 |
| 35 | Single box acting as a component of the MSC. Inside the box the material is set as tungsten carbide. Each box is spaced with 50 μm to build up the MSC. | 66 |
| 36 | Left and Right microbeam within the field. | 67 |
| 37 | Wobble of the goniometric table noticeable on the Gafchromic film (scan speed 93 mm/s) | 68 |
| 38 | Gafchromic film image cleaned with successive image opening, median filter and Gaussian filter | 69 |
| 39 | Cleanest microbeam isolated with extracted profile | 70 |
| 40 | Fourier Transform of the 93 mm/s wobble | 71 |
| 41 | Modelled and measured microbeams for scan speed 93, 90.6, 46, 23 mm/s from left to right. | 73 |
| 42 | Fluctuation of the measurement of OF and PVDR with scan speed due to the oscillation of the goniometric table. | 75 |
| 43 | Series of MC simulations to extract perturbation factors. | 78 |
| 44 | Configuration of the Gafchromic HDV2. | 80 |

| | | |
|----|---|-----|
| 45 | Single microbeam in HDV2 and water at 2 cm depth. | 81 |
| 46 | Single microbeam in FNTD and water at 2 cm depth. | 83 |
| 47 | 2cm depth dose profile in water and with the microDiamond. | 86 |
| 48 | Ratio of doses in water and diamond. | 87 |
| 49 | microDiamond sensitive volume at the edges of the irradiation field. | 89 |
| 50 | Geometry of the experimental hutch adapted from Martinez-Rovira and al [12]. | 90 |
| 51 | Single microbeam measured with the PTW microDiamond detector. The asymmetry in the lateral dose gradient and the inclined top are the due to the non-sensitive components in the detector. | 101 |
| 52 | Radiographie à haute résolution de la structure interne du microDiamond. [8]. | 102 |
| 53 | Fluctuation de la mesure de l'OF et du PVDR avec la vitesse de balayage due à l'oscillation de la table goniométrique.Fluctuation of the measure- ment of OF and PVDR with scan speed due to the oscillation of the goniometric table. | 105 |
| 54 | Flow Chart for Parallelized PENELOPE | 136 |

List of Tables

| | | |
|----|--|-----|
| 1 | Comparison between linear accelerator and synchrotron irradiation specificities. | 5 |
| 2 | Irradiation conditions in Slatkin's study. | 6 |
| 3 | ID 17 Wiggler characteristics | 17 |
| 4 | PTW microDiamond detector specificities. | 26 |
| 5 | Percentage difference between OF and PVDR at 2 cm depth in water and bone with EGSnrc as a gold standard | 53 |
| 6 | HD-V2 films specifications | 59 |
| 7 | PVDR measurement with 3 different dosimeters and comparison with expected MC simulated values. | 60 |
| 8 | PVDR and OF calculated in HDV2 films and water | 82 |
| 9 | Correction factors for absolute dose measurements in HDV2 compared to water. | 82 |
| 10 | PVDR and OF calculated in FNTD films and water | 84 |
| 11 | Correction factors for absolute dose measurements in FNTD compared to water. | 84 |
| 12 | PVDR and OF calculated in microDiamond and water | 88 |
| 13 | Correction factors for absolute dose measurements in microDiamond compared to water. | 88 |
| 14 | Summarize of all the different effect quantified in this work and the associated magnitudes. | 92 |
| 15 | PTW microDiamond detector specificities. | 102 |
| 16 | Résumé de tous les différents effets quantifiés dans ce travail et les grandeurs associées. | 106 |

1 Introduction

1.1 Motivations

Radiation therapy (RT) is a treatment modality using ionizing radiation, it is often part of a cancer treatment aiming to kill or reduce the number of malignant cells. According to the *Cancer Research UK*, about 4 out of 10 people with cancer (40%) have radiotherapy as part of their treatment. A major modality for treatment involves X-rays generated with a linear accelerator. The healing power of RT lies in the fact that the X-rays damage the DNA within the tumour cells. Although normal cells are also affected by radiation upstream and downstream of the tumour, they mend more efficiently than cancer cells.

In some cases, tumours can exhibit a certain resistance to X-rays and make conventional treatments at the hospital ineffective. Many alternatives to conventional radiation therapy (CRT) have been developed in the past few decades in order to improve the therapeutic index for such tumours. For instance, proton sources and heavy ion beams are available for treatments and synchrotron generated X-rays for medical purposes are still under development.

Synchrotron Stereotactic Radiation Therapy (SSRT) and Microbeam Radiation Therapy (MRT) are new RT treatment modalities that are being developed at the European Synchrotron Radiation Facility (ESRF) on the ID 17 Medical Beamline. MRT highlights some major differences compared to CRT treatments. The field is spatially fractionated in an array of narrow microbeams by the means of a multi-slit collimator (MSC) placed between the source and the patient. The main idea in MRT is to achieve a very high dose deposition on the path of primary photons (peak dose) and keep the valley dose build up by Compton scattering under the tissue tolerance. Because possible movements of the patient, even cardio synchronous brain motion could lead to deleterious effects, the dose must be delivered in a fraction of a second. In order to achieve this, very steep dose gradient is needed, so the energy range is about 0–600 keV compared to 1–20 MeV in CRT techniques. MRT also demands high dose rates, which can only be provided by an X-ray synchrotron currently.

SSRT, on the other hand, does not require a high dose rate but a monochromatic beam (80 keV) and the intravenous injection of an iodine-based contrast agent (commonly used for imaging techniques). The therapeutic power of SSRT lies in the fact that the iodine selectively leaks into the tumour due to the locally permeabilized blood brain barrier (BBB) [13]. The combination of the contrast agent (high Z) together with the stereotac-

tic irradiation produces a gradient in the absorption cross-section leading to an increased dose deposition [14]. A differential effect is produced between the tumour and the healthy tissue depending on the iodine uptake leading to a difference in the photon interaction mechanisms. The photoelectrons produced in the target volume deposit their energy over a sub-millimetric distance in the vicinity of heavy atoms, whereas Compton scattering predominates in the surrounding healthy tissues. As a consequence, the dose deposition upstream and downstream of the tumour is further reduced while the dose in the tumoral tissue is reinforced.

At the current stage of development, the SSRT project is at a phase I/II human clinical trial. This means that the dosimetry protocol is established and can be applied in a reasonable time prior to the patient irradiation.

1.2 Microbeam Radiation Therapy

1.2.1 Dose Volume Effect

Spatially fractionated irradiation fields were introduced in 1909 by Alban Köehler who used a grid made of iron wires to reduce skin necrosis when irradiating with medium-energy X-rays. The grid therapy as called by J.Laissue [15] preserves skin cells from direct radiation, thus presenting a better healing power when it comes to burning after an irradiation. Despite the apparent utility of grids, nowadays they are only used in precise cases to enhance the tumour control probability (TCP) [16] [15] [17] because most treatments use mega-voltage X-rays and the associated build-up brings the maximum dose deposition to several mm below the skin.

The dose volume effect was highlighted in the late 1950s by Zeman *et al.* while investigating the effect of cosmic radiation on mice's brains. The observation the authors made was a better tissue tolerance to radiation for small irradiation fields. For a 1000 μm wide beam, a dose of 300 Gy is enough to destroy the tissue when a dose of 11,000 Gy is the threshold limit before creating a lesion with a 25 μm wide microbeam [2](Figure 1).

Curtis [18] and Zeman [19] carried out studies using 22.4 MeV deuterium particles. For a complete destruction of cells within 24 days, the required dose for a 1000 μm wide beam is 150 Gy whereas 4000 Gy are needed for a 24 μm wide beam. The high dose caused the destruction of the cells on the path of the microbeam while the surrounding tissue remained unaltered.

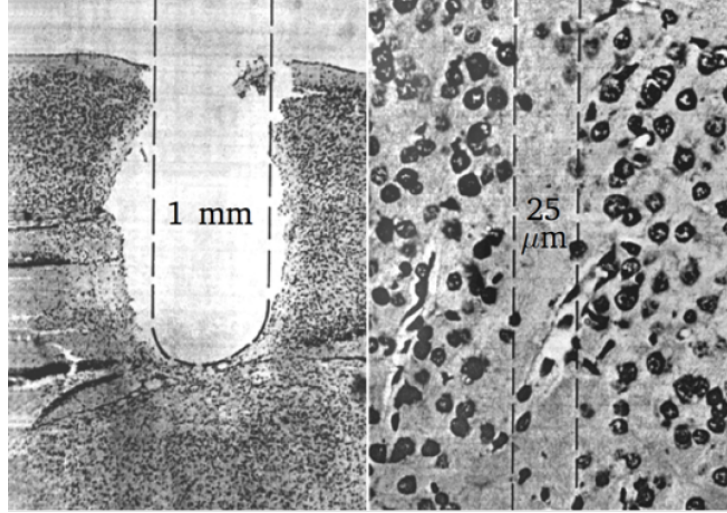


Figure 1: Histological images of a mouse brain irradiated with a 22.5 MeV deuterium beam. On the left image, the mouse brain tissue, irradiated with a 1 mm diameter beam and an entrance dose of 280 Gy (120-day post-irradiation), is completely destroyed while on the right image the tissue irradiated with a 25 μm beam and an entrance dose of 4000 Gy is preserved (28-day post-irradiation) [2].

The irradiation with a wider beam causes tissue necrosis, deleterious effects on the circulatory system and delayed radiation damages on vessels. In the case of the thinnest beam, vessels repaired faster along the microbeam path thus preserving the vascular network. Unfortunately, the use of deuterium particles does not suit the requirements for radiation therapy as their attenuation in biological tissue is strong (15 mm depth under the skin).

1.2.2 MRT technique

MRT was first proposed in 1992 at the Brookhaven National Laboratory (BNL) in collaboration with the National Synchrotron Light Source (NSLS) in Upton, USA [1]. A patent for the MRT was submitted two years after [20] and MRT was implemented at the ID 17 biomedical beam line at the ESRF.

The principle of MRT is to create a highly collimated, quasi-parallel array of microbeams in the kilo voltage energy range by the means of a 3rd generation synchrotron. The beam is spatially fractionated by a multislit collimator (MSC) made of tungsten carbide (WC). The beam is characterized by three main parameters:

- **The centre-to-centre (c-t-c)** distance is the distance between two microbeams.
- **The microbeam width** is the aperture of each slit.

- **The field size** is the lateral distance thus the number of microbeams within the field

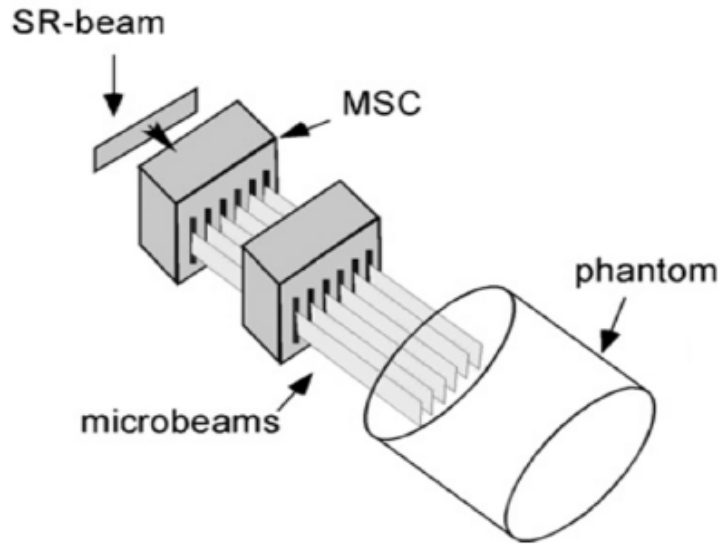


Figure 2: Beam collimation using two MSC's to adjust microbeams width [3]

Those parameters are either fixed or tunable, depending on the use of one single MSC or two MSC's in combination. The typical microbeam width in this study is $50\ \mu\text{m}$ and c-t-c spacing $400\ \mu\text{m}$ although a range of $25\ \mu\text{m}$ to $100\ \mu\text{m}$ in width and $100\ \mu\text{m}$ to $400\ \mu\text{m}$ in c-t-c [21] and is allowed by the system described in Figure 2. As a consequence the MRT irradiation beam differs from medical accelerators generated fields. Table 1 lists the main differences between CRT and MRT. Those differences have a direct impact on the dosimetry protocol. As a matter of fact, every detector on offer is designed to be reliable for measurements in large fields, high energy and medium/low dose rates. Their millimetric size forces their use for measurements in slowly spatially varying fields. Figure 3 displays the difference of the absorbed dose at 2 cm depth in PMMA between MRT and CRT for a $2 \times 2\ \text{cm}^2$ field. The spatial variations in MRT are at the micron scale whereas in CRT the dose profile is almost flat at the centre of the field. The measurement of the fast spatial variations of the dose combined with the steep dose gradients represents a challenge and requires either a detector with a small enough sensitive volume ($1\ \mu\text{m}$ typically) or a dosimetry protocol at a single well-characterized measurement position.

| | CRT | MRT |
|-----------------------------|---|--|
| Source | Linear Accelerator | Synchrotron |
| Energy Range | 1–25 MeV | 0–600 keV |
| Dose Rate | 1–6 Gy/min | 15,000 Gy/s |
| Field Size | 1x1 cm ² to 20x20 cm ² | 2×2 cm ² Scanned with 0.0520x2 cm ² |
| Field Spec | Full | Spatially fractionated |
| Detector's Sensitive Volume | radius 2.4 mm length 4.8 mm | radius 1.1 mm length 1 μm |

Table 1: Comparison between linear accelerator and synchrotron irradiation specificities.

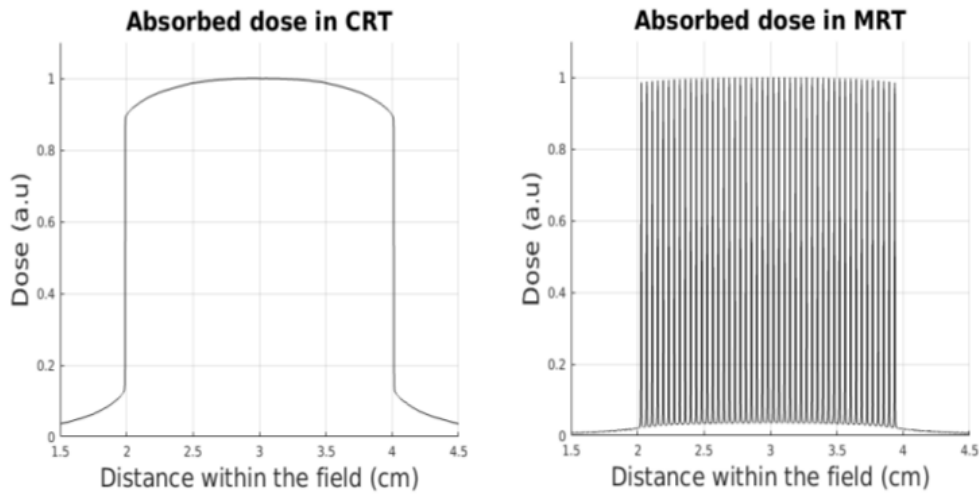


Figure 3: Simulated absorbed dose at 2 cm depth for CRT and MRT

1.3 MRT preclinical results

The first MRT pre-clinical trial (mice) was performed by Slatkin [22] in 1995 at the BNL. Healthy rat brains were irradiated to investigate the influence of the beam width, height, c-t-c spacing on histological sections. To this end, a single slit collimator with tunable

aperture was used, in combination with a "step and shoot" irradiation (translation of the patient followed by irradiation) to create the array of microbeams. Irradiation conditions are summarized in Table 2.

| Dose Range | Field Size | c-t-c | Number of slices |
|----------------|--------------------------------|---------------------------------------|------------------|
| 312 to 1000 Gy | 20 μm \times 4 mm | 200 μm | 20 |
| 312 to 1000 Gy | 42 μm \times 7 mm | 200 μm | 20 |
| 312 to 1000 Gy | 37 μm \times 4 mm | 75 μm or 200 μm | 21 |

Table 2: Irradiation conditions in Slatkin's study.

As a result, half of the rats that received 10,000 Gy developed brain necrosis. Regarding the other half, and those who received 5000 Gy, loss of nuclei was observed along the microbeams path but without any brain necrosis nor brain damage. At lower entrance dose, 2500 at 1250 Gy the absence of necrosis was observed in 57% and 25% of the rats respectively.

Not long after, J.Laissue [23] investigated the potential of MRT to treat rats bearing cerebral 9L gliosarcomas. The field consisted in 101 microbeams, 25 μm wide and 100 μm c-t-c spacing. They irradiated the rats with either one array or two arrays in cross shaped configuration. A peak dose of 625 Gy was delivered for the single array configuration and two different peak doses were investigated for the two orthogonal array configuration (312 and 625 Gy). Both configurations highlighted an increase in the rats life span compared to unirradiated controls. The best results were obtained with orthogonal arrays with a peak entrance dose of 635 Gy leading to a survival time of 139 days after tumour implementation, compared to 20 days for controls.

Moreover, the authors observed a disappearance of the tumour in both configuration in 61% of the rats for the crossed arrays, and 36% for the regular configuration. The increased radio-resistance of the normal brain tissue was imputed to a potential fast repair of the microscopic lesions by adjacent cells in the valley that received a lower dose.

This study led to an important question about the tolerance of normal immature developing tissue to MRT irradiation. A long-term study was then carried out by J.Laissue [24] to estimate the tolerance of suckling rats brains using a unidirectional irradiation and a peak entrance dose of 50 or 150 Gy, a 28 μm wide microbeam width and a c-t-c spacing of either 105 μm or 210 μm . As a result, after 15 months none of the rats had died nor needed to be euthanized. Although a weight loss, neurological and behavioural anomalies

were observed for rats irradiated with the highest dose and the narrowest c-t-c spacing. The other irradiation conditions allowed a better sparing of healthy tissue, and the development of the rats remained similar to the unirradiated control rats.

The following study performed by J.Laissue [4] aimed at verifying that the fractionated structure of the beam is conserved at large depths. To that end, 40 and 41 days old suckling piglets were used. The similitude in neurological development between piglets and human infants make them a good animal model.

The irradiation was performed with skin entrance peak doses ranging from 150 to 600 Gy, $1.5 \times 1.5 \text{ cm}^2$ field of $25 \mu\text{m}$ wide microbeams and $210 \mu\text{m}$ c-t-c spacing. For at least a year, no neurological changes were observed in any of the irradiated piglets nor the controls. Figure 4 displays a histological section of one of the piglets 15 months after being irradiated with a 300 Gy peak entrance dose. The cells on the path of the microbeams are destroyed, although no haemorrhage is to be noticed.

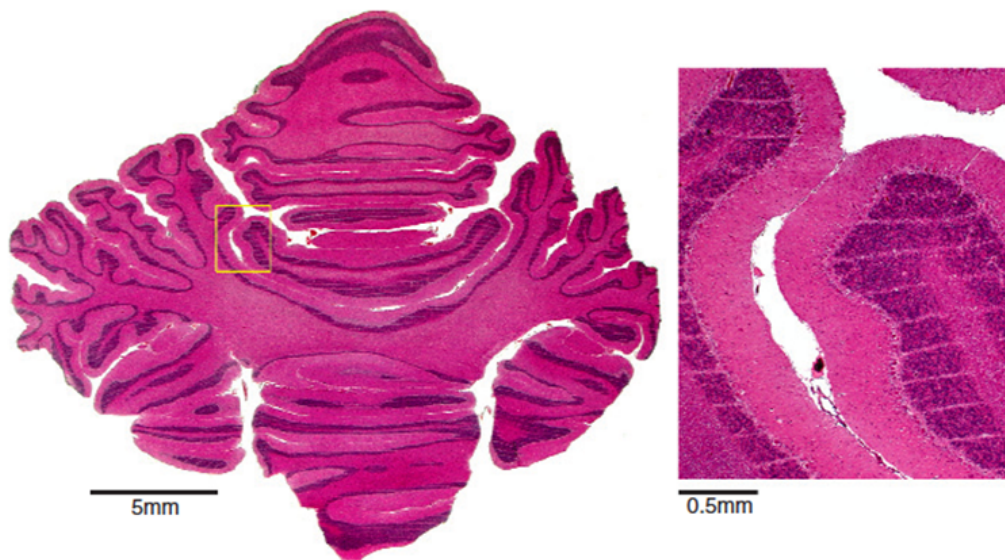


Figure 4: Histological images of a piglet brain 15 months after MRT irradiation with a skin dose of 300 Gy [4].

These studies demonstrated the beneficial effect of MRT and showed an increased life span and tumour reduction while keeping the neurological development integrity of the patients. Moreover, the sparing of the healthy tissue is a substantial added value to make

MRT worth considering for brain tumours for both adults and paediatric patients. Nowadays conventional treatments cause neurocognitive dysfunctions to paediatric patients [25] making MRT a realistic alternative CRT.

Following studies aimed at improving MRT by optimizing the irradiation parameters and more importantly by understanding the mechanisms responsible for the differential effect thus the healing power of MRT.

1.4 Optimization of the MRT parameters

The peak dose is lethal to the cells, but the valley dose has to remain under the tissue tolerance therefore has to be as low as possible. The valley dose is built up by scattered radiation so the greater the c-t-c, the lower the valley dose. The peak dose, on the other hand, mainly depends on the microbeam width.

But the optimization is not straightforward as c-t-c also influences the peak dose (at a lower scale), the closer the microbeams the greater the contribution of the microbeams with each other, and the microbeam width influences the valley dose with increased scattered radiation.

1.4.1 Microbeam c-t-c spacing

Dilmanian *et al.* [26] studied the life span of rats implanted with 9L gliosarcoma. The irradiation was unidirectional with a fixed microbeam width of 27 μm and c-t-c spacing ranging from 50 μm to 100 μm . Skin entrance doses were chosen 150, 250, 300 and 500 Gy.

As a result, an increased life span was observed compared to the controls (19 days). The lowest survival time obtained with MRT corresponds to the 50 μm c-t-c spacing and 300 Gy peak entrance dose and 75 μm c-t-c spacing and 500 Gy peak entrance dose.

These results suggest that MRT efficiency highly depends on the valley dose and the authors concluded that, in the normal tissue, the valley dose must remain under the organ dose tolerance in order to preserve the MRT beneficial effect.

1.4.2 Microbeam width

Serduc *et al.* [27] irradiated both healthy rats and rats implanted with 9L gliosarcoma with different microbeam widths: 25, 50 and 75 μm and a constant c-t-c spacing of 210 μm . Attention was drawn on the value of the valley dose maintain constant for each irradiation

configuration. As a result, 50 μm was found to be the optimum between tumour control and tissue toxicity. In 2012, Griffin *et al.* [28] carried out a study including beam (50 and 500 μm width, c-t-c spacing (200 and 2000 μm) and peak (75 and 100 Gy at 0.5 mm depth). The best results in terms of tumour control were observed with the smallest microbeam width and c-t-c spacing.

In addition, Uyama *et al.* [29] observed a better tumour growth reduction for narrow microbeams and c-t-c spacing on human U251 glioma cells. The best results were obtained with 20 μm width, 100 μm c-t-c rather than 100 μm width, 500 μm c-t-c.

Results from the pre-clinical studies indicate that the smallest beam width and spacing is more efficient in tumour control probability.

1.5 Dosimetry

Reference dosimetry consists in the measurement of the effect of ionizing radiation on matter in reference conditions. The physical quantity that represents this effect is the dose and corresponds to the amount of energy deposited per mass unit in a material. The dose can be defined as follows:

$$D = \frac{\Delta E}{\Delta M} \quad (1)$$

The unit of the dose is the gray (Gy) which corresponds to joules per kilograms. Photons are uncharged particles therefore do not deposit the dose directly. Photons interact with electrons in the media and deposit energy while losing kinetic energy through Coulomb interaction with other electrons.

Photons can interact with electrons of a medium in four different ways:

- **The photoelectric effect (PE)** Where the incoming photon interacts with a bound electron of the material. Its energy has to be higher than the binding energy of the electron but not too high otherwise other interaction mechanisms become more likely to happen. Figure 21 displays the different cross sections in water for energies E ranging from 1 keV to 5 MeV. In water with density 1 PE is predominant for energies below 40 keV.

In this process, the photon disappears and ejects the bounded electron with a kinetic energy E_e that corresponds to the excess of energy related to the bounding energy

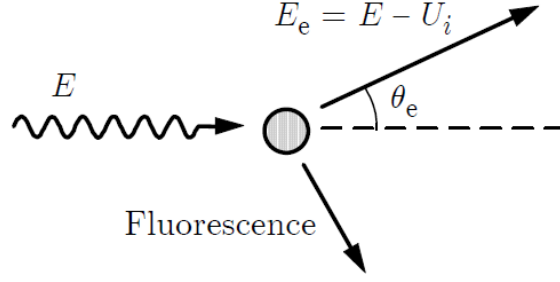


Figure 5: Photoelectric absorption [5]

U_i (Figure 2).

$$E_e = E - U_i \quad (2)$$

The photoelectric cross section is called σ_{PE} and varies with energy and atomic number as [30]:

$$\sigma_{PE} = \frac{Z^4}{E^3} \quad (3)$$

The ejected electron leaves behind a vacant energy level that is then filled up by an electron either from an upper energy shell or an unbounded electron. As a result, a fluorescence photon is emitted which direction is distributed isotropically in space.

- **Compton Scattering (CS)**, also called incoherent scattering. This process involves an incoming photon of energy E scattering on a free (or weakly bounded) electron of the media. The electron is ejected and the photon is scattered with an angle that depends on the transferred energy.

The energy of the scattered photon E' is expressed by:

$$E' = \frac{E}{1 + \alpha(1 - \cos \theta)} \quad (4)$$

Where $\alpha = \frac{E}{m_e c^2}$, $m_e c^2 = 0.511 \text{ MeV}$ and θ is the polar scattering angle

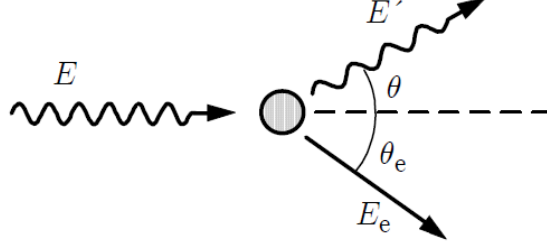


Figure 6: Compton scattering [5]

The kinetic energy acquired by the electron is:

$$E_e = E \frac{\alpha(1 - \cos \theta)}{1 + \alpha(1 - \cos \theta)} \quad (5)$$

The cross section for the Compton scattering is written σ_{inc} . During a Compton event, the direction of propagation of the scattered photon is not isotropically distributed meaning that the probability of scattering in a particular solid angle $d\Omega$ is not constant despite the fact that the scattering probability in the azimuthal angle χ is constant. The probability for a photon of energy E to be scattered with an angle θ is given by the Klein-Nishina (KN) differential cross-section (DCS) formula:

$$\frac{d\sigma_{KN}}{d\Omega}(\alpha, \theta) = \frac{r_0^2}{2} \frac{1}{(1 + \alpha(1 - \cos \theta))^2} \left(1 + \cos^2 \theta + \frac{\alpha^2(1 - \cos \theta)^2}{1 + \alpha(1 - \cos \theta)} \right) \quad (6)$$

With r_0 the classical radius of the electron ($r_0^2 = 7.940775 \cdot 10^{-26} \text{ cm}^2$). Monte Carlo algorithms for radiation transport usually includes the KN model for Compton scattering. Though it should be noted that no intrinsic parameters related to the interaction media is accounted for in this formula as electrons are considered free. Later in this chapter, methods that include Doppler broadening and binding effects (media specific quantities) will be discussed and compared for three widely used MC codes.

- **Rayleigh Scattering**, also known as coherent scattering, is the event where a photon interacts with a bound electron without excitation of the target. The scattered photon has the same energy as the incident photon but suffers from a change in direction of propagation.

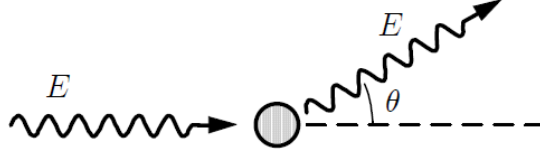


Figure 7: Rayleigh scattering [5]

The atomic DCS per unit solid angle for Rayleigh scattering can be calculated with the non-relativistic perturbation theory [31]. A photon with an energy E higher than the ionization energy K shell follows the DCS:

$$\frac{d\sigma_{Ra}}{d\Omega} = r_e^2 \frac{1 + \cos^2 \theta}{2} [F(q, Z)]^2 \quad (7)$$

Where θ is the polar scattering angle r_e is the classical electron radius, $F(q, Z)$ is the form factor and q is the magnitude of the momentum transfer. The form factor theory is not straightforward and will not be developed here but form factors are available from EPDL [32].

The total atomic cross-section for Rayleigh scattering σ_{Ra} is expressed by:

$$\sigma_{Ra} = \int \frac{d\sigma_{Ra}}{d\Omega} d\Omega = \pi r_e^2 \int_{-1}^1 (1 + \cos^2 \theta) [F(q, Z)]^2 d(\cos \theta) \quad (8)$$

- **Pair production** refers to the creation of an elementary particle and its antiparticle. In the case of a photon, if its energy is higher than twice the rest energy of the electron ($2 \times 511 \text{ keV} = 1022 \text{ keV}$) the photon can split into an electron and a positron.

The cross section for the pair production is written σ_{pp} .

In this work the maximum incoming photon energy is 510 keV therefore no pair production event can occur and its description would not be an added value for this work.

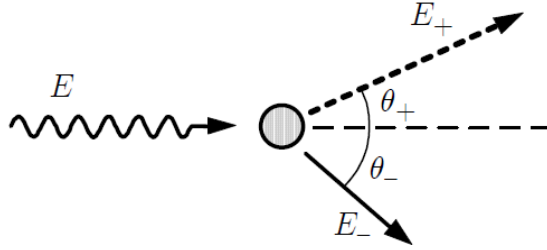


Figure 8: Pair production [5]

1.5.1 Reference Dosimetry in MRT

Conventional radiation therapy (CRT) involving X-rays is routinely performed in the major part of radiotherapy centres and is well understood. Dosimetry protocols are developed with respect to the available technology in terms of radiation detectors which are designed to fit CRT dosimetry requirements. For instance, the IAEA in its Technical Report Series No. 398 (hereafter referred to as TRS-398) Code of Practice [33] describes how to calibrate only cylindrical Ionization Chambers (IC) with a cavity volume in the range of 0.1-1.0 cm³ based on standards of absorbed dose to water. Subsequently, companies such as PTW (Freiburg, Germany) manufacture a wide variety of IC's. But in MRT the beam characteristics combined with the dimension of the sensitive volume of the currently available IC's make this Code of Practice not applicable in a straightforward way.

In photon beams, the use of field sizes smaller than the lateral range of secondary particles will result in a lack of Charge Particle Equilibrium (CPE) within the field. These fields are too small to achieve a build-up of lateral dose at the centre of the beam profile, where lateral scatter is at its maximum. The dose falls off continuously while moving away from the centre [34]. There is a minimum field size that is required to form CPE; it depends on the energy of the photon beam, the source geometry and the material irradiated [35] [36] [37]. The correction factors used in standard radiation therapy rely on the uniform particle fluence in CPE regions. When the detector is placed in the irradiated media, the electronic fluence is no longer uniform, and one has to account for the volume averaging effect. Therefore, the combination of the standard k_Q and additional correction factors is needed to achieve an increased accuracy of small field dosimetry.

Alfonso *et al.* proposed a new formalism for small field dosimetry which introduces the concept of an intermediate calibration field for machines that cannot establish conventional reference conditions. The small field detector is then calibrated in the inter-

mediate, or “machine specific reference field” against a calibration ionization chamber to which dosimetry protocols can be directly applied.

At the ESRF, the current dosimetry protocol is performed in a broad beam configuration and follows the recommendations of the IAEA TRS-398 protocol for medium energy kilo voltage X-rays. The dose measurement is performed in a PTW water tank at 2 cm depth for a 2 cm × 2 cm field size using a PTW PinPoint Ionization chamber with a volume of 0.015 cm³. The absolute peak entrance dose is then calculated by the means of output factors (OF) obtained from MC simulations [38].

1.5.2 Relative Dosimetry

Absolute dosimetry at the micron scale has been a real challenge for the past few decades. Until very recently, detectors capable of measuring doses with a micrometric spatial resolution were not available. To overcome this problem, two quantities of interest are defined: Output Factors and Peak to Valley Dose Ratios (PVDR). Both PVDR and OF are relative quantities defined as the ratio of two different doses. Figure 9 displays the different measurement points to calculate OF’s and PVDR’s.

Equation 9 is the ratio between the maximum dose measured for a 50 microns wide beam and the maximum dose in a 2×2 cm² field. This defines the OF which is the attenuation in terms of maximum dose caused by the MSC.

Equation 10 is the ratio between the peak dose in an array of 50 μm wide microbeams spaced with 400 μ in a 2×2 cm² field and the closest valley dose.

$$OF = \frac{D_{\max 50}}{D_{\max 2}} \quad (9)$$

$$PVDR = \frac{D_{\text{Peak}}}{D_{\text{Valley}}} \quad (10)$$

OF’s and PVDR’s are directly linked due to the fact that an array of microbeams is the sum of one single microbeam as many times as needed for the desired field size. So the use of the TRS-398 makes sense under the condition of having a perfect knowledge of OF’s and PVDR’s for a lot of irradiation conditions. This would allow us to perform on single absolute broad beam measurement and directly check if the valley dose remain under the tissue tolerance.

One should notice that the irradiation setup in MRT imposes the need for accurate knowledge of OF’s as those values are used to deliver the dose during the treatment.

$$v_{z(mm/sec)} = D_{(Gy/sec/mA)} \cdot I_{(mA)} \cdot OF_{(OutputFactor)} \frac{z_{beam-height(mm)}}{D_{(Gy)}} \quad (11)$$

The calculation of the scan speed for the accurate dose delivery is given by equation 11. It accounts for the dose rate of the machine $D_{(Gy/sec/mA)}$, the prescribed dose $D_{(Gy)}$ the beam height, $z_{beam-height(mm)}$ and the output factor.

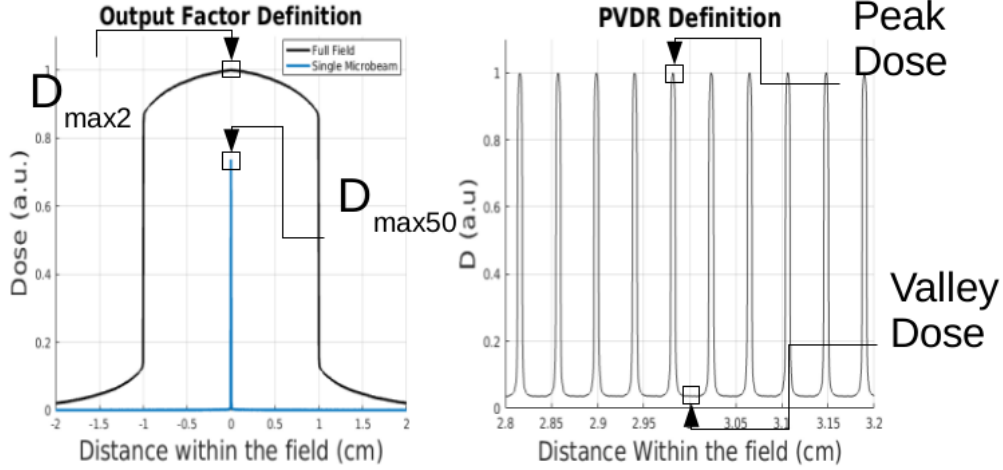


Figure 9: Definition of OF and PVDR.

In other words, OF's are not only useful for dosimetry purposes, they are also needed for the dose delivery.

1.6 Synchrotron Source

Synchrotron is the name given to the radiation emitted by a charged particle that undergoes an acceleration [39]. Within the scope of relativistic particles, the synchrotron radiation has quite unique characteristics such as a continuum spectrum from the infrared to the X-rays, a small divergence, coherence, high degree of polarization and a short temporal structure.

Figure 10 provides a diagram of a multi-sation synchrotron. Electrons are generated in the electron gun then accelerated in the linac. The booster is a circular accelerator that propels the electrons to nearly the speed of light (6 GeV). These electrons are then injected in the storage ring where they are forced to remain on the same orbit as a very

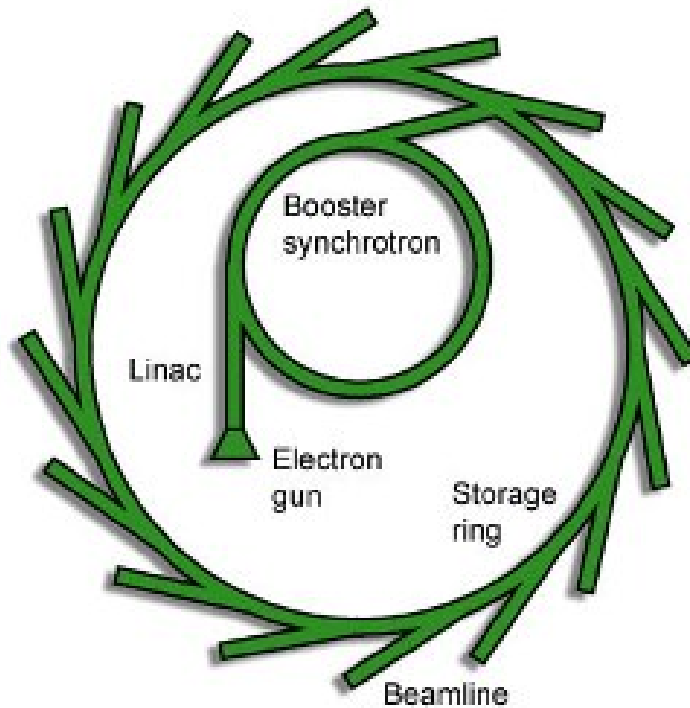


Figure 10: Diagram of a synchrotron.



Figure 11: Bending magnet(left) and insertion device(right)

dense package by the means of quadrupoles and sextupoles. Bending magnets or insertion devices (ID) -whose operating principles are different but lead to the generation of X-rays- are placed on several points on the storage ring. Bending magnets, generate magnetic fields that change the path of the electrons to make their trajectory circular (Figure 11).

An object with such a trajectory undergoes a centripetal acceleration, and charged particles emits X-rays tangentially relative to the trajectory. ID's, (a wiggler typically) on the other hand, are added to accelerators to produce light that is specifically tailored to the experimental requirements (wavelength, flux, brightness, polarization). They consist in two parallel arrays of magnets with alternate polarity, through which electrons travel and

| ID parameters | ID 17 (w150) |
|-----------------------------|--------------|
| Magnetic field period (cm) | 15 |
| Number of periods | 11 |
| Magnetic field strength (T) | 1,592 |
| Deflection parameter | 22.30 |
| Critical energy (keV) | 38 keV |
| Total power (kW) | 13.3 |

Table 3: ID 17 Wiggler characteristics

are periodically deflected. The period of polarity changing in the wiggler (λ_u) is directly linked to the wavelength of the emitted photon (λ) as shown in the wiggler equation 12.

$$\lambda = \frac{\lambda_u}{2n\gamma^2} \left(1 + \frac{K}{2} + \theta^2\gamma^2 \right), \quad (12)$$

with K the deflection parameter, γ the Lorentz factor and θ the emission angle. For example, for a 3 GeV electron passing through a 50 mm period wiggler with $K = 3$, the wavelength of the first harmonic on-axis is 4 nm. The translation from cm periods of the wiggler to nm wavelengths is due to the huge value of the term γ^2 .

The distance between the two sets of magnets in an insertion device known as the gap can be tuned as well so as to adjust the energy spectrum and the fluence of the generated photons. Table 3 summarizes the characteristics of the ID 17 wiggler. The conservation of energy imposes a loss of energy in the storage ring due to the emission of synchrotron radiation. Electrons have to be accelerated to compensate this energy loss. Radio frequency cavities are placed around the storage ring to counteract this problem.

1.6.1 ID 17 MRT beam line characteristics

At the ESRF, ID 17 is the biomedical beam line. Research taking place here varies from medical imaging, radiation biology and radiation therapy. The radiation therapy research program is focused on two main techniques both based on synchrotron radiation. The Synchrotron Stereotactic Radiation Therapy(SSRT) [40] [41] is the more advanced in terms of protocol validations and human trials. MRT's current state of development is at the small animal clinical trial recently moving towards a project involving bigger animals. SSRT and MRT are performed in two different hutches. The MRT hutch is located 40 m away from the wiggler whereas in SSRT the hutch is placed at 150 m away from the

source, in a satellite building (Figure 12). MRT relies on a polychromatic source compared to SSRT which utilizes a monochromatic photon beam. The beam tuning in MRT is performed by a 15 cm period wiggler (w150). In SSRT the W150 is used in combination with another wiggler with a 12.5 cm period (w125) to further increase the monochromatic photon flux.

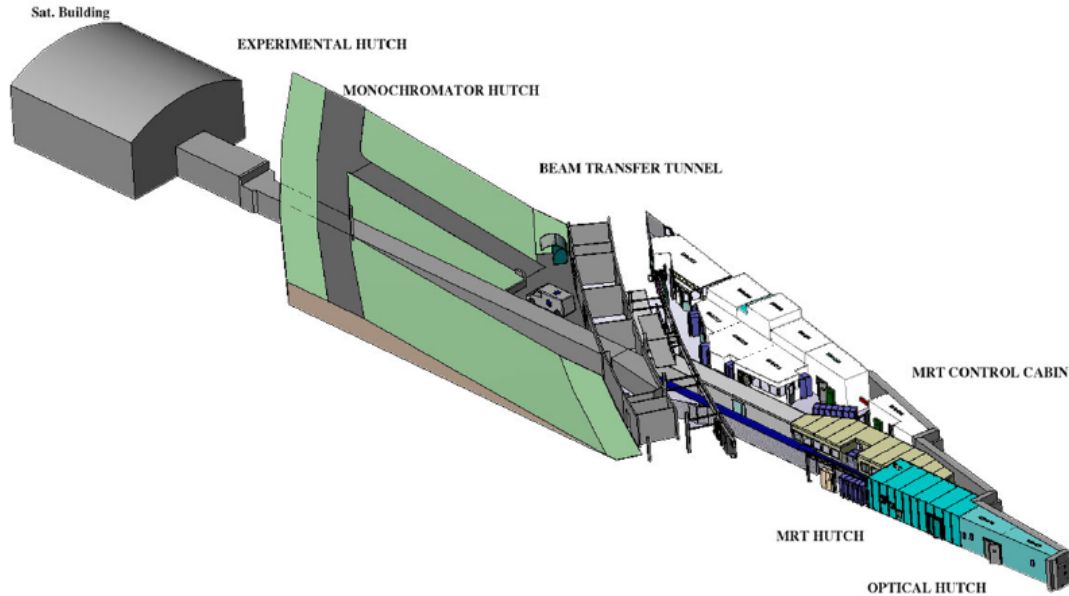


Figure 12: ID 17 medical beam line. The optical hutch is located in the experimental hall. A tunnel connects the MRT hutch to the satellite building where the SSRT is performed.

From the wiggler, X-rays travel through a long stainless pipe under vacuum. Vacuum between different sections of the pipe is ensured by the presence of valves and Beryllium windows (300 to 500 μm in thickness). At 21.6 m away from the source a diaphragm limits the beam dimensions. This limitation of 2.4 cm in the horizontal direction and 0.5 cm in the vertical direction is designed to minimize the heat load of the downstream instrumentation devices. At the patient position, the maximum beam dimensions cannot exceed $41 \times 2.5 \text{ cm}^2$.

As a first step, the beam is focused by a primary slit made of oxygen-free copper blocks located at 29.3 m away from the source. The primary slits allow the user to set the primary horizontal and vertical apertures. A succession of different water-cooled filters are

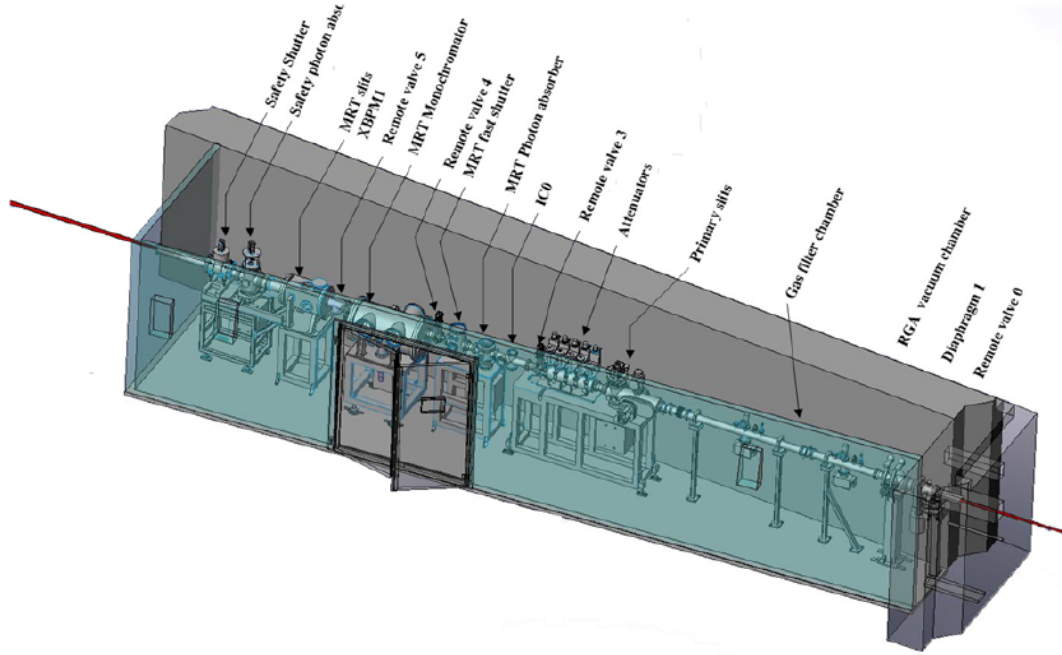


Figure 13: MRT optical hutch.

positioned downstream the primary slit to in order to remove energies lower than 30 keV from the spectrum. The typical filtration in MRT is the following: 1.42 mm of C, 0.28 mm + 1.24 mm of Al and 0.35 mm + 0.69 mm of Cu.

The resulting photon energy spectrum has been calculated by Martinez-Rovira [12]. The MRT spectrum currently used for MC simulations ranges from 27 keV to 600 keV with a mean energy around 100 keV.

A major aspect in MRT is the dose delivery. The extremely high dose rate allows a very short irradiation to deliver a dose compatible with tissue tolerance. The exposure time is controlled by a fast shutter [6] whose opening time is 5 ± 0.5 ms. Figure 14 provides the mechanical design of the fast shutter. Two 15 mm thick blades made of tungsten carbide (WC) are coupled to an actuator. When the fast shutter is at rest, blade 1 is below the beam axis while blade 2 obstructs the photon beam. Before an irradiation, the electromagnets are triggered to arm the system. As a result, blade 2 goes above the beam axis, while blade 1 blocks the incoming photons.

When the irradiation starts, the supply to blade 1 electromagnet is powered down, throwing blade 1 to its initial position. At this stage of the irradiation the photons are allowed to pass through the fast shutter. The irradiation stops when the supply is cut and blade 2 goes back to its initial position blocking the incoming X-rays.

In order to protect blade 2 from heating, a 15 mm thick cooled copper absorber follows blade 2's motion with a delay of 1 second.

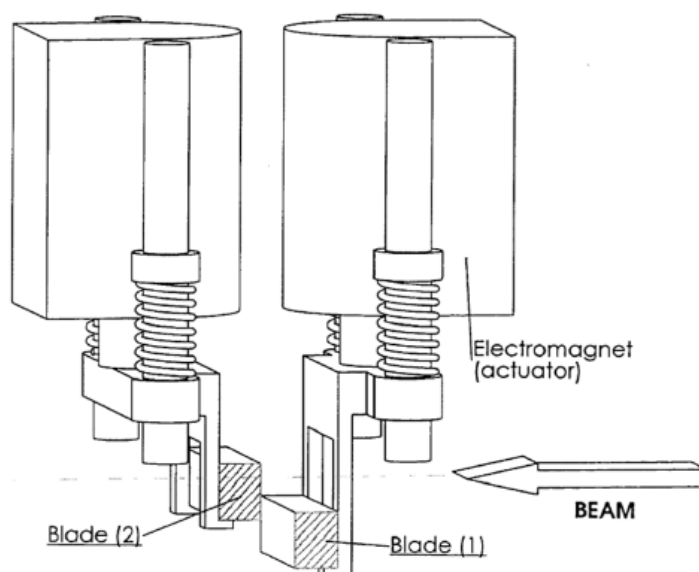


Figure 14: Design of the fast shutter [6].

1.6.2 MRT experimental hutch

Figure 15 displays the MRT experimental hutch. The ionization chamber IC1 monitors the beam at the entrance of the experimental hutch followed by PMMA attenuators and a rotary shutter used for imaging purposes. During the irradiation, both the PMMA attenuators and rotary shutter are removed from the path of the X-rays. Further vertical and horizontal slits made of WC are inserted to adjust the beam width and height prior the MSC.

As described in Braueur-Krisch *et al.*,2009a [7] (Figure 16) the MSC is a WC block is designed with 50 μm wide gaps spaced with a period of 400 μm . The MSC is embedded in an Al box and cooled down by the means of a nitrogen gas flush. The patient, sample or dosimetry phantom is set on the a 3-axis Kappa-type high precision goniometer (Huber, Germany) located at 40.5 m from the wiggler X-ray source.

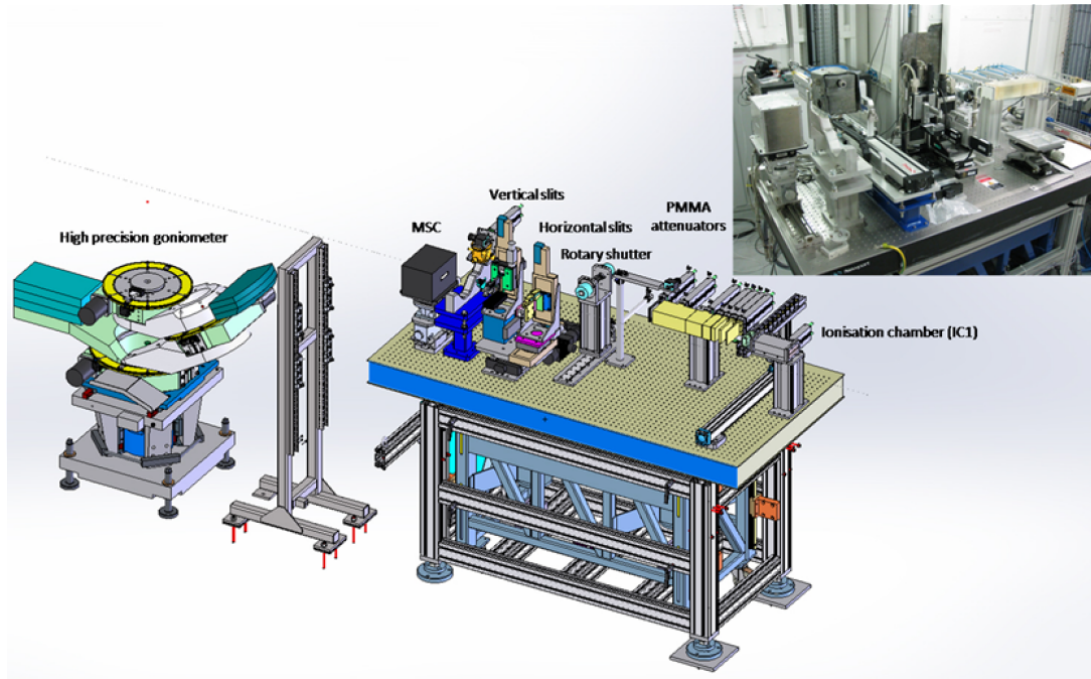


Figure 15: Technical drawing of the MRT hutch [6] and the associated picture.

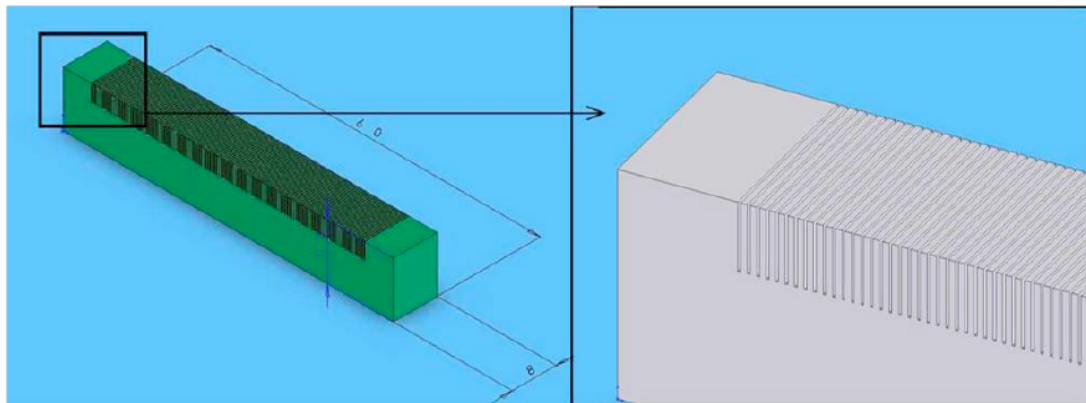


Figure 16: Technical drawing of the MSC [7].

1.6.3 SSRT experimental hutch

As a first step, at the entrance of the hutch the beam is shaped properly by the means of cerobend masks. The number of masks corresponds to the number of irradiation ports, and their respective shapes are extracted from the treatment planning system (TPS) as a projection of the tumour section the beam sees. The different masks are placed on a rail, which are exchanged when the irradiation port changes.

Like in MRT, the beam height is limited, although larger (2 mm) because the patient is located after the same MRT experimental hutch. As a consequence, an irradiation over a

distance greater than 2 mm is performed by scanning the sample through the beam.

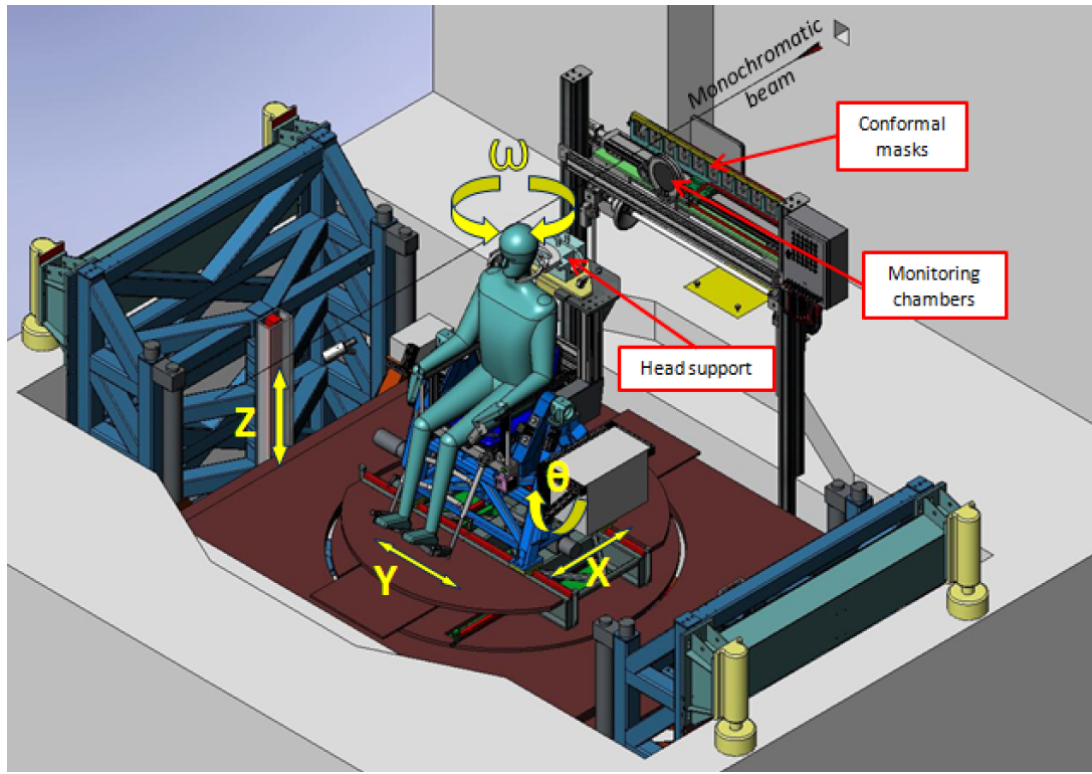


Figure 17: Patient positioning system in SSRT. The field is conformed by cerrobend masks and the flux is monitored by two plate IC.

Compared to conventional RT treatments where the source moves around the patient, the synchrotron beam is fixed. The rotation of the patient is performed by the means of a dedicated patient chair that allows 5 degrees of freedom (Figure 17). The chair is also used to acquire CT imaging of the patient before the irradiation for positioning purposes.

1.7 Project overview

The high dose-rate in MRT, the spatial fractionation of the beam and the use of medium energy photons highlight the need for a new kind of dosimetry. The knowledge that we have about cancer treatments involving radiation is based on decades of the use of full field and megavoltage X-rays. That is why the tumour control probability (TCP) and the normal tissue complication probability (NTCP) [42] are well known for most treatments available today and help in quantifying the therapeutic outcome of a radiotherapy (RT)

treatment. These two quantities are defined to provide the most efficient treatment for each type of known cancer, as the TCP must be high while the NTCP has to be as low as possible.

A mathematical model called the linear quadratic model (LQ) is a model used to compare different treatment modalities by accounting for the influence of temporal fractionation on the relative biological effect (RBE), and is also the product of decades of studies and clinical use of radiation for medical purposes. Limitations in the LQ model -due to the discrepancies between the *in vitro* protocol used to collect the data utilized by the LQ model and the complexity of the vascular and stromal repairs occurring after an irradiation- have been highlighted for high dose rate stereotactic radiosurgery (SRS) [43].

In MRT, the combination of the spatial fractionation and the high dose-rate generates a different tissue response to conventional irradiation, so that a hypothesis of a selective radio-vulnerability of the tumour vasculature versus normal vessels by MRT is still studied. That is to say, the knowledge we have in terms of conventional radiation therapy is not applicable as it is for MRT, but needs to be adapted.

The research in MRT is centred on 3 main axes. The first one is the improvement of the ID 17 medical beamline to take in patients, such as goniometric tables for the patient placement, the enhancement of devices for beam monitoring [44], and the adaptation of a Patient Security System (PSS) that already exists for Synchrotron Stereotactic Radiation Therapy (SSRT). The second axes considers radiobiology in MRT and about understanding the effect of such radiation on tissues. Finally, the last research axis is about the accuracy of the dose measurement and calculation, in order to develop a treatment planning system and a dosimetry protocol dedicated to MRT.

1.8 Project Aims

This work is focused on the development of an accurate dosimetry in MRT by means of a PTW microDiamond detector and Monte Carlo (MC) simulations. The PTW microDiamond detector has a 0.004 mm^3 cylindrical active volume, with a 1.1 mm radius and a thickness of 1 μm . This detector presents the advantage of being almost tissue-equivalent, and its geometry allows high resolution measurements. The highest resolution is obtained when the greatest dimension of the sensitive volume of the detector is parallel with the direction of the beam ('edge-on' mode) [45] furthermore, this configuration reduces the volume averaging effect [46]. By using the detector this way we can measure the dose deposited inside the microbeam (peak) and outside (valley) at micrometric resolution and

calculate the peak to valley dose ratio (PVDR).

The PVDR is a relative value, and consequently becomes important only when dose values are converted from the treatment plan to compute the absolute valley dose for the normal tissue, which corresponds to the classical maximum admissible dose value with respect to NTCP [44]. Absolute dosimetry protocols have been proposed in synchrotron beams using ionization chambers (IC's) for broad beam dose rate measurements [47]. At the moment, the absolute dose determination at the ESRF for MRT is carried out for 2×2 cm² fields using dose rate measurements in broad beams with a PinPoint chamber [48].

This dosimetry protocol is limited for spatially fractionated synchrotron beams as the PinPoint chamber does not satisfy the requirements for a suitable dosimetry in terms of spatial resolution. Nevertheless, the relative dose profiles at depth can be determined using several types of detectors, all with their individual advantages and disadvantages. The most promising results so far were obtained with Gafchromic films either in combination with a microdensitometer or microscope. Films provide important information about dose gradients and 2D distribution but the resolution of the densitometer limits the spatial accuracy. In addition, the acquisition has significant noise and films cannot be read out in real time. Other potential high resolution dosimeters that are good candidates for MRT dosimetry include fluorescence nuclear track detectors (FNTD's) from Landauer (Al₂O₃ detectors), and 2D thermoluminescence dosimeters (TLDs, however, both are unable to achieve on-line dose monitoring and require a strong calibration.

1.9 Challenges

In any kind of dosimetry -not particularly in MRT- the measurement of the absolute dose deposition in a medium -even a homogeneous- medium, remains a delicate task. This is due to four key effects described by Bouchard et al. [49] that occur as soon as one puts any detector in a medium. (i) The atomic properties of the detector sensitive volume may be dissimilar to water, which affects the dose response and perturbs the particle fluence (ii) the electron density of the detection medium relative to water scales the interaction coefficients and also perturbs the particle fluence (iii) the presence of non-sensitive components in the detector (including walls, electrodes, wires) causes particle interactions to be different from the situation where the detector is a bare cavity (iv) the finite size of the detector -even made of water- causes a volume averaging effect. These four key effects need to be corrected for each beam quality. What is meant here by beam quality is the whole irradiation condition which depends on the beam spectrum, the geometry of the

phantom, the position of measurement and the presence of lateral dose gradients [50].

In MRT, the photon and electron spectrum are vary between the peak and the valley, and obtaining dose profiles is achieved by scanning the detector through the beam, a complete set of correction factors should be applied for each measurement point. Our measurements of dose profiles with the PTW microDiamond also demonstrate the non-negligible influence of the non-sensitive components as the profile of the peak is asymmetric reflecting the detector geometry (Figure 51).

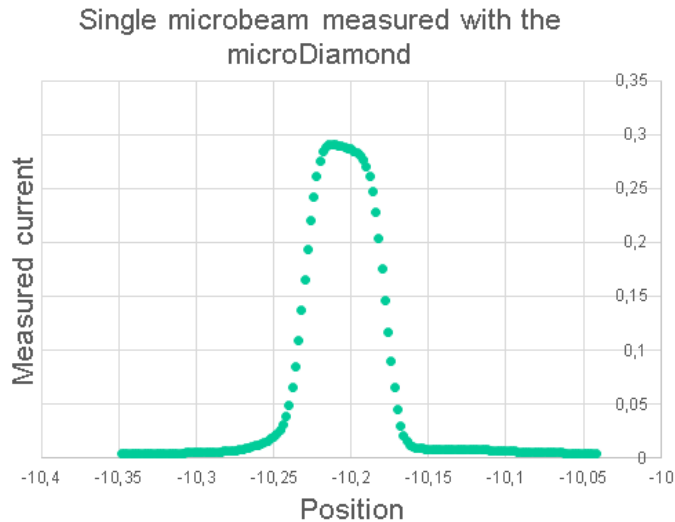


Figure 18: Single microbeam measured with the PTW microDiamond detector. The asymmetry in the lateral dose gradient and the inclined top are the due to the non-sensitive components in the detector.

The set of correction factors proposed by Bouchard et al. for each beam quality can be determined analytically using the Spencer-Attix-Nahum [51] cavity integral for gas based detectors or the Burlin’s theory [52] for solid-state detectors. But these two approaches rely on knowledge of the photon and electron fluence in water and the detector for each beam quality. In small field dosimetry, the main challenge is to determine these quality-dependent electrons fluence. Originally, the calculation was made analytically for reference beams assuming charge particle equilibrium (CPE) that allows the estimation of perturbation factors. However in small fields, these approaches are not suitable and we need to rely on MC simulations [49]. Our ability to properly correct the dose measurement with respect to the beam quality strongly depends on our aptitude to accurately model

the irradiation conditions, and detector geometry. To that end, the ID 17 X-ray source was modelled by the synchrotron ray tracing code SHADOW. The photons from the wiggler were simulated with the MC code PENELOPE/PENEASY through a geometry file containing the whole structure of the beam line until a vertical plane ahead of the patient position [12].

The dose distributions in homogeneous media were experimentally verified using Gafchromic films in a solid-water phantom for both lateral dose gradients and percentage depth dose curves in the broad beam configuration. PVDR were also simulated and compared to Gafchromic measurements and were in agreement. Despite the fact that the current experimental data fail to reproduce the PVDR values predicted by Rovira et al. with both PTW microDiamond and Gafchromic films. In addition to that, some features in the microbeam profile and our inability to retrieve PVDR experimentally leads to the assumption that the MC is not complete.

1.10 Introduction of the PTW microDiamond

The PTW microDiamond detector is a synthetic single crystal diamond detector developed for small field dosimetry. The process used for the manufacture is the chemical vapour deposition of a multilayered highly conductive p-type diamond/intrinsic diamond structure on a high-pressure high-temperature (HPHT) single crystal diamond substrate as described by Almaviva, et al. [53].

Similar to silicon diodes, this Schottky diode detector requires no applied bias to collect charges. Its sensitive volume is a 2.2 mm diameter 1 μm thick cylinder. The diamond active volume is towered over by a thin circular aluminium contact with diameter 2.2 mm which has been thermally evaporated on the intrinsic diamond surface.

| | |
|--------------------------|--|
| Detector type | Synthetic single crystal diamond detector |
| Dimensions | Diameter 7 mm, length 45.5 mm |
| Nominal sensitive volume | 0.004 mm ³ , radius 1.1 mm, thickness 1 μm |
| Detector Bias | 0 V |
| Energy Response | $\leq \pm 8\%$ (100 keV- ⁶⁰ Co) |

Table 4: PTW microDiamond detector specificities.

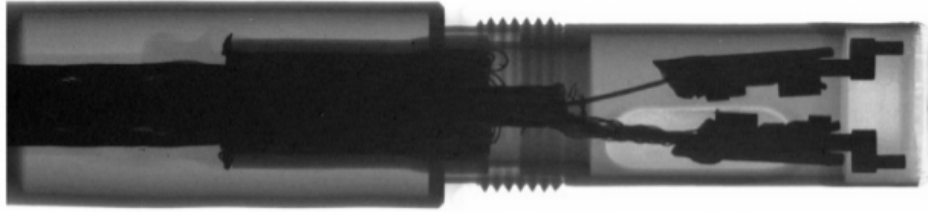


Figure 19: High resolution radiograph of the internal structure of the microDiamond [8].

Table 15 lists the principal characteristics of the PTW microDiamond detector. The key parameter for achieving microdosimetry is the 1 μm thick sensitive volume. Figure 52 displays the internal structure of the microDiamond. The sensitive volume is located at the extreme right of the structure caught in the pair of pliers. Marinelli *et al.* [54] investigated the average sensitive area and thickness over 10 PTW microDiamond detectors. In order to evaluate the microDiamond active volume, the thickness of the diamond sensing layer was independently evaluated by capacitance measurements and alpha particle detection experiments. An average active surface area diameter of 2.19 ± 0.02 mm. Average active volume thicknesses of 1.01 ± 0.13 μm and 0.97 ± 0.14 μm were derived by capacitance and sensitivity measurements respectively. The obtained results are in agreement with the nominal values reported in the manufacturer dosimeter specifications. A homogeneous response was observed over the whole device active area as well. Livingstone *et al.* [8] characterized the PTW microDiamond detector for spatially fractionated fields at the Imaging and Medical Beamline (IMBL) at the Australian synchrotron and reported an energy dependence in the energy range 30–120 keV with a K_Q factor of 1.05 ± 0.09 . Additionally, a dose rate independence from 1–700 Gy/s was also highlighted. The PTW microdiamond detector appears to be suitable for MRT because of its satisfactorily low dose rate dependence. The manufacturer announces a low energy and angular dependence in a range of energy from 100 keV to 1.25 MeV and angles from 0 to 40 degrees.

2 Monte Carlo Simulations

2.1 Introduction of Monte Carlo simulations

Most statistical systems cannot be solved explicitly, or no tidy formula for the equation of the partition function can typically be found. Simulation becomes therefore a powerful tool for extracting answers out of statistical processes for realistic systems [55]. Monte Carlo (MC) simulations are designed to extract mean values of an observable physics quantity which is the result of a large number of random events. Each event is governed by a statistical law that can be known or approached. The required number of events needed to obtain the physical observable quantity of interest through exact analogue simulations is so big in most cases that it cannot be calculated analytically.

The first MC method was applied by the Comte de Buffon in 1777 with the needle tossing experiment to calculate the value of π . This experiment considers needles to be thrown many times on a parquet floor. The parquet is made of parallel boards of the same width. A ‘success’ is counted when a needle straddles two different boards. The more needles are thrown, the more the ratio between success and failures reaches a certain number that relates to π . For instance, if the needle length is equal to the board width, then this number is $\frac{2}{\pi}$.

Another method to calculate π has been developed by Laplace in 1886 using a circle within a square. The same principle of success/failure is applied and the ratio leads to the value $\frac{\pi}{4}$.

In 1930, Enrico Fermi used a random sampling algorithm to estimate the quantities involved in controlled fission, and the newly discovered neutron. During the Los Alamos project in the 1940s, Von Neumann and Ulam coined the term Monte Carlo to describe this kind of simulation and used it for simulating exponentially distributed flights based on material cross-sections for neutrons. Those calculations were performed on hand calculators by efficient technicians and later on analogue computers such as the FERMIAC and the ENIAC to allow the calculation of a large number of histories to get robust statistics. Mathematically, the MC method can be defined as follows:

- **Generate** N random histories which result in N random vectors \vec{x}_i .
- **Calculate** the mean and variance of the distribution $f(\vec{x}_i)$:

$$\langle f \rangle = \frac{1}{N} \sum_{i=1}^N f_i \quad (13)$$

$$\langle f^2 \rangle = \frac{1}{N} \sum_{i=1}^N f_i^2 \quad (14)$$

- **According to** the Central Limit Theorem, for a large number of events N , the value of the estimator $\langle f \rangle$ approaches the true value \bar{f} , the mean value of the Normal law described by:

$$\frac{\exp(-(\langle f \rangle - \bar{f})^2/2\sigma^2)}{\sqrt{2\pi}\sigma} \quad (15)$$

$$\sigma^2 = \frac{\langle f^2 \rangle - \langle f \rangle^2}{N - 1} \quad (16)$$

This means that the greater the number of events, the more precise the calculation of $\langle f \rangle$ becomes. Which leads to one major drawback in Monte Carlo: time. One could say the longer the better, but usually reaching a defined uncertainty is enough to form conclusions.

Time issues are application dependent, for instance in clinical medical physics, a treatment plan should be calculated in 10 to 15 minutes to deal with the number of patients to be treated. Considering the voxelized geometry of the CT scans, the different number of irradiation ports and the large number of different materials, MC simulations for clinical purposes can take up to 15 hours for one patient. Considering the fact that the dosimetry out of the calculation could not be optimized, another 15 hours should be added.

On the other hand, a 24-hour calculation in research is considered an acceptable time as the outcome of a research calculation is not as crucial as a treatment plan for medical purposes. This chapter will introduce the MC method in the specific field of radiation transport through the description of the key components and quantities of a simulation. The time issue will be discussed and methods to overcome this problem will be presented. Finally, a benchmark of 3 widely used MC codes will be presented, with a specific attention brought on the behaviour of these codes in the application for MRT.

2.2 Monte Carlo in radiation transport

MC simulations can be either very simple (calculation of π) or complicated to implement. The level of difficulty is determined by the purpose of the code. For medical applications, MC simulations involve numerous mandatory elements, the accuracy of which in terms of description will influence the accuracy of the result.

This section will introduce the key components of a MC code for medical application purposes.

2.2.1 Random Sampling Methods

The very first component of a MC code is the numerical sampling of variables with specified probability density functions $p(x)$ (PDFs). In most cases, random sampling algorithms use random numbers ξ uniformly distributed in the interval $(0, 1)$. Reliability of the random number generators (RNG) will not be broached here but relevant information about it can be found in Hellakalek, 1998, *Good random number generators are (not so) easy to find* [56].

The main important aspect to bear in mind about random numbers is that they can be easily generated by a computer [57]. Among the currently available RNG, one commonly used is called the multiplicative congruential generator [58]. It produces a sequence of random numbers considering a given ‘seed’ used as an input. This algorithm remains deterministic though, this is why the name pseudo-random would be more appropriate. One key characteristic of the random number used in Penelope is that it generates pseudo-random numbers with a period of 10^{18} , this makes it very unlikely to generate twice the same particle with the same history (which does not improve the statistical uncertainty of the calculation) as in this work the number of histories varies between 10^8 and 10^9 .

2.2.1.a The inverse-transform method

From the particle source properties to the interaction of a particle with matter, most of the processes involved in a MC calculation in radiation transport follow a certain PDF different from the uniform distribution. As an example, a uniform square source model can use the RNG as it is, but in the case of a point source emitting uniformly and isotropically in space, some transformation has to be made. The same principle applies with the sampling of the interaction depth of a photon; the interaction probability in depth follows a decreasing exponential law and is certainly not uniform.

The method to generate random numbers that follow a known PDF is called the Inverse-Transform method.

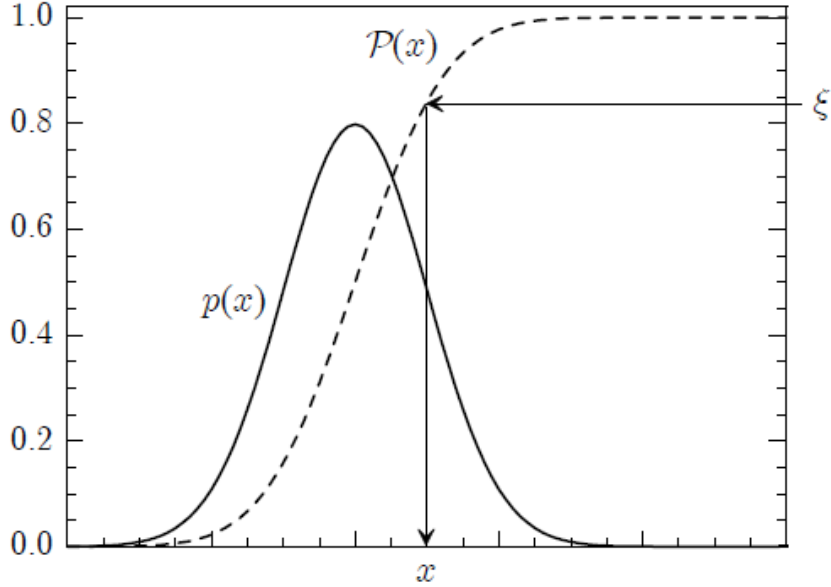


Figure 20: Random sampling using the inverse transform method [5]

The first step of this method is to calculate the cumulative distribution function of $p(x)$. By definition the cumulative distribution function is non-decreasing, therefore has an inverse function $P^{-1}(\xi)$. This new function $\xi = P(x)$ utilizes the uniformly distributed RNG that take values in the interval $(0, 1]$ to produce random numbers that follow the distribution $P(x)$.

Figure 20 shows both basic and cumulative function and the correspondence between ξ and x . It is important to notice that the randomness of $P(x)$ is ensured by the randomness of ξ . This procedure is particularly adequate for distributions with analytical expressions because the sampling equation can be solved analytically. On the other hand, it remains achievable to apply the inverse transform method on unknown functions such as photon spectra which admit a strictly increasing cumulative distribution function.

As an example the following equations describe how the depth of the interaction of a photon in matter is sampled using the Beer-Lambert law with a uniform random number ξ as an input:

The exponential distribution is defined as:

$$p(x) = \frac{1}{\lambda} \exp\left(-\frac{x}{\lambda}\right), \quad (17)$$

with x the free path of the interaction event and λ the mean free path. We calculate the

cumulative distribution function:

$$\xi = \frac{1}{\lambda} \int_0^s \exp\left(-\frac{x}{\lambda}\right) dx = \left[-\exp\left(-\frac{x}{\lambda}\right) \right]_0^s = 1 - \exp\left(-\frac{s}{\lambda}\right) \quad (18)$$

$$\Rightarrow \ln(1 - \xi) = -\frac{s}{\lambda} \quad (19)$$

$$\Rightarrow s = -\lambda \ln(1 - \xi) \quad (20)$$

Equation 20 provides the depth of interaction of a photon of mean free path λ considering the uniform random number ξ .

2.2.2 Geometry description

Geometry is an essential part of a MC code for medical applications. A versatile geometry tool allows the modelling of complex geometries such as for example a dosimeter, including all sensitive / non-sensitive components with proper dimensions. This complexity can be pushed towards using a voxelized geometry provided by a computed tomography (CT) scanner and hence being as faithful as possible to the real patient morphology.

In Penelope, this task is handled by the package Pengeom [59] where volumes are described as ‘bodies’ delimited by surfaces.

Each surface is defined in a geometry input file and combined together to produce the bodies. For example, a cube is defined by 6 planes $x = 1, x = -1, y = 1, y = -1, z = 1, z = -1$. The surfaces are oriented to fill the inside of the cube with a material, or the outside depending on the desired geometry.

The way this geometry is used is straightforward. Let’s consider a photon emitted in a basic cubic geometry. The depth of interaction is computed with equation 20. This position is compared to the limits of the previously defined cube. If the interaction point is inside the cube, the type of interaction is chosen randomly according to material and energy dependent cross-sections (defined later in this chapter) otherwise the photon interacts in a ‘void’ material hence nothing happens. The photon is ‘killed’ and a new one is generated.

For the user, a geometry package associated with a Monte-Carlo code is reduced to learning a syntax of getting used to a Graphical User Interface (GUI).

2.2.3 Cross-section data

In equation 20 the parameter λ is the mean free path of a particle. This mean free path is related to a physical quantity called the interaction cross section σ as follows:

$$\lambda = \frac{1}{N\sigma}, \quad (21)$$

where N is the number of target particles per unit volume.

The interaction cross-section σ is expressed in barns (10^{-32}cm^2) and is a quantity that is particle, material (atomic number and density) and energy dependent. In equation 20, the lower the mean free path and the higher the cross-section, the greater the probability of interaction by the photon.

This interaction probability is called the total interaction cross-section as the photon can interact through different mechanisms, each one is associated with its own interaction probability.

The total interaction cross-section is defined as the sum of all cross-sections corresponding to the previously introduced events, as shown in Figure 21:

$$\sigma_{total} = \sigma_{PE} + \sigma_{inc} + \sigma_{Ra} + \sigma_{PP} \quad (22)$$

2.3 Time issue in MC simulations

In MC and more specifically in MRT, the calculation time remains a major issue. A conventional CT scanner performs images with a spatial resolution of 0.5 mm, thus statistics are ‘rapidly’ acquired to reach the desired uncertainty. The size of the pixels is good enough considering the field sizes routinely used in conventional RT since the spatial variations of the beam intensity are very slow.

In MRT, the field spatially varies rapidly, and produces micron length areas where dose gradients are steep. In order to account for this localized behaviour in MC, the 3D dose distribution has to be recorded with voxels smaller than the measured effect in size (1 μm is optimal). In this work, the MC study of the PTW microDiamond detectors forces

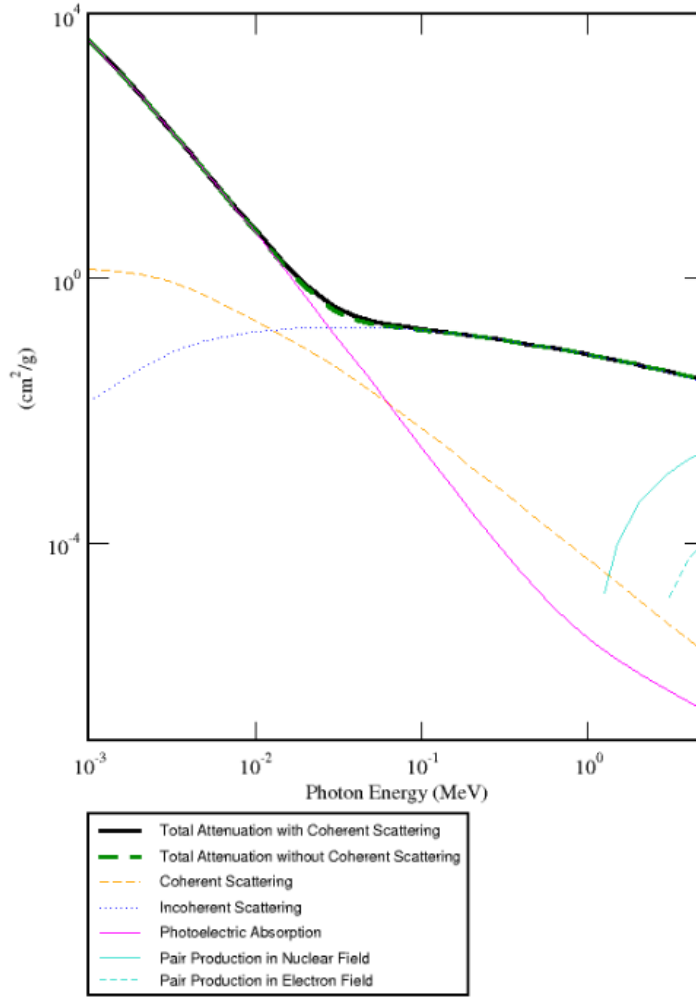


Figure 21: Water interaction cross sections [9]

the use of a 1 μm thick sensitive volume which is a major cause of increased calculation time. As a matter of fact, recording an interaction in the PTW microDiamond sensitive volume can be estimated as being 460 times less likely to happen than in the rest of the geometry for a $2\text{ cm} \times 51\ \mu\text{m}$ microbeam. For a $2 \times 2\text{ cm}^2$ spatially fractionated field with 50 μm wide microbeams spaced with 400 μm c-t-c spacing, only 1 event out of 22,000 can produce a relevant event in the sensitive volume.

Another aspect to be considered is the writing time. The greater the number of voxels, the longer it takes to write down the results. It is recommended writing partial results regularly to create recovery points during the calculation to avoid starting the simulation

from scratch in case the of problems. As a consequence, the calculation time increases with the number of back ups performed during the simulation.

Commonly used MC codes provide variance reduction (VR) techniques built in the code. They are designed to reduce the statistical uncertainty of a physical quantity without increasing the computation time. Unfortunately, these optimizations are extremely problem dependant and general recipes to minimize the variance cannot be given [5]. In this work, the importance of variance reduction is obvious. However, built-in variance reduction techniques such as Russian roulette or particles splitting will be a last resort. We will present a few techniques that can be implemented to speed up the calculation. Of course designing such simulation requires man time, but this work is an exploration of the possibilities and knowledge from the following chapter is used to speed up the next calculations.

2.3.1 Speed-up through the geometry

The accuracy of the description of the geometry is crucial in a MC problem. Fully modelled geometry and what we will call from now on, ‘forward calculations’, is not always required. In this section, a method called the semi-adjoint MC technique is presented. This method switches the detector and source dimensions. Using the semi-adjoint technique reduces the calculation time as mentioned previously but also allows to simulate various source geometries with one single simulation where forward MC simulations would require more simulations. This technique is applied to OF’s and PVDR’s calculations. The theory of semi-adjoint MC simulations is explained in [60] [61]. Developing the whole theory here is not the point; furthermore, it has already been written in a MRT related PhD thesis by Bartzsch [10] in addition to a quantification of the enhancement associated with the use of the technique. Instead a description of how the semi-adjoint technique is applied in MRT is provided.

2.3.1.a Applying Semi-adjoint MC simulation in MRT

As a reminder, in MRT one microbeam width is 50 μm , 2 cm in height and the centre to centre distance is 400 μm . A forward MC calculation of the OF at 2 cm depth for a $2 \times 2 \text{ cm}^2$ field would be to first simulate a microbeam with such dimensions, to score the dose deposited in a 3D grid with a $1 \mu\text{m} \times 1 \text{ mm} \times 1 \text{ mm}$ with limits in $X = [-1 \text{ cm}, 1 \text{ cm}]$, $Y = [0, 10 \text{ cm}]$, and $Z = [-1 \text{ cm}, 1 \text{ cm}]$. According to equation 9 another simulation involving a $2 \times 2 \text{ cm}^2$ field with the same dose scoring is needed. When forward calcu-

lations are used, results are not versatile, which means that they cannot be extrapolated to other irradiation conditions. If another OF definition involves a microbeam with another width, the user has to run other calculation to account for the change in the beam dimensions.

The dimension of the source can then be reduced to a point and the scoring volume to $1 \mu\text{m} \times 1 \text{ cm} \times 1 \text{ mm}$ is used with limits from $X = [-3 \text{ cm}, 3 \text{ cm}]$, $Y = [0, 10 \text{ cm}]$, and $Z = [-1 \text{ cm}, 1 \text{ cm}]$. The scoring volumes in MRT have to remain small since dose changes at the micron scale. Nevertheless the improvement in terms of statistical noise reduction and calculation time is real as shown in Figure 22 for the calculation of the valley dose in MRT. The valley dose is crucial to assess accurately but its simulation is long because it is built up with scattered radiation. Applying the semi-adjoint simulation allows the use of a lower number of histories and does not require any PSF for the source description.

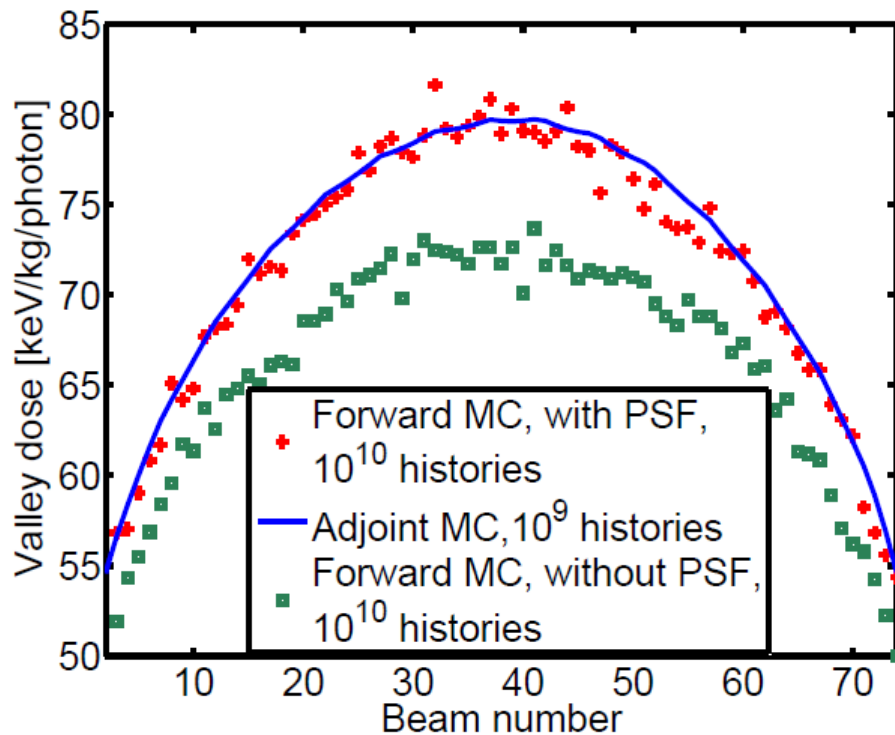


Figure 22: Comparison forward calculation/ semi-adjoint theorem [10]

Figure 23 displays the OF as a function of the width of the microbeam. OF is calculated from one single simulation whose result is a kernel generated by the point source. The extrapolation of the microbeam width $W(x)$ is performed by convolving this kernel $K(x)$ with a rectangular function $\Pi_L(x)$ of increasing the width L :

$$\Pi_L(x) = \begin{cases} 1/L & \text{if } |x| < L/2 \\ 0 & \text{if } |x| > L/2 \end{cases} \quad (23)$$

with x the distance within the field. The numerical convolution is computed by:

$$W(x) = \sum_{x'} K(x') \Pi_L(x - x' + 1) \quad (24)$$

Figure 9 shows the definition of OF and PVDR, both graphs are generated from a single kernel obtained with the semi-adjoint simulation. Microbeam width and c-t-c spacing become numerically tunable parameters, leading to a improved potential of study in MRT.

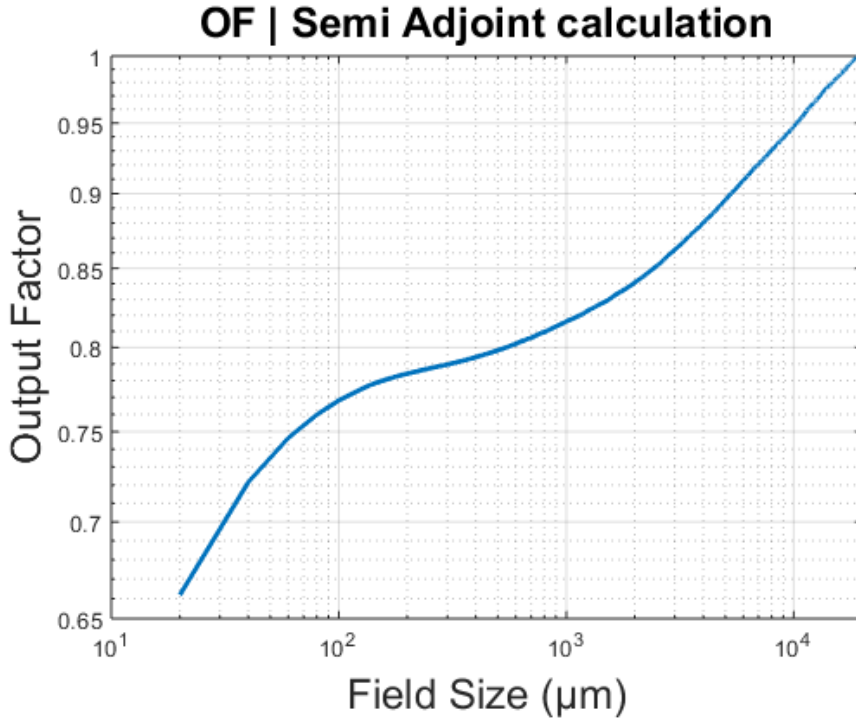


Figure 23: OF versus microbeam width calculated with the semi-adjoint MC.

2.3.1.b Adapting the geometry and particle cut-offs

A MC simulation in radiation transport focuses on events happening to a particle from its creation until its disappearance. The tracking of a particle stops when it has deposited all of its energy. A charged particle undergoes more interactions when its energy decreases, as a consequence, following the state of a particle until it has transmitted all its energy can take too long. To overcome this problem, the user has to define cut-offs for each particle. A cut-off is an energy below which the particle is disregarded and its energy is locally absorbed. For example, let us consider the MSC made of WC, placed 1 m prior the patient as an input geometry for a MC calculation. The source is a broad beam 2 cm wide and 0.0520 cm high irradiating the MSC, thus creating the spatially fractionated irradiation field. X-rays that interact in the MSC that are not transmitted put electrons in motion in the MSC. It is impossible for one of these electrons to reach the patient and play a significant role in the dose deposition at 2 cm depth. Setting the electron cut-off to the maximum photon energy value in the MSC allows then a substantial speed-up of the calculation.

The interaction medium can be segmented in regions with decreasing cut-offs.

A segmentation like the one displayed in Figure 24 allows the simulation to disregard events that will not produce relevant information. In this example, if the high cut-off is set so that the maximum distance possible for an electron in the media is lower than the depth of the second region (medium cut-off), none of the electrons produced will reach the sensitive volume.

The dimensions of the sensitive volume can be adapted as well depending on the nature of the problem. If the dose is scored in a region where dose gradients are not steep, the sampling of the dose profile can be less accurate as spatial variations are very low (the tip of the peaks or the middle of the valley dose). Typically, a scoring region of 1 μm of the dose profile for a $2 \times 2 \text{ cm}^2$ field at 2 cm depth with microbeams 50 μm wide 400 μm c-t-c spacing produces a difference of 0.07% on the OF value compared to a grid with 5 μm wide voxels. In the following paragraphs a quantification of the enhancement by increasing the sensitive volume will be shown.

2.3.2 Speed-up by mimicking the scanned irradiation

In MRT the constraints due to the beam dimensions make the irradiation procedure different from conventional radiation therapy. Indeed, the synchrotron generated beam is

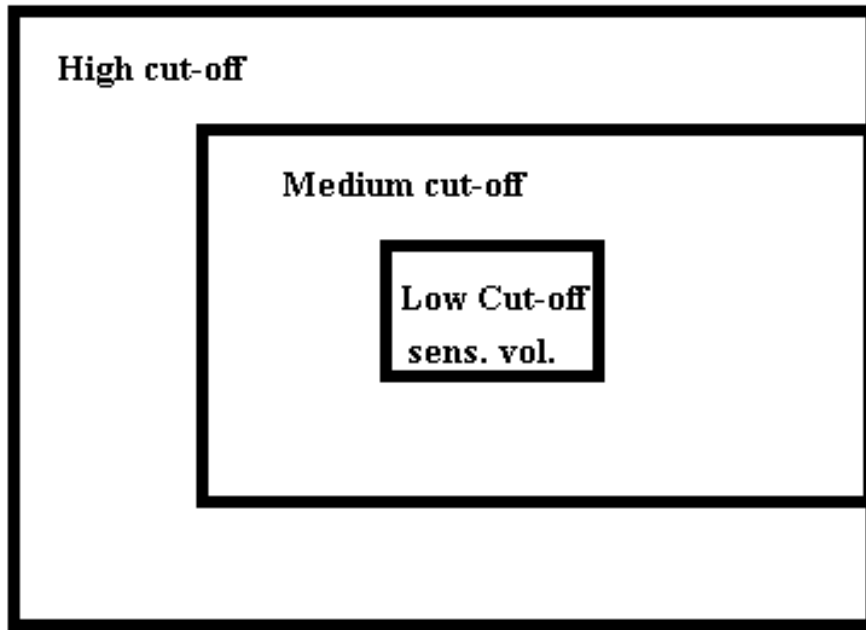


Figure 24: Diagram of cut-off repartitions in a target media. Cut-offs are decreased with distance to the sensitive volume

0.52 mm high and up to 3 cm wide in a static horizontal plane. So the irradiation of a tumour greater than 0.52 mm is performed by scanning the patient vertically through the beam. By tuning the slit opening ahead of the patient it is possible to choose the lateral opening of the field. The combination of the aperture of the slit and the patient scanning offers the possibility to realize field sizes like 2 cm \times 2 cm, 3 cm \times 3 cm and others.

In the SSRT literature, Prezado [47] *et al.* demonstrates the equivalence between measuring the dose in a broad beam by scanning a thin beam over the same dimension as the broad beam. In their approach they make the hypothesis that the thin beam is homogeneous, which is not the case at all in MRT.

In order to verify the equivalence between the deposited dose after a scanned irradiation and the measured dose during the scanned irradiation, two MC calculations are made. In both simulations the irradiated medium is a water tank (18 cm \times 18 cm \times 18 cm). In simulation No. 1 the beam is 0.52 mm high and 2 cm wide, fractionated in microbeams 50 μ m wide spaced with 400 μ m. The dose is recorded in a cube 2 cm high, 8 cm deep and 2 cm wide. The dose is calculated by integrating over the height (2 cm) to emulate the scanning of the beam. The simulation No. 2 considers a fractionated beam

2 cm high and 2 cm wide with same c-t-c distance and width as in simulation No. 1. The dose is recorded in the same grid as in No. 1 and the dose profile is extracted from the centred plan of the field. Figure 25 shows peak to valley dose ratios from simulation No. 1 and 2, supposed to respectively represent the measurement made during a scanned irradiation and the dose deposited by a scanned irradiation.

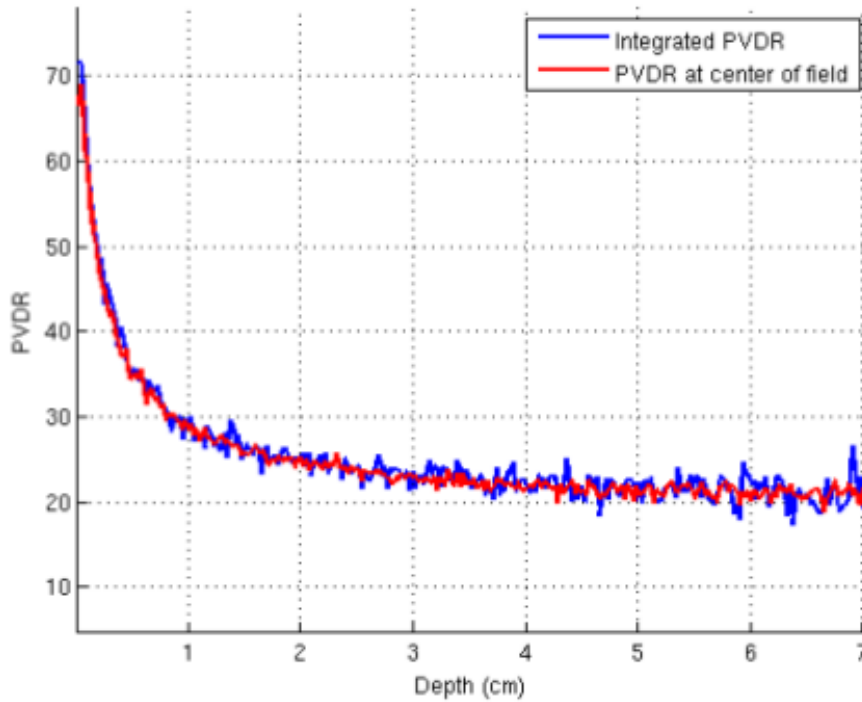


Figure 25: Integrated PVDR over 2 cm from an irradiation with a 0.52 mm high beam and central profile from a 2 cm high beam irradiation

The results of the two simulations highlight the fact that measuring by scanning the detector through the 0.52 mm high beam is equivalent to a static measurement from a 2 cm high beam irradiation. This result is mainly useful in terms of calculation speed enhancements. It is a lot more accurate to sample a 0.52 mm high beam and integrate rather than a 2 cm high beam.

2.3.3 Speed-up through the Parallelization of PENELOPE

The use of Monte Carlo (MC) methods for dose calculation in microdosimetry is limited by the voxel size of sensitive volumes, therefore the computation time needed to achieve

a dose calculation with the adequate accuracy increases. In smaller voxels the number of events is reduced and impoverishes the statistical uncertainty. This effect is enhanced in MRT because of the spatial fractionation of the beam. In the region between the peaks, the dose deposition is only due to scattered radiation, for which the number of events is significantly lower than on the path of primary photons. Moreover, microdosimetry involves 3D dose maps over a large number of voxels ($40,000 \times 50 \times 50$) and the voxel size is $1 \mu\text{m} \times 1 \text{mm} \times 1 \text{mm}$. As the PVDR is the parameter of therapeutic importance in MRT, a sufficient statistical uncertainty is required for both the peaks and valleys measurements for several depths and field sizes. As a consequence the combination of small voxel sizes and spatial fractionation leads to a large increase in the dose calculation time. The code PENELOPE was first parallelized by Salvat et al. [5] using the MPI distributed memory message passing library and ran on eight processors at the Centre de Supercomputaci3n de Catalunya (CESCA). Later in 2003 R.B. Cruise and al [62] parallelized the code PENELOPE at the University IBM Teraflop SP using the parallel random number generator (p.r.n.g) developed by the MILC lattice-QCD collaboration [63] Both codes have been tested and validated in terms of dose map calculations.

The main idea of this work is to create a custom version of the code PENMAIN allowing parallel computation of microbeams. This work is strongly based on the studies of J.Sempau and R.B. Cruise.

2.3.3.a Structure of the parallel code

Parallelizing PENELOPE is a process called Single Program Multiple Data (SPMD). In this kind of code, each parallel processor will consider the exact same set of input parameters, such as the irradiation geometry, materials, the initial particle spectrum, etc., and generate its own set of trajectories. Each processor keeps tracks of the relevant quantities during the whole calculation and once all the processors are finished, the results from each processor are gathered by the root processor to generate the final output files. One key aspect of SPMD is that the processors do not have to communicate with each other during the calculation. This is convenient as the evolution from sequential (code running on one single processor) to parallel can be achieved by small changes in the original sequential code.

As mentioned above, SPMD means that the exact same program is run by all the processors, as a consequence, special attention should be paid to the random number generator

(RNG) to ensure the statistical independence of the simulation performed by each processor. If the RNG is not modified properly, each processor will perform the exact same set of trajectories and as a result no statistical noise reduction improvement occurs and the parallelization is pointless.

To implement a SPMD, the standard Application Programming Interface (API) called MPI (Message Passing Interface) is used. This parallelization is performed using Intel MPI version 4 and capitalizes on a library of subroutines designed to manage interprocessor communication. MPI assigns each processor a unique identification number which is used to initialize the RNG and distribute statistically independent jobs to each processor.

2.3.3.b Parallelization of the PENMAIN subroutines

Originally, the PENELOPE's random number generator was the subroutine RAND written in the `rita.f` source code. The function RAND is initialized with a pair of numbers (1.1). This function as it is cannot be used for parallelized computing as the sequence generated for each processor remains the same.

One of the improvements in the development of PENELOPE in the last decade is the addition of the function RAND0. This function includes a pre-computed list of seeds (1000 pairs at the total) that belongs to the sequence from RAND and whose relative separation is 10^{14} calls. In other terms, starting with the n -th seed pair allows 10^{14} calls of RAND before obtaining the $(n + 1)$ -th pair. RAND0 takes the parameter n as an entry and starts the simulation with the n -th pair of seeds.

The only subroutine that needs to be modified to ensure the statistical independence of each processor's calculation is PMRDR in the `penmain.f` main source code. PMRDR is the first subroutine to be called by the main program. Originally this subroutine does not take any argument as an input, but only reads the input file and sets up the variables needed for the simulation accordingly. The simulation parameters must remain the same for all the processors except for the seeds that must be different for each processor and the number of simulated showers which should be set as the total number of showers requested NSH divided by the total number of processors NUMPROC. The first step is then to modify the declaration of PMRDR as follows:

```
SUBROUTINE PMRDR(rank , numproc)
```

and the call of the subroutine accordingly. Here `rank` and `numproc` are variables defined

in the main program and represent the rank (label) of a processor and the total number of processor requested for the simulation respectively. Then in the input file write the line `RSEED -1 1`. The value -1 is read by PMRDR and stored in the variable `ISEED1`. Inside PMRDR at the location where the value of `ISEED1` is tested modify the code as follows:

```
IF (ISEED1.LT.0) then
ISEED1=-rank-1
CALL RAND0(-ISEED1)
```

This produces a different seed from `RAND0` depending on the rank of the processor calling the subroutine.

In the input file the requested number of histories is called with `NSIMSH 1e8` (requesting $1e8$ histories in this example). This value is then stored in the variable `DSHN`. In `penmain.f` in the subroutine `PMRDR`, the line where the subroutine reads the value `DSHN` has been modified accordingly.

```
READ(BUFFER,*) DSHN
NTOT=DSHN/(numproc)
IF (rank .lt. (DSHN-NTOT*(numproc))) NTOT=NTOT+1
DSHN=NTOT
```

This piece of code divides the number of requested showers between the processors. The shower simulation now loops over a counter ranging from 1 to `NTOT`.

2.3.3.c Parallelization of the Main Program PENMAIN

The PENELOPE code is based on subroutines. The user is then free to develop his own main code which repeatedly calls PENELOPE's subroutines to generate trajectories and compute averages.

As with all FORTRAN codes the user has to declare the file containing the MPI dedicated libraries as follows:

```
INCLUDE 'mpif.h'
```

The first task is to initialize the MPI API and assign each processor a unique ID (variable `rank`):

```
call MPI_INIT(ierror)
call MPLCOMMRANK(MPLCOMMWORLD, rank, ierror)
```

Then each processor needs to access the total number of processors `numproc`:

```
call MPLCOMM_SIZE(MPLCOMMWORLD, numproc, ierror)
```

Here `MPI_COMM_WORLD` is called a communicator, all MPI communication calls require a communicator argument and MPI processes can only communicate if they share a communicator. At this stage, the code runs any desired number of statistically independent simulations in parallel. The next important step is gathering results from all the processors and adding them up together. This is achieved by declaring the dual of almost all the common blocks declared in the file `pmcomms.f` in the main program. Attention should be brought to the variables which are table sizes and which should not be added up together.

The `COMMON_BLOCK` at the beginning of the subroutine `SDOSE` must be copied and paste and added to the main program as well as creating dual variables as follows:

```
COMMON/DOSE(NDXM, NDYM, NDZM)
```

Which defines the variable `DOSE` as common and

```
double precision myDOSE(NDXM, NDYM, NDZM)
```

Which is the dual variable of `DOSE`. Once this step is achieved for each and every quantity needed to be tracked in the parallel calculation, adding up the results of each processor is performed with one single command:

```

      call MPLREDUCE(DOSE,myDOSE, size(DOSE) ,
+  MPI_DOUBLE_PRECISION, MPLSUM, 0 ,MPLCOMMLWORLD, ierror )

```

Where the different values of DOSE in the different processors are added and stored in myDOSE.

In order to benefit from PENELOPE's subroutine to write down the output files, ask the processor 0 to copy the dual variables in the regular variables and call the subroutine PMWRT:

```

      if (rank .eq.0) then
        DOSE=myDOSE
        call PMWRT(1)

```

Finally the communicator is closed with:

```

      call MPI_FINALIZE(ierror)

```

The quantification of the speed enhancement of the parallelization is presented in the next paragraph.

2.3.4 Quantification of speed enhancement

In order to quantify the enhancement of the different procedures previously described, a MC simulation is designed. The geometry of the PTW microDiamond detector has been coded using the software PENGINEOM.jar provided by the package PENELOPE. A section of the geometry is shown in Figure 26. The pink volume at the centre of the image is the 300 μm carbon substrate. At the top of the substrate the 1 μm sensitive volume is located. The surrounding materials and dimensions will not be given here.

The digital PTW microDiamond is placed in a PMMA tank $20 \times 20 \times 20 \text{ cm}^3$ with the centre of the sensitive volume located at 2 cm depth.

The beam is a single microbeam 2 cm high and 51 μm wide, sampled from the ID 17 MRT spectrum. The sensitive volume is placed at the centre of the microbeam. The dose and its associated uncertainty are recorded in the sensitive volume for a range of different numbers of histories from 10^4 to 10^7 . At lower histories the sensitive volume does not

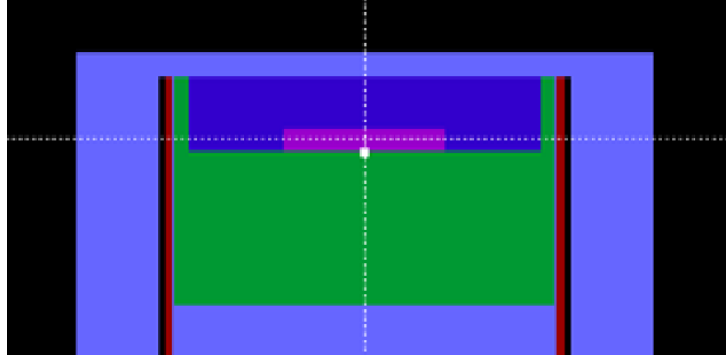


Figure 26: Diagram of the PTW microDiamond detector displayed from `PENGEOM.jar`

detect any particle. The comparison includes a slightly optimized MC simulation with cut-offs placed in the regular geometry (1 keV for photons and electrons). The increase in the size of the sensitive volume is also studied (from 1 μm to 5 μm with the combination of segmentation/cut-offs (decreasing from 100 keV to 1 keV). Finally, the parallelized regular simulation over 10 processors is tested. Dose, uncertainty and calculation time are gathered for each simulation and number of histories to evaluate the efficiency. Figure 27 displays the figure of merit (FOM) depending on the applied technique. The FOM is defined as follows:

$$FOM = \frac{1}{R^2 T} \approx \text{const}, \quad (25)$$

where T is the simulation time and R is the relative error expressed by:

$$R = \frac{\Delta \bar{D}}{\bar{D}} \propto \frac{1}{\sqrt{N}}, \quad (26)$$

with $\Delta \bar{D}$ the statistical uncertainty on the mean value \bar{D} and N the number of histories.

The FOM can be interpreted as:

A reliability indicator for a tally; it must be constant except for small statistical variations

A measure of the efficiency of the MC calculation; the higher the FOM the better the efficiency.

A useful tool for estimating the time needed to achieve a given statistical precision.

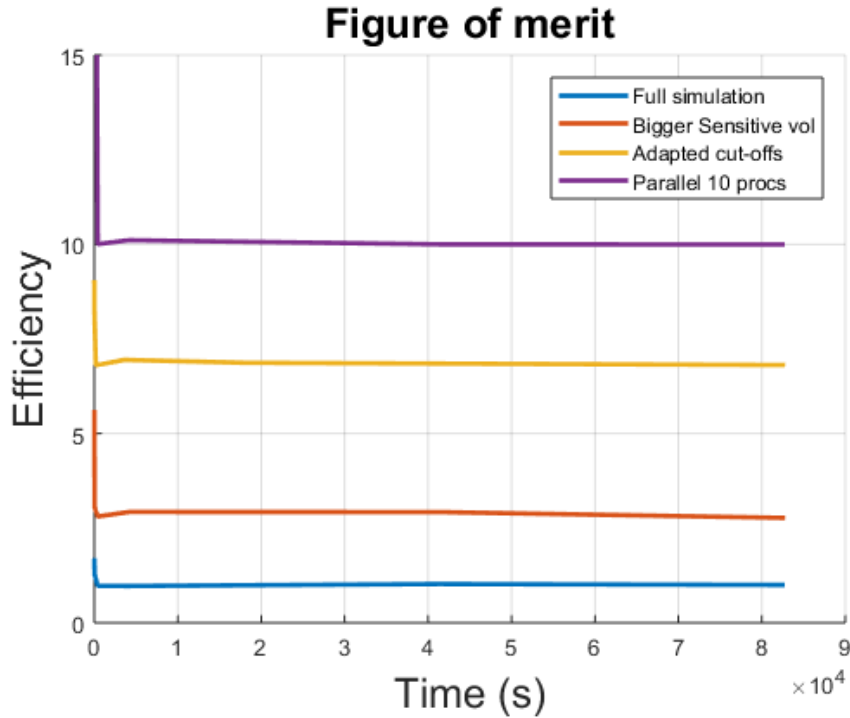


Figure 27: FOM for enhanced MC simulation normalized to the full simulation.

In Figure 27 values of the efficiency are normalized to the plateau value of the full simulation. Therefore, when the FOM reaches a constant value, this latter corresponds to the enhancement in terms of time for achieving the same precision.

As a result, the increase in sensitive volume from $1 \mu\text{m}$ to $5 \mu\text{m}$ reduces the simulation time by a factor of 3. Building a segmented geometry with wisely chosen cut-offs makes the simulation 7 times faster and the parallelization increases the efficiency by a factor of 10.

2.3.5 Particle splitting simulations

The simulation of a measurement with the PTW microDiamond detector has to account for the whole geometry of the detector and the MRT hutch. As a consequence, the semi-adjoint MC simulation cannot be applied. Moreover, the PTW microDiamond detector provides the measurement at one single location within the field, thus one simulation per measurement point is required to reconstruct the dose profile. Statistics can be quickly acquired for measurement points on the path of the primary photons but the accuracy decreases with distance to the beam axis at fixed number of histories. The combination

of a large number of simulations and their associated uncertainty makes the estimation of the measurement with the PTW microDiamond detector a very long task.

A procedure is presented here to increase the efficiency of particle detection at large distances from the central microbeam to evaluate the measurement of OF and PVDR at 2 cm depth. The main idea of the procedure is based on importance sampling [64]. What is meant here by importance sampling is a way to associate a larger statistic importance to an area of greater interest. The thin sensitive volume of the PTW microDiamond detector is a region in the geometry where particle interactions are rare. Using particles splitting with conditions on the labels on different bodies of the geometry is one solution. In PENELOPE, the geometry construction is performed from the most central volume (BODY 1) to the biggest. The sensitive volume is chosen to be BODY 1 and is embedded in all the rest. The following procedure affects the parameter NSPLI1=100 to each BODY and has to be inserted in penmain.f at the end of the subroutine SHOWER():

```

      DO KB=NBODY,1,-1
C  —— Splitting .
      NSPLI1=100
      IF (NSPLI1.GT.1) THEN
          CALL VSPLIT(NSPLI1)
C  —— Energy is locally deposited in the material .
          DEP=(NSPLI1-1)*E*WGHT
          DEBO(IBODY)=DEBO(IBODY)+DEP
          IF (LDOSEM) THEN ! Particle inside the dose box .
              CALL SDOSE(DEP,X,Y,Z,N)
          ENDIF
      ENDIF
ENDDO

```

NSPLI1 is the parameter that controls the splitting of the particles. One particle that enters a BODY with NSPLI1=100 is copied 100 times and simulated using a second RNG to ensure that these particles undergo different events. The call of the subroutine VSPLIT(NSPLI1) realizes the splitting and computes WGHT which is the weight associated to the particle that deposit its energy. SDOSE(DEP,X,Y,Z,N) writes down the results in the output file. The procedure is embedded in a loop over labels of bodies, this way the area with the maximum splitting is the sensitive volume. Duplicated particles and their descendants will be stored in the secondary stack which should be increased accordingly.

The variable `NMS` in `penelope.f` initially set to 1000 is increased to 100000 for the purpose of this job. Increasing the size of the secondary stack is crucial otherwise particles with the lowest energy will be deleted, generating a lack of accuracy in the results.

This method will be used in the final chapter to estimate the correction factors to be apply to measurements performed with the PTW microDiamond detector.

2.4 Benchmark of the MC codes

In MRT, the peak dose is lethal to the cells while the valley dose has to remain under the tissue tolerance. Both peak and valley doses are mainly due to Compton events, the only difference is that the peak dose is due to primary events, and the valley dose from events that follow the primary interaction. Thus the accurate modelling of the Compton scattering at the micron scale and a consistency in the result of the Monte Carlo (MC) codes used to predict dosimetric quantities are expected. The main motivation for this work is that discrepancies between output factor simulations for MRT were found in the literature [38] between Penelope and Geant4 combined with an inability to retrieve such results experimentally.

This study involves three MC codes EGSnrc [65], GATE (Geant4) [66] and Penelope [5, 67, 68]. EGSnrc and Penelope are based on the Ribberfor's scattering model, the Double-differential Compton scattering Cross-Section (DDCS) in the Relativistic Impulse Approximation (RIA) [5].

This method has been developed to account for the scattering of a bound electron considering its binding energy and pre-collision momentum of the target electron [69] whereas using the simple Klein Nishina formula for free electron scattering. This binding effect becomes noticeable in terms of Doppler broadening of the scattered photon's energy distribution for energies lower than 5 MeV and hence has to be accurate in MRT. EGSnrc uses a class II condensed history technique for the simulation of the charged particle transport [5, 70–74] [75–77]. Total theoretical and differential cross sections are used. The user has the choice between using the free electron approximation (Klein-Nishina) or the relative impulse approximation to allow binding effect and Doppler Broadening consideration. EGSnrc relies on published cross-sections data from Storm and Israel (1970), EPDL(Cullen et al. 1997) [32] or Berger and Hubbel 1987 [9] depending on the user's choice. Geant4 is an object-oriented `C++` toolkit that allows the simulation of a large variety of particles and physics processes over a wide range of energy. The user can define which physics processes to be involved in the calculation in the 'Physics

List'. In this study, the Physics List adopted is `emstandard-opt4`. In terms of Compton scattering modelling `G4EmStandardPhysics-option4` encompasses 2 implementations of the Compton effect. The first one uses a free electron Klein-Nishina model for energies over 20 MeV. Below this threshold value the `G4LowEPComptonModel` is used. The `G4LowEPComptonModel` [78], utilizes the Monash University Compton Scattering algorithm as an alternative to Ribberfor based algorithms. The cross section data are from EPDL (Cullen et al. 1997). The Compton scattering is simulated using the algorithm from Brusa [67] using the impulse approximation and accounting for the binding effect and Doppler broadening below 5 MeV. The cross section data used is from EPDL (Cullen et al. 1997). Microbeam dosimetry has been studied in the past using MC simulations [1, 3, 79, 80]. Different codes have been investigated such as GEANT4 [10, 81, 82], EGS4 [79, 83], EGS5 [84] and PENELOPE [3, 12, 80]. De Felici [85] compared EGS4, EGSnrc, PENELOPE, GEANT4 and MCNPX using the same irradiation conditions and geometries involving 25 μm wide cylindrical and rectangular microbeams. A maximum difference in the dose profile between 10 and 100 μm of 20% has been found for MCNPX and around 19% for EGS4 and GEANT4. The authors limited their studies to a maximum range from 0 to 1 mm away from the microbeam axis with 1 μm wide bins which do not provide information on the long radiation scattered a long way away from the central microbeam. The far from beam axis scattered radiation contributes in the simulation of output factors (OF) and peak to valley dose ratio (PVDR) (defined in the next section), both quantities of interest in MRT to assess the therapeutic outcome and dose delivery during the treatment. The aim of this study is to compare EGSnrc, PENELOPE and GEANT4 for OF and PVDR simulations, and try to understand the source of discrepancies between them.

2.4.1 Material and methods

The comparison of the MC codes is performed using a rather simple geometry. A water/bone (ICRU-44) [86] phantom 6 cm \times 6 cm \times 20 cm with 1201 lines of 50 μm in the X direction, 3 lines of 2 cm in Y and 125 lines of 0.16 cm in Z. The beam is a 2 cm long line along the Y axis centred on the pixel 601 from the X axis. The profiles are recorded at 2 cm depth which is the 13th slice in the Z direction. The ESRF spectrum (figure 28) ranging from 0 to 600 keV is used for the calculation.

GRIDX -3 3 1201 [X coords of the box vertices , no. of bins]

| | | |
|-------|----------|--|
| GRIDY | -3 3 3 | [Y coords of the box vertices , no. of bins] |
| GRIDZ | 0 10,125 | [Z coords of the box vertices , no. of bins] |

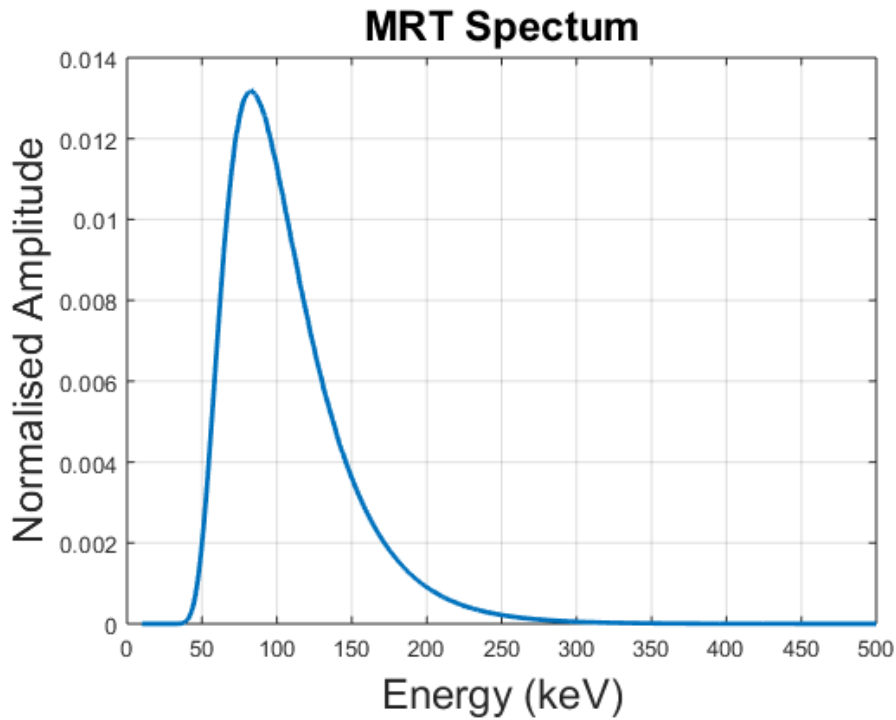


Figure 28: ID 17 medical beamline MRT polychromatic spectrum

The single microbeam profile obtained from the simulation is then used to calculate OF's and PVDR's which are handy relative dosimetric experimentally measurable quantities. The calculation of OF from a single microbeam profile can be achieved because a full field is the sum of any number of 50 μm wide microbeams required to obtain the desired field size. So by adding up the contribution of each voxel from the profile to the central pixel (601) one can obtain the maximum dose for a $2 \times 2 \text{ cm}^2$ field. For the calculation of the PVDR, it is mandatory to account for the centre-to-centre distance (400 μm) and add to the central pixel the contribution of each microbeam by digitizing the single microbeam profile each 5 pixels (400/2). The same calculation is then performed with a disabled electron transport by selecting a cut-off value for the electrons equal to the maximum energy in the spectrum. This way the electron energy is deposited entirely at the location

of the interaction.

2.4.2 Results

OF and PVDR are both subject to 0.7% and 1.5% respectively. The uncertainty on the ratios is calculated using the square root of the quadratic sum of the relative uncertainties leading to a respectively 1% and 2.1%. Table 5 provides the results of the comparison of OF and PVDR values for the three codes.

When electron transport is switched off:

Both GEANT4 and Penelope give higher OF and PVDR values than EGSnrc in water. The agreement between OF values between the codes is within 1% and the difference in the PVDR calculation is up to 1.9% for GEANT4 but still within the uncertainty bars. In bone the agreement is poorer than the simulation in water with a maximum relative difference to EGSnrc up to 1% for the OF calculation and 3.3% for the PVDR.

With electron transport switched back on :

The comparison of OF from EGSnrc, Geant4 and Penelope at 2 cm depth in water highlights some differences up to 2.0%. Geant4 agrees with EGSnrc within the uncertainty bars but Penelope calculates a lower OF. In bone, both GEANT4 and Penelope present a higher OF up 2.6% and a higher PVDR up to 3.9%. The primary dose maximum difference in the central pixel for both electron transport on and off along the whole depth for water and bone is lower than 0.05%; it means that the difference in OF and PVDR values between the codes comes either from photon scattering or electron transport or a combination of both.

Figure 29 displays the OF and PVDR with depth for each code and the percentage difference with respect to EGSnrc along the depth. Error bars are not displayed for a better readability. The latter shows how sensitive to the statistical uncertainty the PVDR measurement is compared to the OF. Regarding the OF in water, GEANT4 and EGSnrc have a close behaviour with higher values than Penelope. The agreement within the codes worsens with depth more rapidly for Penelope than GEANT4 and a similar trend is to be observed for the PVDR. In bone, the OF trend is inverted giving Penelope and GEANT4 closer agreement leaving EGSnrc with a lower value. The agreement worsens with depth as well but seems to plateau around 2.5%.

| | EGSnrc | Geant4 | ≠ to EGSnrc | Penelope | ≠ to EGSnrc | Irradiation conditions |
|------|--------|--------|----------------|----------|----------------|-------------------------------|
| OF | 0.7404 | 0.7365 | -0.38 % ± 1% | 0.7287 | -2.02 % ± 1% | 2x2 cm ² 2 cm |
| PVDR | 28.9 | 29.25 | +1.17 % ± 2.1% | 23.29 | -1.63 % ± 2.1% | depth in water |
| OF | 0.7914 | 0.7960 | +0.58 % ± 1% | 0.7987 | +0.21 % ± 1% | 2x2 cm ² 2 cm |
| PVDR | 31.44 | 32.04 | +1.89 % ± 2.1% | 32.71 | +0.39 % ± 2.1% | depth in water no electron |
| OF | 0.5470 | 0.5614 | +2.63 % ± 1% | 0.5483 | +2.1 % ± 1% | 2x2 cm ² 2 cm |
| PVDR | 12.19 | 12.66 | +3.87 % ± 2.1% | 12.47 | +3.67 % ± 2.1% | depth in bone |
| OF | 0.6124 | 0.6172 | +0.8 % ± 1% | 0.6196 | +0.98 % ± 1% | 2x2 cm ² 2 cm |
| PVDR | 13.51 | 13.85 | +2.51 % ± 2.1% | 13.95 | +3.3 % ± 2.1% | depth in bone no electron |

Table 5: Percentage difference between OF and PVDR at 2 cm depth in water and bone with EGSnrc as a gold standard

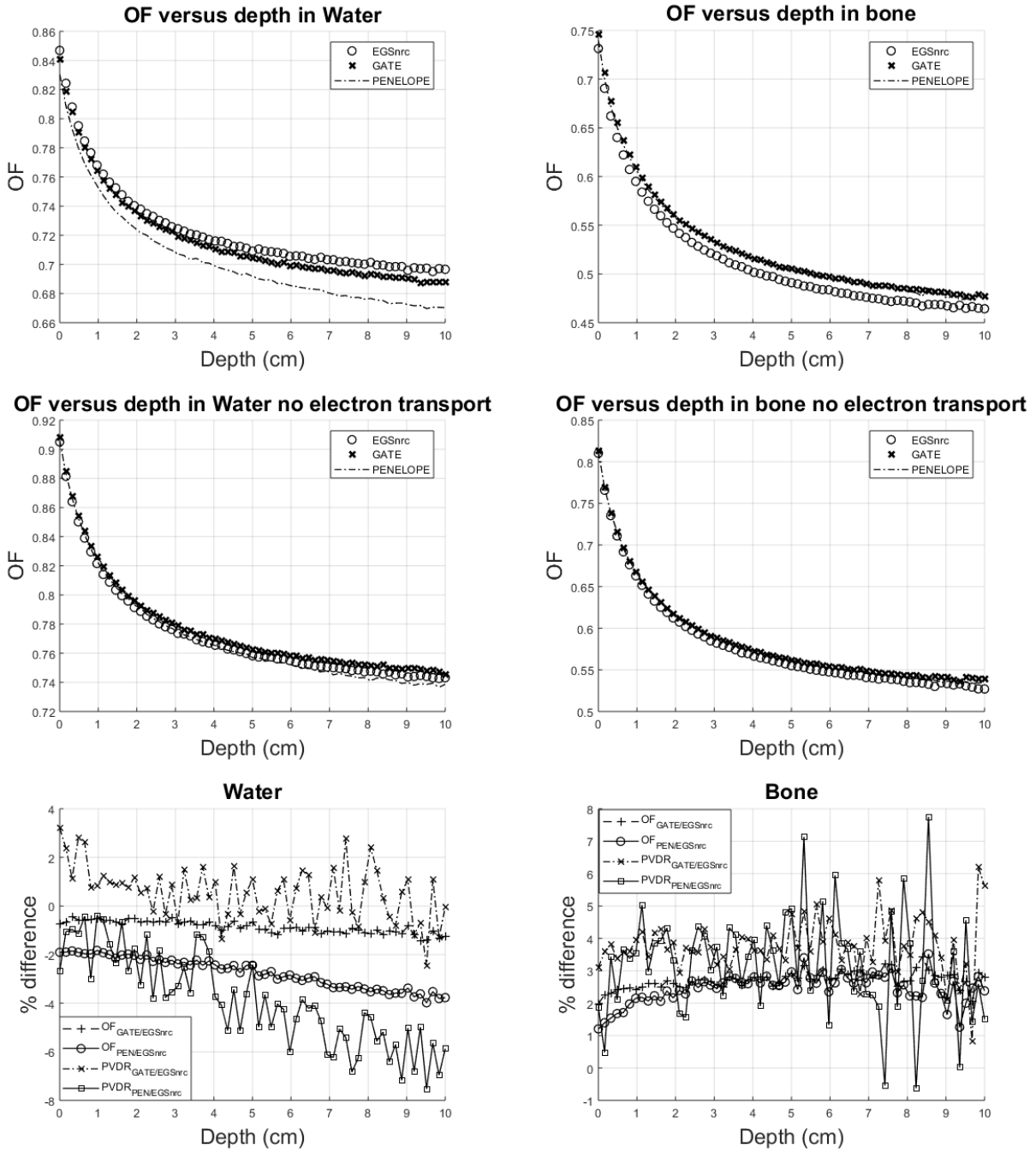


Figure 29: PVDR and OF versus depth for EGSnrc, Geant4 and Penelope

‘ With electron transport switched on:

Figure 30 is the ratio between Penelope and Geant4 dose profile at 2 cm depth with respect to EGSnrc. Scattered dose from GEANT4 is the same as EGSnrc, as the mean of the fluctuations along the whole profile is equal to 0. Penelope, on the other hand,

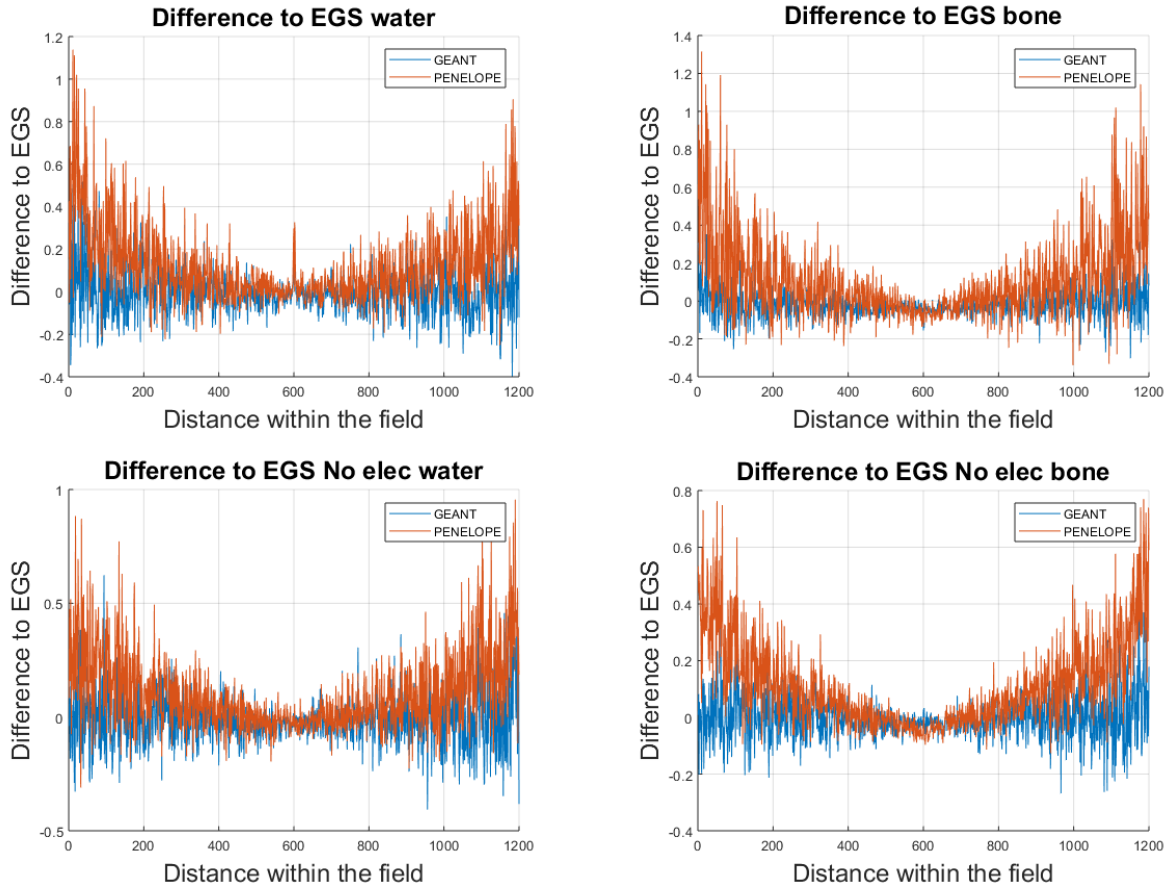


Figure 30: Dose profile at 2 cm depth compared to EGSnrc.

shows an increase in the dose deposition with respect to the lateral distance to the centre of the field. In water, the simulation also highlights a difference in close vicinity to the microbeam for both codes with a 30% increase in the dose deposition in the first pixels (a distance of $25\mu\text{m}$ - $75\mu\text{m}$) around the central pixel for Geant4 and Penelope compared to EGSnrc. In bone, at long distances from the microbeam the difference remains the same for all the codes with a good agreement between Geant4 and EGSnrc and an increase in the scattered dose deposition for Penelope. In this case, the short-range feature disappears.

With electron transport switched off:

In water, the short-range increase in the dose deposition disappears but the long-range discrepancy between Penelope and EGSnrc remains. In bone, at short range, Penelope's relative dose profile falls off rapidly before increasing again with distance.

2.4.3 Discussion

The primary dose in the peak is in agreement for all codes, therefore the main differences in OF and PVDR values come from either the scattered dose deposition or the electron transport. The PVDR simulation is more sensitive to the statistical uncertainties and thus makes the interpretation of the data difficult. The OF, on the other hand, is a more robust tool to analyse the discrepancies as obvious trends can be seen. This is explained by the fact that a lot more measurement points extracted from the 2D profile are used to calculate OF's, then the statistical noise is further reduced according to the Poisson law. EGSnrc and Penelope use analytical Compton profiles and the sampling method from Brusa [67] while the *G4LowEPComptonModel* and its Monash algorithm use the interpolated Compton profile from Biggs [9]. A close agreement between EGSnrc and Penelope is then expected. But surprisingly Geant4 and EGSnrc have the same behaviour in terms of lateral long distance scattered dose deposition. Penelope, on the other hand, highlights an increased lateral dose deposition in comparison to EGSnrc that worsens with the distance to the central peak. The long distance difference suggests a difference in the Compton scattering procedures in Penelope in comparison to EGSnrc and GEANT4. In the vicinity of the central peak, both GEANT4 and Penelope behave the same (Figure 30) with a slower dose fall-off than EGSnrc. This would suggest a difference in the close-range electron transport. Furthermore, the inversion of the behaviour of the close-range difference in bone confirms that electron transport is involved. Two types of electrons are emitted from primary interactions on the path of the microbeam: Compton electrons and photoelectrons. In the hypothesis of a difference of Compton scattering handling, both GEANT4 and Penelope should highlight the same trend away from the central axis but, only Penelope does. Therefore, photoelectrons could be handled in the same way with GEANT4 and Penelope but differently from EGSnrc.

In depth, the agreement between the codes is within the uncertainty bars for the OF from Penelope in water. In bone the agreement is reached for OF in bone without electron transport, otherwise the difference may be up to 3.9%.

The calculation of dosimetric quantities for a $2 \times 2 \text{ cm}^2$ field involves a range of pixels from 400 to 800. Therefore the great difference in the profile above 1 cm is not accounted for when computing OF and PVDR presented in this work. Despite the 30% difference in the dose profile in the ranges 25–75 microns in water (located in 2 pixels), the difference in the OF and PVDR remains lower than 2%. In bone, on the other hand, there is no such large localized difference but the OF and PVDR are not in agreement between the

codes.

2.4.4 Conclusion

Three widely used MC codes have been benchmarked for dosimetry at the micron scale to find-out the cause of discrepancies between experimental and simulated results. Our investigation led to the assessment that the codes agree with each other in water for the PVDR measurement. A discrepancy between Penelope and EGSnrc exists for the OF calculation in water; this discrepancy is attributed to a potential difference in Compton scattering combined with a different way of handling photoelectrons. The difference a long way away from the beam axis is large for Penelope compared to the others but this work is performed to predict experimental measurements of OF and PVDR in reference conditions used in MRT which is limited to $2 \times 2 \text{cm}^2$ field sizes, thus this does not affect the evaluation of OF and PVDR. The codes do not agree in bones, which is not an issue in this work as experimental assessment of dosimetric quantities are performed in a PMMA phantom. Despite the 30% difference in the dose profile in the ranges 25–75 μm in water (20% reported by De Felici [85] between 10–100 microns for 25 μm wide microbeams) the OF and PVDR in water remain correct.

3 Simulation vs Experiment

Three dosimeters that differ in terms of operating mode are compared in MRT reference conditions. The goal of this study is two fold; first to identify sources of discrepancies between the dosimeters, and second to point out elements to explain their relative difference with the MC calculated values.

3.1 Dosimeter Benchmark

3.1.1 Material and Methods

Microbeams profiles are acquired with three different detectors, the PTW microDiamond detector, Gafchromic™ (Ashland Global Holdings Inc, Covington, Kentucky, United States) films and Fluorescent Nuclear Track Detector (FNTD). Gafchromic™ films and FNTD's are passive dosimeters. The information about the dose is recorded in the sensitive material and has to be read out to extract the dose profile after the irradiation. The PTW microDiamond detector, on the other hand, allows an on-line reading.

The FNTD provided by Landauer Inc is based on single crystals of aluminium oxide doped with carbon and magnesium and having aggregate oxygen vacancy defects ($\text{Al}_2\text{O}_3:\text{C,Mg}$). Radiation-induced colour centres in the new material have an absorption band at 620 nm and produce fluorescence at 750 nm with a high quantum yield and a short 75 ± 5 ns fluorescence lifetime. Non-destructive read-out of the detector is performed using a confocal fluorescence microscope. Scanning the three-dimensional spatial distribution of fluorescence intensity along the dose profile permits the extraction of deposited dose in the detector [87].

Gafchromic™ films HD-V2 are designed for use with beams of photons, electrons, protons, ions and neutrons or a large range of doses (10-1000 Gy). They are then suitable for PVDR measurements where the valley dose can be up to 30 times inferior than the peak dose. HD-V2 films are made of two layers, one active 12 μm thick containing the active component, marker dye, stabilizers and other components giving the film its energy independent response and a polyester substrate 96 μm thick. Table 6 shows the HD-V2 films specifications. This detector as well as the PTW microDiamond detector and FNTD's have been developed for CRT applications. Using these kinds of films in MRT is hijacking the prime usage of these films. To a certain extent different results between the dosimeters are then expected.

The irradiation parameters are the following: The dosimeters are placed in a PTW

| Property | Gafchromic™HD-V2 Film |
|--------------------|---|
| Configuration | Active Layer on 97 μm clear polyester substrate |
| Size | 8" * 10" |
| Dynamic dose range | 10 to 1000 Gy |
| Energy dependence | $\leq 5\%$ difference in net density when exposed at 1 MeV and 18 MeV |
| Dose rate response | $\leq 5\%$ difference in net density for 10 Gy exposure at 3.4 Gy/min |

Table 6: HD-V2 films specifications

PMMA tank ($18 \times 18 \times 18 \text{ cm}^3$) at several depths. The tank is irradiated with a $1 \times 1 \text{ cm}^2$, $2 \times 2 \text{ cm}^2$ and $3 \times 3 \text{ cm}^2$ spatially fractionated beam with $50 \mu\text{m}$ microbeams spaced with $400 \mu\text{m}$. Two sets of HD-V2 films are first calibrated in two ways. One calibration curve to assess the valley dose and another for the peak dose. As PVDR's at 2 cm depth in PMMA are expected to be around 30, the peak dose will be extremely high compared to the valley dose. The valley dose can't be as low as possible for this study as it has to be higher than the noise baseline of the films. Information of both films are then combined to extract the PVDR.

FNTD's are acquired from the FNTD 3.0 crystal A377 at Landauer Stillwater Crystal Growth Division. Bleaching of the FNTD's is performed with a Spectra-Physics Explorer 349 nm Laser System to determine the background signal. Wide-field irradiation is performed at the ESRF for dose calibration. A calibration curve is obtained by comparing the fluorescence rate from FNTD's exposed in the Landauer lab and the one exposed at the ESRF.

3.1.2 Results

Table 7 provides the results of the measurements of PVDR with films, microDiamond and FNTD's for field sizes $1 \times 1 \text{ cm}^2$, $2 \times 2 \text{ cm}^2$, $3 \times 3 \text{ cm}^2$ and depths 1cm, 2cm, 4 cm and 8cm. As expected the PVDR from FNTD's measurements are lower than those measured by the microDiamond. The linear attenuation coefficient of aluminium oxide for energies lower than 100 keV is higher than the ones for diamond and films. Then the energy response of FNTD in the valley where the energy spectrum is lower is increased, which leads to a lower PVDR.

On the other hand, the microDiamond could be underestimating the PVDR due to volume averaging effect in the peak dose [88]. Dose gradients are very steep in the peak

| Field Size 1x1 | Films | microDiamond | FNTD | Monte-Carlo |
|-----------------|-------|--------------|-------|-------------|
| Depth 2cm | 30.83 | 36.31 | 36.09 | 51 |
| Field Size 2x2 | | | | |
| Depth 1cm | 22.50 | - | 21.17 | 33 |
| Depth 2cm | 19.52 | 22.23 | 17.58 | 28 |
| Depth 4cm | 17.28 | 19.31 | 15 | 25 |
| Depth 8cm | 15.29 | 17.60 | 17.52 | 22 |
| Field Size 3x3 | | | | |
| Depth 2cm 14.75 | 16.72 | 12.82 | 20 | |

Table 7: PVDR measurement with 3 different dosimeters and comparison with expected MC simulated values.

so a small misalignment of the detector would have deleterious effects on the peak measurement.

The PVDR from the FNTD's are too small because the calibration is performed in a broad beam configuration. The strong energy dependence of the aluminium oxide highlights the need of two calibration curves, one for the peak and another one for the valley just like for films.

3.1.3 Conclusion

Three of the benchmarked dosimeters highlight PVDR's lower than expected. The difference between the measurement themselves is understood by considering the difference in material of the sensitive volumes and knowledge of how the calibration is made.

The discrepancy between MC simulation and measurements may come from the dosimeters behaviour even if the microDiamond highlights a certain sturdiness in measuring doses coming from low-energy X-rays; even if it has been designed for megavoltage X-rays.

As a consequence of this experiment, the assumption is made that the MC calculated PVDR's and OF's does not reflect the reality of the experimental setup, but are from an incomplete MC model. The only way to simulate lower PVDR's is by increasing the scattered radiation, the valley dose will increase and then worsen the PVDR's. The next part of this work is the investigation of potential effects that could add up scattered radiation in the valley region and study their impact on PVDR's and OF's values.

3.2 Study of Potential Total Reflection on Inner Surfaces of the MSC

3.2.1 Motivation and Preliminary study

It has been highlighted by Pauline Fournier [11] that the orientation of the MSC affects both peak and valley doses. In her PhD thesis, she reports a 5.6% decrease in the central peak dose and a 11% increase in the valley dose when the MSC is tilted with an angle of 0.02° . This results in a 15% decrease in PVDR (leading from the ideal MC calculated values 28 to 23.5) and a 5.6% for the OF (from 0.72 to 0.68). Figure 31 shows the increase in the valley dose due to the rotation of the MSC. The first thing to be noted is that valley doses do not follow the MC calculated trend but seem to depend on the MSC geometry. Valley doses on each side of the central peak are different, although expected to be equal. Nevertheless, in this study, the accurate geometry is not accounted for. The emphasis will be on the study of Rayleigh scattering occurring on the MSC inner surfaces, as it is the main built-in effect that could cause an increase in the valley.

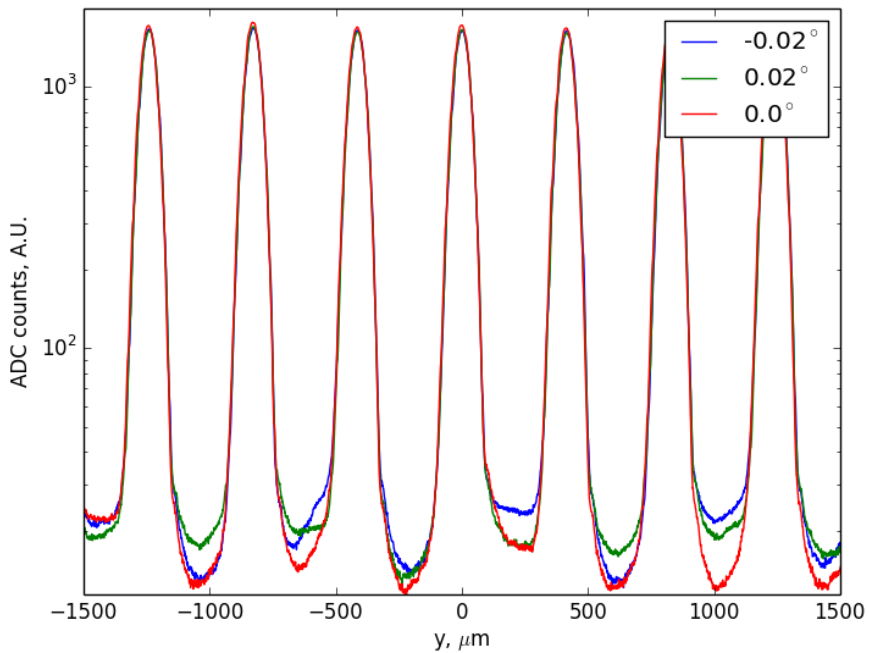


Figure 31: Central microbeams obtained for three different rotation angles of the MSC (-0.02° , 0° and 0.02°) [11].

A preliminary study is performed by the means of MC simulations using a tilted MSC with an angle of 0.02° . The PMMA tank is $18 \times 18 \times 18 \text{ cm}^3$ and placed 110 cm away from the MSC. The ID 17 MRT energy spectrum is used and the linear polarization of the beam is taken into account. The energy fluence is acquired at the entrance of the PMMA tank by the means of a PSF in which a table called `ILB` is stored for each particle. This table contains 5 different values that represent the history of a particle.

- **ILB (1)** is the generation of the particle. `ILB (1)=1` for a primary particle, 2 for secondaries, etc.
- **ILB (2)** is the kind of the parent particle (1 for electrons 2 for photons and 3 for positrons)
- **ILB (3)** is the interaction mechanism that originated the particle
- **ILB (4)** identifies particles from atomic relaxation events
- **ILB (5)** does not represent something in particular but is available for the user to be utilized.

The `ILB (3)` value is of interest here. To isolate Rayleigh photons, the user has to select only these who have the parameter `ILB (3)=1` (The whole nomenclature of interaction mechanisms can be found in the `manual.txt` documentation of Penelope). Figure 32 displays the particles orientation at the entrance of the PMMA tank. The red curve represents photons which underwent a Rayleigh scattering right before entering the PMMA tank. The direction of propagation is asymmetric with respect to the beam axis. This asymmetry is ascribed to Rayleigh scattering occurring on one of the two inner surfaces of the MSC.

Figure 33 shows the photon fluence at the entrance of the PMMA tank. Despite the one side increase in the photon orientation, the photon fluence remains symmetrical.

The same simulation is therefore run again without the PSF. In the present case, the model has to account for the presence of the MSC, as a consequence, the semi-adjoint theorem is not applied, a straightforward calculation is preferred. In comparison to section

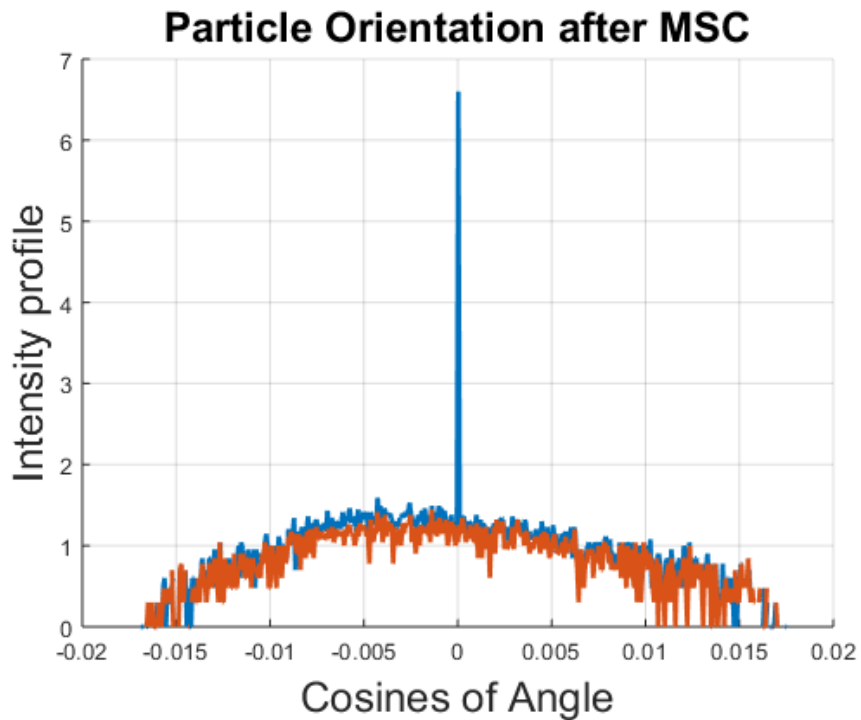


Figure 32: Particle orientation at the entrance of the PMMA tank. The red curve represents photons that underwent a Rayleigh interaction.

1.4.1, the 3D dose box dimensions are adapted to the small dose gradients and described as follows:

| | | | | |
|-------|-----|-----|------|--|
| GRIDX | -1 | 1 | 4001 | [X coords of the box vertices , no. of bins] |
| GRIDY | 100 | 110 | 101 | [Y coords of the box vertices , no. of bins] |
| GRIDZ | -1 | 1 | 39 | [Z coords of the box vertices , no. of bins] |

The photon and electron cut-offs in the PMMA tank are set to 1 keV, and electrons cut-offs are set to 1 MeV (instantly absorbed) in the MSC.

The output of this calculation gives a PVDR and an OF unchanged in comparison to the aligned MSC calculation.

The conclusion of this preliminary study is that a key element in the modelling of the irradiation setup is not accounted for whether it is geometrical or physical. The main goal of this modelling is to investigate the influence of total reflection that might occur on the inner surfaces of the MSC. The small divergence of the beam causes photons

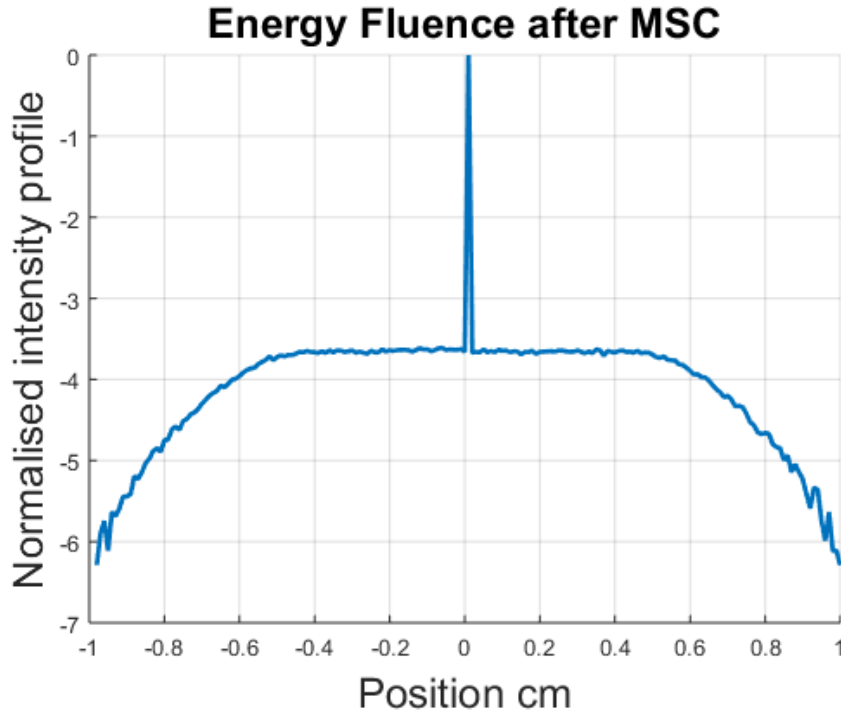


Figure 33: Energy fluence at the entrance of the PMMA dosimetric tank after tilted MSC (natural logarithm scale).

to interact with the MSC's inner surfaces with grazing angles. The hypothesis is made that the deviation of photons directions caused by the total reflection can lead to a dose deposition in the valley and thus worsen PVDR measurements.

3.2.2 Modelling

In this study, the model accounts for the distance between the photon source and the MSC (40 m) the distance MSC/patient (1 m) (Figure 34). At the patient position a screen is placed to record the intensity profile of the beam. Photons are simulated from the source with a normalized intensity. Two different events can occur: photons are transmitted through the matter and their intensity is multiplied according to Beer-Lambert's law, which considers the linear attenuation coefficient of the tungsten carbide at 100 keV (mean energy of the synchrotron beam) or the photons are totally reflected; this changes their direction of propagation but not the intensity. When a reflection occurs, the incident angle between the photon's direction of propagation and the normal vector of the inner surface of the collimator is calculated, a new direction is then generated by changing the sign of the first coordinate of the direction vector.

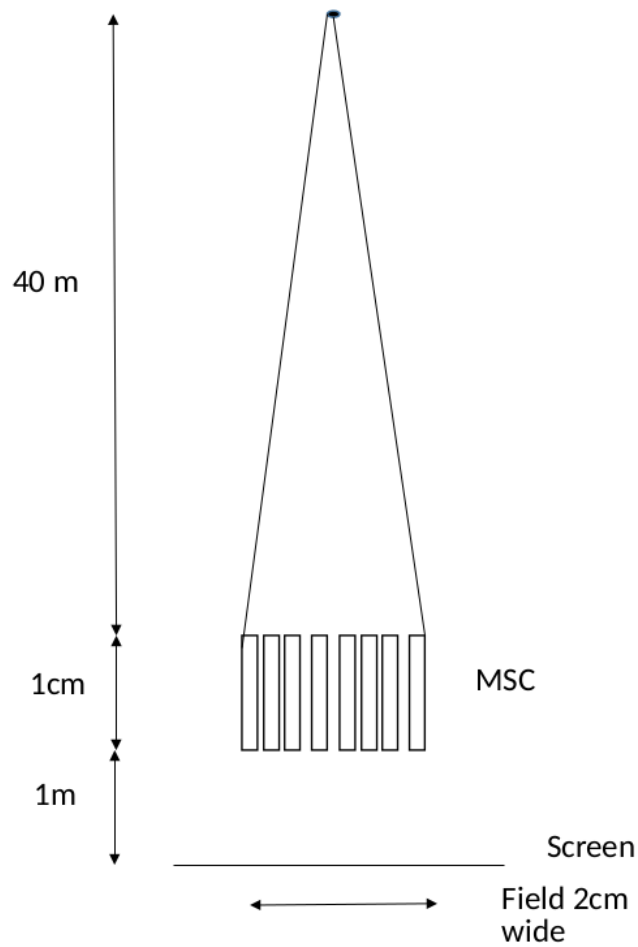


Figure 34: Irradiation geometry used in the python script.

As mentioned, the photons are generated from a point source and carry with them the information of the direction vector. The whole array of photons is then generated by incrementing the first coordinate of the direction vector with the desired quantity. This quantity thus defines the spatial resolution of the calculation.

3.2.3 Geometry

The MSC is built as an array of rectangular boxes of $400 \mu\text{m}$ in width, 1 cm in depth and spaced with $50 \mu\text{m}$ with 4 sides AB BC CD DA (Figure 35). When a photon is

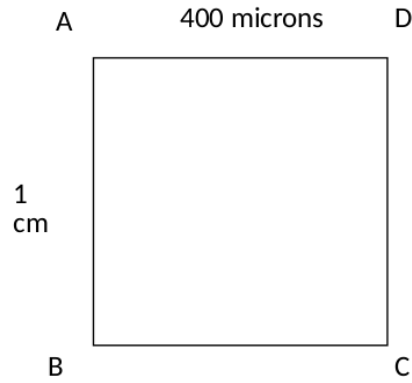


Figure 35: Single box acting as a component of the MSC. Inside the box the material is set as tungsten carbide. Each box is spaced with $50\ \mu\text{m}$ to build up the MSC.

generated, the script tests the intersection of the photon's trajectory with the box. If this intersection is found, the script then tests which side of the box is crossed first. If this segment is AD then there is necessarily another intersected segment. The distance between the entrance and exit point is used to attenuate the beam intensity.

If the first intersected side is AB or DC, the script calculates both scalar and vectorial product between the photon's trajectory and the normal vector of the segment to extract the angle and its sign. The value of the angle is compared to a threshold value. If the angle value is lower than the threshold value, then total reflection occurs. In this case, the intensity of the photons recorded on the screen is arbitrarily fixed at 1.02 for a better readability.

Intersection points are calculated using Cartesian coordinates because this way they are obtained by solving a simple linear system.

3.2.4 Results

The first thing to be noted is that the reflected photons are deviated inside the microbeam itself. The reflection peaks are symmetrical with respect to the beam axis which is a good indication about the proper execution of the script. Considering the position of the screen, reflected photons don't travel far enough to actually deposit their dose in the valley as shown in figure 36. In this simulation, the roughness of the inner surfaces of the MSC is not accounted for, which might be an interesting point to investigate in the future.

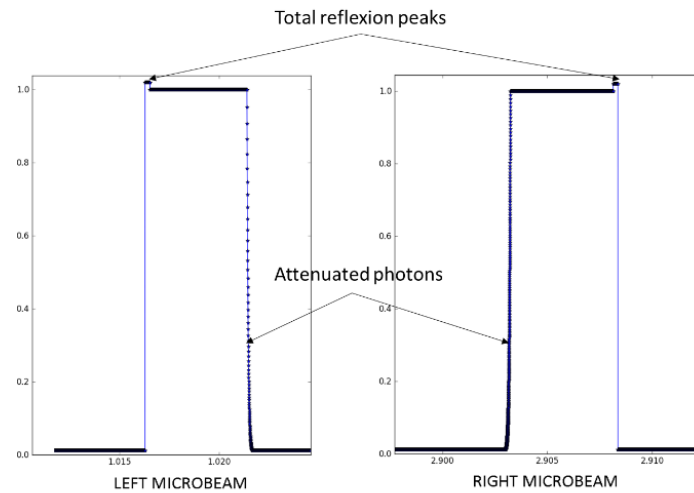


Figure 36: Left and Right microbeam within the field.

3.3 Wobble study

Continuing with the idea of explaining the discrepancies between the MC simulations and the experimental results, attention is brought on a newly discovered phenomenon that occurs during the scan of the sample through the beam. The goniometric table on which the dosimetry cube stands moves up and down to create an irradiation field of the desired size. This motion is expected to be perfectly straight but in reality it wobbles. Figure 37 displays a GafchromicTM film irradiated with a 50 μm wide microbeams 2 cm high with a scan speed of 93 mm/s. An oscillation with varying amplitude is noticeable along the whole height of the beam. The vertical dimension is shrunken to make the wobble more visible.

The measurement of the peak dose with the PTW microDiamond detector is performed at a unique position. The alignment procedure prior to the irradiation is designed to position the sensitive volume of the detector at the centre of the microbeam. A displacement of this maximum - due to the wobble of the goniometric table - causes the measurement position to move to a point where the dose is lower than the central dose and hence worsens the peak dose measurement.

This study is a quantification of the impact of the wobble effect on dosimetric quantities of therapeutic importance in MRT: OF and PVDR at 2 cm depth in a PMMA dosimetric

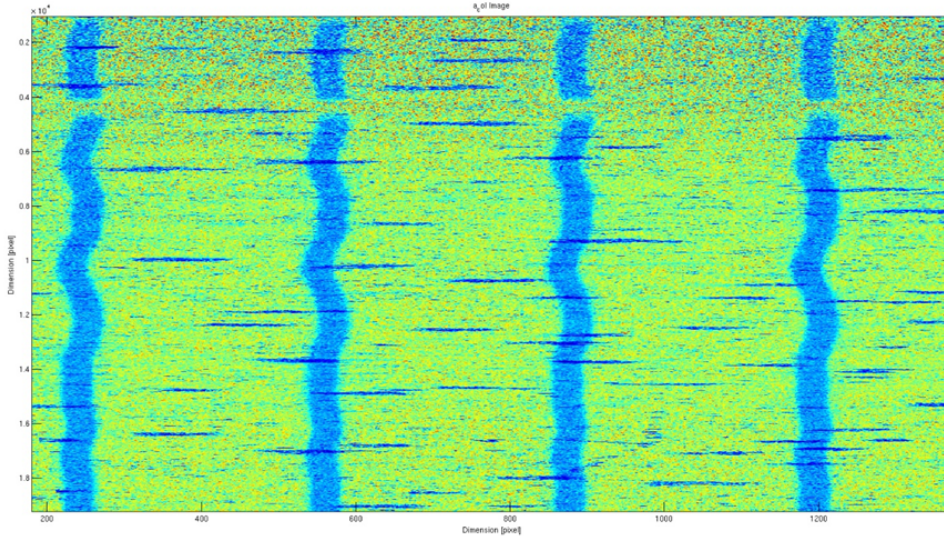


Figure 37: Wobble of the goniometric table noticeable on the Gafchromic film (scan speed 93 mm/s)

cube and a 2×2 cm² field with 50 μ m wide microbeams spaced with 400 μ m.

The examination of the wobble is performed using microbeam measurements acquired on Gafchromic™ films. One single microbeam is isolated and the relevant parameters are extracted. The oscillation is a superimposition of different waves with different frequencies, amplitudes and phases. The accurate characterization of these oscillations is meant to be used as an input photon source model for MC simulations and allows the calculations of the range of uncertainties caused by the wobble. Observations of the wobble at different scan speed show that the shape of microbeams change differently, that is why four different speeds have been chosen for this study 93, 90.6, 46, and 23 mm/s.

3.3.1 Extraction of the Wobble

The characterization of the wobble can be achieved by external measurements of the displacement of the table. The datum acquired this way have to be correlated with the position of the microbeam within the films and require the use of an additional experimental setup. The technique presented here is based on the fact that the whole information about the wobble is already contained on the films, and can be extracted through numerical procedures.

The first step is to remove the noise on the films. Two types of noise are to be distinguished and removed accordingly. The statistical noise that appears like a Gaussian enlargement at the pixel values of interest is removed using a Gaussian filter applied using the built-in

MATLAB[®] (Natick, Massachusetts, US) function called `imgaussfilt()`. The other type of noise is electrical and can be caused by pixels from the camera. This noise known as "pepper and salt" is removed by a median filter using the MATLAB[®] built-in function `medfilt2()`. Finally, a morphological operation called image opening is used to remove from the image any element smaller than a structuring element defined as a square with 2×2 pixels. The results of the procedure are shown in Figure 38 for the film presented in Figure 37 highlighting large white pixel areas, clean enough to extract one single microbeam.

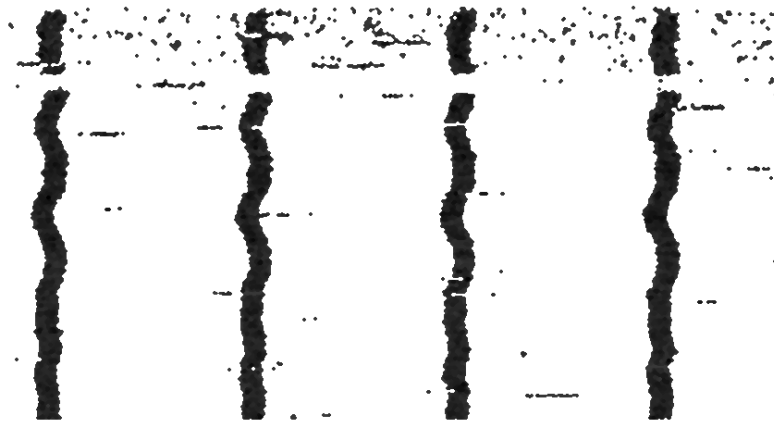


Figure 38: Gafchromic film image cleaned with successive image opening, median filter and Gaussian filter

The cleanest microbeam is extracted -in this case for a 93 mm/s scan speed- the left-hand side microbeam. The profile of the oscillation is retrieved by the means of a loop over all the pixels of the image. Each pixel is tested and the coordinates x and y of the pixels are gathered if they respect the following criteria:

- -The pixel of the previous line and same column has to be white.
- -The pixel of the next line and same column has to be black.

As a result, the blue line displayed on Figure 39 represents the oscillation profile. At this stage, the displacement is expressed in terms of the number of pixels. The pixel size is multiplied by the profile and the mean value is subtracted to centre the oscillation around

0.



Figure 39: Cleanest microbeam isolated with extracted profile

In order to access the frequency information of the profile, a Fast Fourier Transform (FFT) is computed using the `fft()` function from MATLAB[®] defined as follows:

For a length N input vector x , the discrete Fourier transform (DFT) is a length N vector X , with elements:

$$X(k) = \sum_{n=1}^N x(n) e^{-\frac{2i\pi(k-1)(n-1)}{N}} \quad (27)$$

The inverse DFT (computed by `ifft()`) is given by:

$$x(n) = \left(\frac{1}{N}\right) \sum_{k=1}^N X(k) e^{-\frac{2i\pi(k-1)(n-1)}{N}} \quad (28)$$

Extracting the amplitude of the oscillation from the Fourier transform is performed by applying a normalization factor $1/N$ to equation 27. Nevertheless, this factor is removed before computing `ifft()` as the normalization is already accounted for in equation 28. Figure 40 displays the Fourier transform of the 93 mm/s wobble. The frequency of the oscillation is around 25 Hz with the highest amplitude of 11.2 microns. The amplitude of the oscillation is spread between the positive and negative value, as a consequence each peak is half the real amplitude of the displacement.

3.3.2 Wobbling source model for MC simulations

The Fourier transform constitutes the basis of the modelling of the wobbling photon source in MC. Three parameters, amplitude, phase and frequency are gathered from the Fourier transform of the wobble and placed in three arrays. The source model is 50 microns wide, 2cm high and the scan speed dependant oscillation is used to re-sample the lateral position

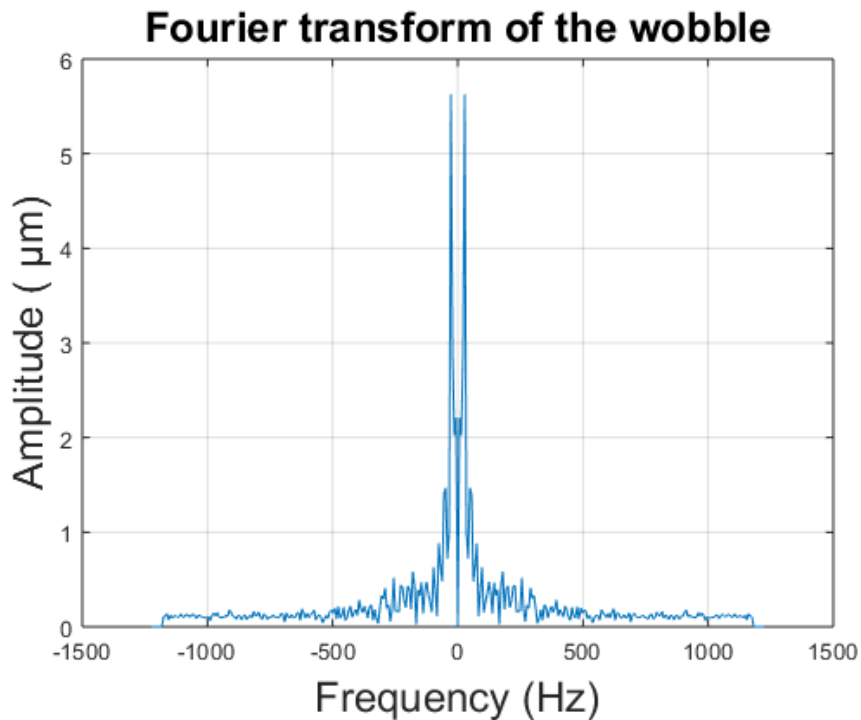


Figure 40: Fourier Transform of the 93 mm/s wobble

of photons from the perfectly straight microbeam. The position, energy and direction of each incoming photon is calculated and written down in a phase space file (PSF) with respect to Penelope's expected syntax.

The first step of the process is the sampling of the MRT energy spectrum. The energy of each initial photon is sampled from the MRT energy spectrum using the inverse transform method described in chapter 1.2.1.a. The cumulative distribution function is called "*cumulFunct*" in the following code:

```
for i=1:1:nbPart
    rng = rand();
    index(i) = max(find(cumulFunct<=rng));
end
```

The maximum value of the cumulative function is 1 and the minimum value is 0. Therefore the use of the function `rand()` with no further transformation is justified. The function `find()` returns an array of the indices of *cumulFunct* that contains values inferior or

equal to *rng*. The function `max()` returns the maximum index in this array, which is the index of the closest value to *rng* present in *cumulFunct*.

The initial photon energy is found using:

$$E(i) = \text{Energy}(\text{index}(i));$$

With `Energy` the abscissa vector of the MRT spectrum. As a result, this procedure generates photons with random energy distributed according to the MRT energy spectrum. To sample the initial position of the particles, the width and height of the beam are stored in variables:

$$\begin{aligned} \text{height} &= 0.0520; \\ \text{width} &= 0.0050; \end{aligned}$$

The positions *X* and *Z* of the straight source are generated with:

$$\begin{aligned} Z &= 2 * \text{rand}() - 1; \\ \text{deltaZ} &= \text{rand}() * \text{height} - \text{height} / 2; \\ Z &= Z + \text{deltaZ}; \\ \text{deltaX} &= \text{rand}() * \text{width} - \text{width} / 2; \end{aligned}$$

The position *Z* is re-sampled in a window 520 μm high to account for the penumbra generated at the edges of the field. The lateral position along the *X* axis is expressed as a function of *Z*. This function is a sum of cosines with amplitudes, frequencies, phases and scan speed previously extracted from the films (*Amp*, *Freq*, *Phase*, *scanSpeed*) expressed as follows:

$$\begin{aligned} \text{sinZ} &= \text{sum}(2 * \text{Amp} * \cos(2 * \text{pi} * Z * \text{Freq} / \text{scanSpeed} + \text{Phase}); \\ X &= \text{sinZ} + \text{deltaX}; \end{aligned}$$

This procedure generates a lateral displacement that ranges from -25 μm and + 25 μm with respect to an oscillating position that depends on *Z*. As a result, Figure 41 displays

for each scan speed tested the microbeam extracted from the film and its corresponding model used as an input for the MC simulation.

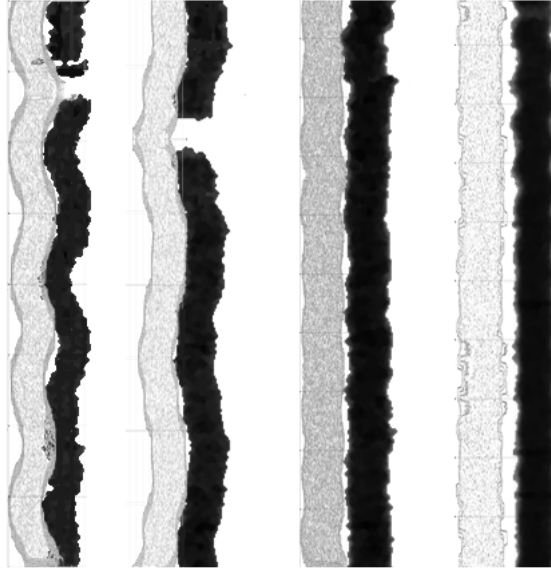


Figure 41: Modelled and measured microbeams for scan speed 93, 90.6, 46, 23 mm/s from left to right.

3.3.3 Impact of the wobble on dosimetric quantities

3.3.3.a Methods

For this simulation, the code MC Penelope is used. The source geometries are contained in four different PSF's corresponding to the four scan speed tested. The microbeams irradiate a PMMA tank $18 \times 18 \times 18 \text{ cm}^3$ placed so as to have 2 cm depth at $Y=0$. The 3D dose distribution is recorded in a 3D dose box with the following dimensions:

| | | |
|-------|-----------|--|
| GRIDX | -1 1 4001 | [X coords of the box vertices , no. of bins] |
| GRIDY | -2 8 101 | [Y coords of the box vertices , no. of bins] |
| GRIDZ | -1 1 39 | [Z coords of the box vertices , no. of bins] |

Each PSF contains the initial state of the $2e10^7$ particles to properly sample the source

area. The particles from the PSF are split into 10 particles when they enter the water tank in order to achieve the desired statistical uncertainty. The cutoffs for photons, electrons and positrons are set to 1 keV and the parameters C1 and C2 are set to 0.01. W_{cc} and W_{cr} have respectively the same values as the photon and electron cutoffs. The step length in the water tank is set to a tenth of 5 μm the smallest dimension of the voxels.

The 3D dose matrix produced as a result is processed with MATLAB[®]. The OF and PVDR are calculated for each slice in the Z direction at 2 cm depth. The central slice and the four adjacent slices are considered for the estimation of the uncertainty range caused by the wobble. 5 voxels correspond to a height of 2.5 mm which is comparable to the 2.1 mm diameter of the microDiamond detector. The percentage difference between the standard deviation of the distribution of OF and PVDR over the 5 slices and the theoretical values for a straight microbeam are given as the uncertainty range.

Each OF and PVDR are given with a statistical uncertainty of 1% for the OF and 2.1% for the PVDR.

3.3.3.b Results

The oscillation of the goniometric table has an influence on the OF and PVDR measurements. The displacement of the maximum of the 50 μm peak causes the measurement of D_{50} to be lower than the expected value without wobble. Figure 53 displays the fluctuations in the PVDR and OF values at 2 cm depths due to the wobble. The amplitude of the fluctuations increases with the scan speed resulting in a mean fluctuation of the PVDR of 2.87% and 1.72% for the OF. For scan speeds below 45 mm/s the fluctuation caused by the wobble is lower than the statistical uncertainties of the calculation for both PVDR and OF. Uncertainties on PVDR's are greater than OF's because of their definitions. Both quantities involve D_{50} the maximum dose of a 50 μm wide microbeam but in the case of OF, this value is contained in one single voxel. For the PVDR calculation, the peak dose is measured within an array of microbeams hence requires to add up contributions from the other microbeams within the field. The further the microbeam, the greater the uncertainty. This results in a increased uncertainty on the PVDR compared to OF.

Fluctuation of OF and PVDR with scanspeed in presence of wobbling

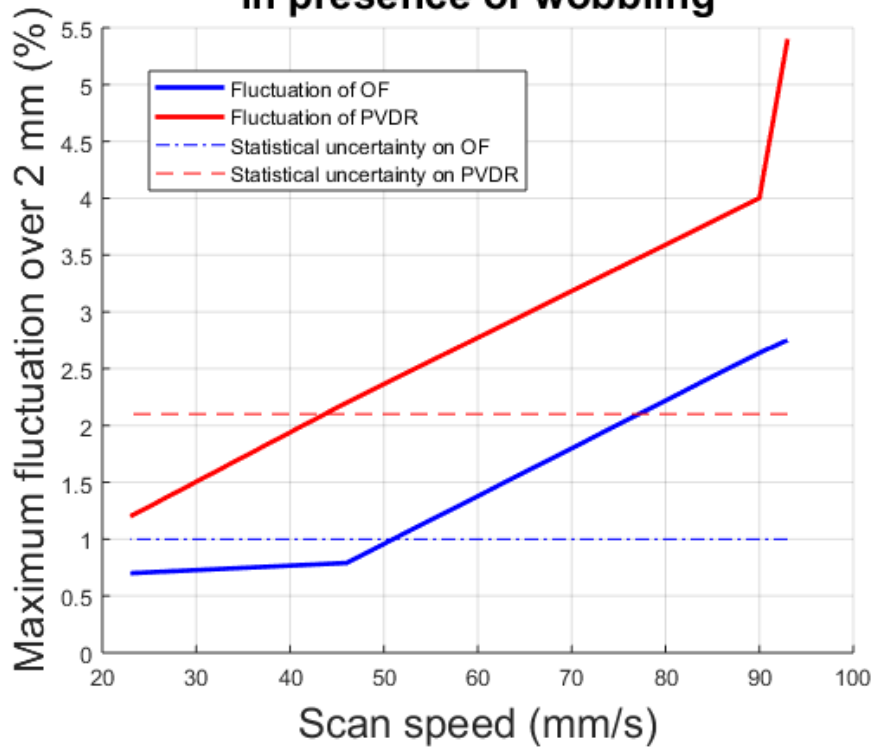


Figure 42: Fluctuation of the measurement of OF and PVDR with scan speed due to the oscillation of the goniometric table.

3.3.4 Conclusion

The impact of the wobble of the goniometric table on OF and PVDR at 2 cm depth has been quantified. The quasi linear dependence of the fluctuation with respect to the scan speed suggests that choosing lower scan speeds for the irradiation would allow more control on the output of the irradiation. Nevertheless, the scan speed depends on the machine current which is not tunable. In the case of a high dose delivery, a slow irradiation works but could be a problem regarding brain motion. A fast irradiation, on the other hand, is preferred as it allows more control on the amount of dose delivered.

It would be useful to identify the source of the wobble to get rid of it, or at least reduce it so that the fluctuation remains below the statistical uncertainty for any scan speed in the relevant range.

4 Application of the Bouchard method on dosimeters

4.1 Bouchard Method

The method described in Bouchard, 2015 [76], is a MC based estimation of correction factors to be applied to measurements for a specific beam quality without requiring any approximation. The characterization of the contribution to the detector dose response is performed by decomposing the overall perturbation factor $P(Q)$ into a product of sub-factors, meant to represent detector-specific physical effects in a given beam quality. The approach of using correction factors is not new [89–93] but the first consistent mathematical approach to this problem was published by Bielajew [94] in which he stated that the product of the sub-factors has to be equal to the overall factor. The method consists in a sequence of $N + 1$ geometries $G_i = G_1, G_2, \dots, G_{N+1}$ each with a single homogeneous scoring volume (i.e., the cavity). Let us consider G_1 to be the fully modelled detector (faithful geometry, materials, including non-sensitive components) in a reference water phantom, G_N the bare detector cavity filled with water, and G_{N+1} a small cavity in water meant to represent the point of measurement in the reference phantom. Let us define the average absorbed doses in G_i as $D_i = D_1, D_2, \dots, D_{N+1}$. The following ratio can be defined:

$$f(Q) = \frac{D_w}{D_{det}} = \left(\frac{\bar{Z}}{A} \right)_m^w P_{MC} P_{vol} \quad (29)$$

In equation 29 the perturbation factor f depends on the beam quality Q . P_{vol} is the perturbation factor due to volume averaging in the cavity and P_{MC} is the perturbation factor of the entire detector defined as follows:

$$P_{MC} = \prod_{i=1}^n P_i \quad (30)$$

where each sub-factor P_i is expressed:

$$P_i = \frac{D_{i+1}}{\left(\frac{\bar{Z}}{A} \right)_{i+1}} \frac{\left(\frac{\bar{Z}}{A} \right)_i}{D_i} \quad (31)$$

with $\left(\frac{\bar{Z}}{A} \right)_i$ taken for the medium constituting the cavity of the geometry G_i . In this formalism, the volume averaging factor P_{vol} is defined separately from the direct Monte Carlo approach. Simulating dose in a volume small enough to represent absorbed dose at a point in water can be highly inefficient. The method as used in this chapter focuses on

the detector characteristics including the shape of its cavity and different materials.

Four key effects can influence the dose measurement compared to water:

- The atomic properties of the detector sensitive volume are not in water, which affects the dose response and perturbs the particle fluence
- The electron density of the detection medium relative to water scales the interaction coefficients and also perturbs the particle fluence
- The presence of non-sensitive components in the detector (walls, electrodes, wires etc.) causes particle interactions to be different from the situation where the detector is a bare cavity
- The finite size of the detector, even made of water causes volume averaging effect

To represent these effects into sub-factors, a set of geometries G_1, G_2, G_3, G_4, G_5 whose differences are reflected by these main characteristics are defined. Two calculations are suggested (paths A and B in Figure 143) with the following geometries:

- (1) the fully modelled detector
- (2) the bare detector volume filled with detector medium, i.e., the detector without its non-sensitive components
- (3) the bare detector volume filled with artificial medium, being either water with the electron density of the detector medium (path A), or the detector medium with the electron density of water (path B)
- (4) the bare detector filled with water
- (5) a volume of water small enough to represent absorbed dose at a point in water

The series of simulation in both cases allows the calculation of the following sub-factors: P_{ext} the extracameral perturbation factor, P_{med} the atomic property correction factor, P_ρ the density correction factor and P_{vol} the volume averaging perturbation factor. Figure 43 displays the two different paths for obtaining the correction factors including the point measurement in water for volume averaging effect correction. This latter effect will not be calculated in this work, but it is expected to be small given the dimensions of the sensitive volume of the microDiamond compared to the microbeam.

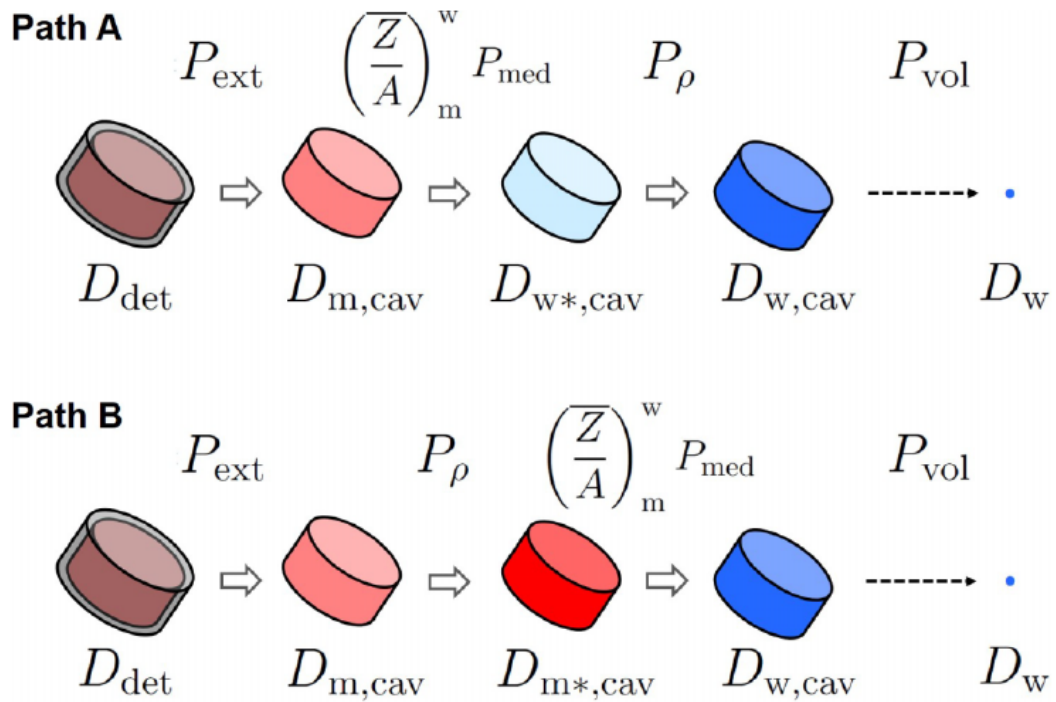


Figure 43: Series of MC simulations to extract perturbation factors.

In this method, one can define the following formalism:

- D_{det} : the absorbed dose in the detector being fully described (proper materials and dimensions) (paths A and B)
- $D_{m,\text{cav}}$: the absorbed dose in the bare detector cavity (paths A and B)
- $D_{w^*,\text{cav}}$: the absorbed dose in the detector cavity filled with water having the electron density of the detection medium (path A)
- $D_{m^*,\text{cav}}$: the absorbed dose in the detector cavity filled with detection medium having the electron density of water (path B)
- $D_{w,\text{cav}}$: the absorbed dose in the cavity filled with water (paths A and B)
- D_w : the absorbed dose to water at the point of measurement

And the sub-factors can be described as follows:

$$P_{ext} = \frac{D_{m,cav} \left(\frac{\bar{Z}}{A}\right)_m}{\left(\frac{\bar{Z}}{A}\right)_m D_{det}} \quad (32)$$

$$P_{med} = \begin{cases} \frac{D_{w^*,cav} \left(\frac{\bar{Z}}{A}\right)_m}{\left(\frac{\bar{Z}}{A}\right)_{w^*} D_{m,cav}} \\ \frac{D_{w,cav} \left(\frac{\bar{Z}}{A}\right)_{m^*}}{\left(\frac{\bar{Z}}{A}\right)_w D_{m^*,cav}} \end{cases} \quad (33)$$

$$P_\rho = \begin{cases} \frac{D_{w,cav} \left(\frac{\bar{Z}}{A}\right)_{w^*}}{\left(\frac{\bar{Z}}{A}\right)_w D_{w^*,cav}} \\ \frac{D_{m^*,cav} \left(\frac{\bar{Z}}{A}\right)_m}{\left(\frac{\bar{Z}}{A}\right)_{m^*} D_{m,cav}} \end{cases} \quad (34)$$

In equations 32, 33 and 34 m , m^* , w and w^* represent respectively the cavity medium, the cavity medium having the electron density of water, regular water, and water having the electron density of the cavity medium.

The overall correction factor P_{MC} is then written:

$$P_{MC} = P_{ext} P_{med} P_\rho \quad (35)$$

In this work, $f(Q)$ is of interest, therefore no intermediate calculation is performed. G_1 and G_4 are used, meaning the fully modelled detector and the water only geometry as allowed by Equation 29. Although interesting, the intermediate steps in the series of calculation are long to calculate. The calculation time is extremely long for each detector, 72 hours for film and FNTD, and 400×72 hours for the PTW microDiamond detector to reach the desired uncertainty.

In this chapter, correction factors are calculated using the Bouchard method for HDV2 films, Landauer FNTD and the PTW microDiamond detector. Finally, all the calculations previously presented are combined together to bridge the gap between MC and experimental results for the PTW microDiamond.

4.2 Bouchard on films and FNTD

4.2.1 Methods

HDV2 Films and FNTD are modelled by the mean of the package PENGEOM. The sensitive volume of films is 12 μm thick on a 97 μm polyester substrate (Figure 44). The active material is made of a mixture with the following mass fractions: hydrogen: 0.0897, carbon:

0.6058, nitrogen: 0.1122, oxygen: 0.1923 with a density of 1.3 g/cm³.

FNTD active thickness is 1.5 mm made of al₂o₃:c,mg with a density of 3.97 g/cm³.

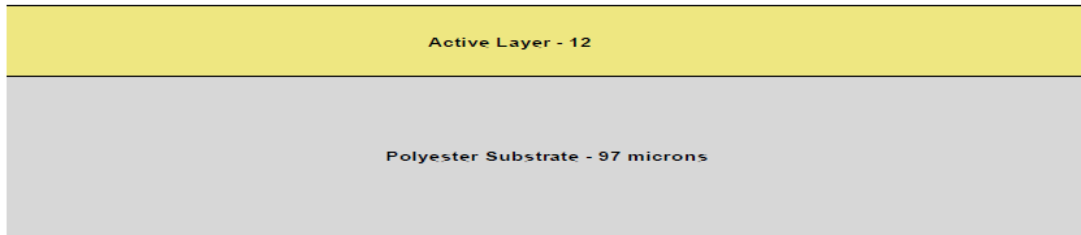


Figure 44: Configuration of the Gafchromic HDV2.

Both films and FNTD are modelled as infinite layers along the x, y plane with their respective thickness in the z direction. A 1.7 cm thick layer of water is placed before the detectors with electron cut-offs set at 100 keV. A second layer of water of 3 mm thickness is placed in between the water layer and the detector with a cut-off set at 1 keV. This layer is copied and also placed after the dosimeters with the same cut-off. The rest of the geometry in depth is then water with 600 keV cut-offs for electrons (electron transport switched off). In every part of the geometry the photon cut-off is set at 1 keV and parameters C_1 and C_2 are set at 0.01. Step length is chosen to be equal to a tenth of the thickness of the considered material layer.

For both detectors, 2 simulations are used:

Simulation 1 Includes the detector with all materials and dimensions

Simulation 2 All materials are replaced with water, simulation parameters remain the same as Simulation 1.

3D-Dose distributions are acquired in dose grids adapted to each sensitive volume thickness.

```
>>>>>>> Dose distribution in a box for HDV2.
GRIDX  -2 2 4001      [X coords of the box vertices , no. of bins]
GRIDY  -1 1 1        [Y coords of the box vertices , no. of bins]
GRIDZ  -0.0012 0 1   [Z coords of the box vertices , no. of bins]
```

```
>>>>>>> Dose distribution in a box for FNTD.
```

```

GRIDX  -2 2 4001      [X coords of the box vertices , no. of bins]
GRIDY  -1 1 1        [Y coords of the box vertices , no. of bins]
GRIDZ  -0.15 0 1     [Z coords of the box vertices , no. of bins]

```

The photon source is a single microbeam 50 μm wide 0.052 cm high and linearly polarized with the ID 17 MRT spectrum.

4.2.2 Results

3D dose boxes from HDV2 FNTD and simulations in water are imported into MATLAB[®] and the profile of the microbeam in the different sensitive volumes are extracted. Dose profiles are presented normalized to the peak dose in water.

4.2.2.a HDV2 films

Figure 45 displays the microbeams in water and HDV2. Absolute peak and scattered doses are lower in HDV2 compared to water, nevertheless this problem is overcome with the calibration of the film prior the measurement.

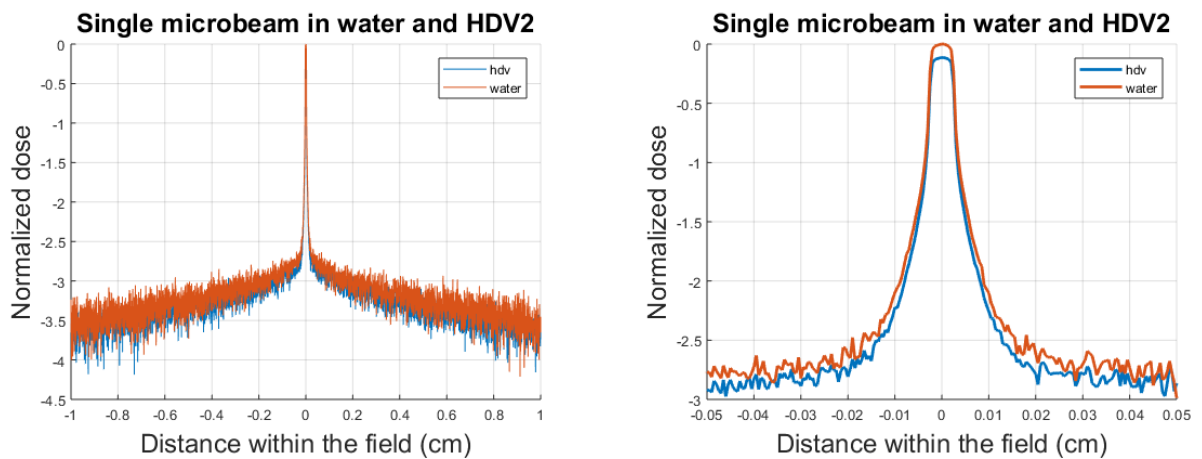


Figure 45: Single microbeam in HDV2 and water at 2 cm depth.

Table 8 presents the PVDR and OF in water and HDV2. The similarity of the values puts forward a water equivalent behaviour of the films.

| | |
|------------|-------------------|
| PVDR HDV2 | 28.01 ± 0.59 |
| PVDR water | 27.60 ± 0.59 |
| OF HDV2 | 0.720 ± 0.008 |
| OF water | 0.719 ± 0.008 |

Table 8: PVDR and OF calculated in HDV2 films and water

| | |
|---------------------------|----------------------------|
| PVDR | Correction factor |
| Peak | 1.30 ± 0.01 |
| Valley | 1.31 ± 0.04 |
| $f(PVDR)$ | 0.988 ± 0.029 (2.97 %) |
| OF | |
| Peak | 1.298 ± 0.009 |
| $2 \times 2 \text{ cm}^2$ | 1.300 ± 0.018 |
| $f(OF)$ | 0.998 ± 0.015 (1.5 %) |

Table 9: Correction factors for absolute dose measurements in HDV2 compared to water.

Table 9 shows the values of the OF and PVDR correction factors obtained as follows:

$$f(OF) = \frac{OF_{water}}{OF_{det}} \quad (36)$$

$$f(PVDR) = \frac{PVDR_{water}}{PVDR_{det}} \quad (37)$$

With $f(OF)$ and $f(PVDR)$ the correction factor of the measurement of the respective quantities with the HDV2 films. As a result, both PVDR and OF correction factors are close to unity, which suggests a similar response of the films to primary and scattered radiation. The correction factor of the peak and valley measurement is the same, 1.3 which confirms the energy independent behaviour in the MRT energy range. The factor 1.3 is also the density of the HDV2 films which scales the interactions within the sensitive volume. This suggests a very low influence of the atomic properties $\left(\frac{Z}{A}\right)_{HDV2}$ in MRT irradiation conditions.

The correction factor for the OF in HDV2 films is also 1.3 in the peak and in the 2×2 cm² field which is consistent with the results from the PVDR.

4.2.2.b FNTD

Figure 46 displays the dose profile in the FNTD sensitive volume and in water. The number of simulated photons is the same as for the HDV2 simulations. Although the profile is less noisy, mainly due to the fact that the sensitive volume in FNTD is 125 times bigger than the active layer of films and FNTD and denser (3.97 g/cm³).

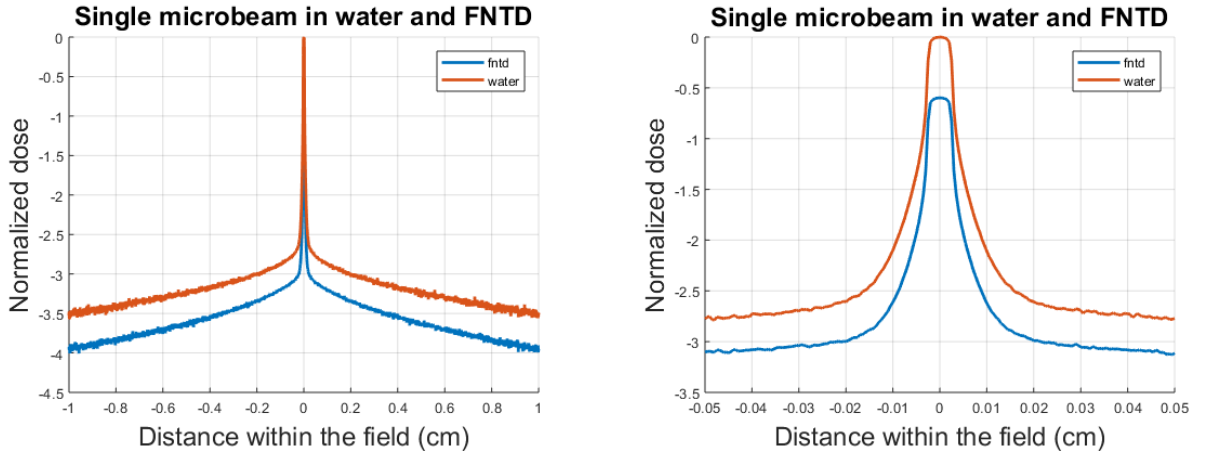


Figure 46: Single microbeam in FNTD and water at 2 cm depth.

Along the lateral profile at 2 cm depth, the dose in the FNTD is lower than the dose in wa-

| | |
|------------|-------------------|
| PVDR FNTD | 16.69 ± 0.35 |
| PVDR water | 27.60 ± 0.59 |
| OF FNTD | 0.627 ± 0.007 |
| OF water | 0.719 ± 0.008 |

Table 10: PVDR and OF calculated in FNTD films and water

| | |
|---------------------------|----------------------------|
| PVDR | Correction factor |
| Peak | 3.88 ± 0.038 |
| Valley | 2.360 ± 0.065 |
| $f(PVDR)$ | 1.640 ± 0.049 (2.97 %) |
| OF | |
| Peak | 3.966 ± 0.028 |
| $2 \times 2 \text{ cm}^2$ | 3.462 ± 0.048 |
| $f(OF)$ | 1.146 ± 0.017 (1.5 %) |

Table 11: Correction factors for absolute dose measurements in FNTD compared to water.

ter. Same as films, the calibration procedure prior to the measurements should overcome this problem but not entirely. As shown in Table 10, the PVDR in the FNTD is 60% lower in the FNTD compared to water and the OF is 14% lower than in water. This can be due to a difference of response of the FNTD between primary and scattered radiation. Table 11 displays the correction factor of peak and valley single point measurements. The peak measurement (peak in an array of microbeams) requires a 3.88 correction factor which is close to the FNTD density but not equal suggesting an influence of the atomic properties $\left(\frac{Z}{A}\right)_{FNTD}$. On the other hand, the correction factor for the peak measurement of the single 50 μm microbeam highlight no dependence on the atomic properties. As expected, the correction of the valley dose measurement is different from the peak with a value of 2.36. in this case, both density and atomic properties influence the dose deposition.

4.2.2.c Conclusion

The study of correction factors on films and FNTD highlights the need to accurately model a dosimeter and to account for the beam quality. Even if films behave the same

in measuring primary and scattered radiation in MRT, this is not the case for FNTD's. One way to make FNTD's reliable in MRT would be to generate several calibration curves based on a peak dose measurement, weighted with the lateral distance to the central peak. Those weights can be extracted from MC simulations such as the ones performed in this chapter.

4.3 Bouchard on PTW microDiamond

Unlike films and FNTD's, the PTW microDiamond detector does not record 2D dose maps but performs point measurements. In order to acquire a full dose profile at 2 cm depth with the same accuracy as the MC simulations presented in the latter sub-chapter, 4001 different simulations should be run, one for each lateral distance. Measuring only half of the peak is not a solution as the asymmetry of the geometry of the microDiamond generates an asymmetry in the dose profile with respect to the central beam.

In addition, recording events far from the beam axis is rare. Attention should be paid to the uncertainty of such value as it will be used combined together with the rest of the measurements to calculate the OF and PVDR and the desired uncertainties. Applying the Bouchard method on any point measurement detector is therefore a delicate task.

4.3.1 Methods

To overcome this problem, the particle splitting method described in section **2.3.5** is used combined with an increased sensitive volume size (from 1 μm thick to 5 μm) which further increases the calculation speed by a factor of 3 (section **2.3.4**). The adapted geometry and cut-offs from section **2.3.1.b** are also used as the resulting enhancement of the calculation speed is a factor 7.

The points chosen to sample the dose profile at 2 cm depths are in the interval [-1 cm, 1 cm] with a spacing of 200 microns (to account for the influence of the 400 μm spaced microbeams and valleys on the central microbeam and central valley respectively). This sampling requires that 200 different simulations are run for the microDiamond detector. The information of the dose in water is mandatory here so another 200 simulations are needed (Equation 29). Preliminary studies aimed at evaluating the simulation time required to achieve the desired uncertainties on OF and PVDR (around 1%) shows 62 hours per simulations are required rounded to 72 hours (3 days). Obtaining the correction factors for OF and PVDR -at 2 cm depths only- takes 1200 days of calculation.

The High Performance Computer Wales (HPCWales) is used to split the simulations over the 400 required processors and therefore reduce the calculation time to 3 days. In practice, 200 processors were allowed to run at the same time and 200 simulations were pending which leads the actual human time to 6 days.

The irradiation geometry is the same as the film and FNTD simulations with the microDiamond geometry placed in the water tank with the centre of the sensitive volume located at 2 cm depth. The dose and uncertainties are gathered from `penmain-res.dat` where energies in eV are stored for each BODY in the geometry. Scoring volume is the same in both detector and water simulations therefore the deposited energy in diamond is normalized by its density (3.51 g/cm^3) to obtain a dose in eV/g.

4.3.2 Results

The dose profile at 2 cm depth as measured by the modelled PTW microDiamond detector is displayed on Figure 47. The peak dose in the diamond is 10 % lower than in water, but the scattered radiation a long way away from the beam axis is the same in both simulations on the left side of the peak (Figure 48) but lower for the microDiamond on the right side. The non-sensitive components have a strong influence on the dose measurement in the position range $[-0.2 \text{ cm}, 0.1 \text{ cm}]$.

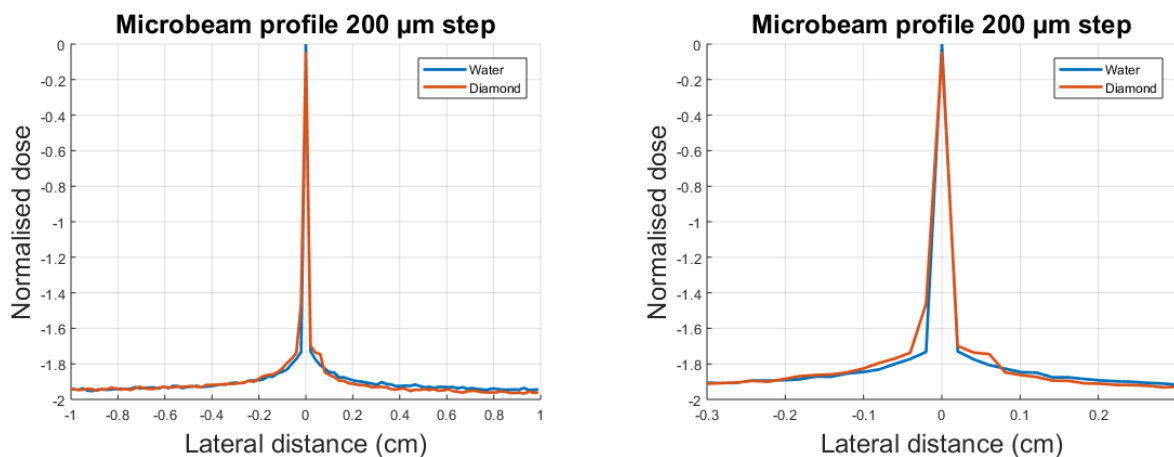


Figure 47: 2cm depth dose profile in water and with the microDiamond.

In the microDiamond geometry, elements above the sensitive volume do not disturb the dose measurement, whether these are resins, aluminium layers or shielding. The difference arises when the beam irradiates either the carbon sensitive volume or the 300 μm thick

substrate. The increase in dose compared to water is linked to the increase in electrons produced in the carbon combined with the reduced range of motion. Electrons supposed to be ejected above the sensitive volume in water are more likely to interact in the carbon thus enhancing the signal. When the beam is irradiating above the substrate, the dose recorded in the sensitive volume of the microDiamond is lower compared to water. This behaviour is ascribed to the carbon substrate that shields the electrons produced further in the stem of the detector.

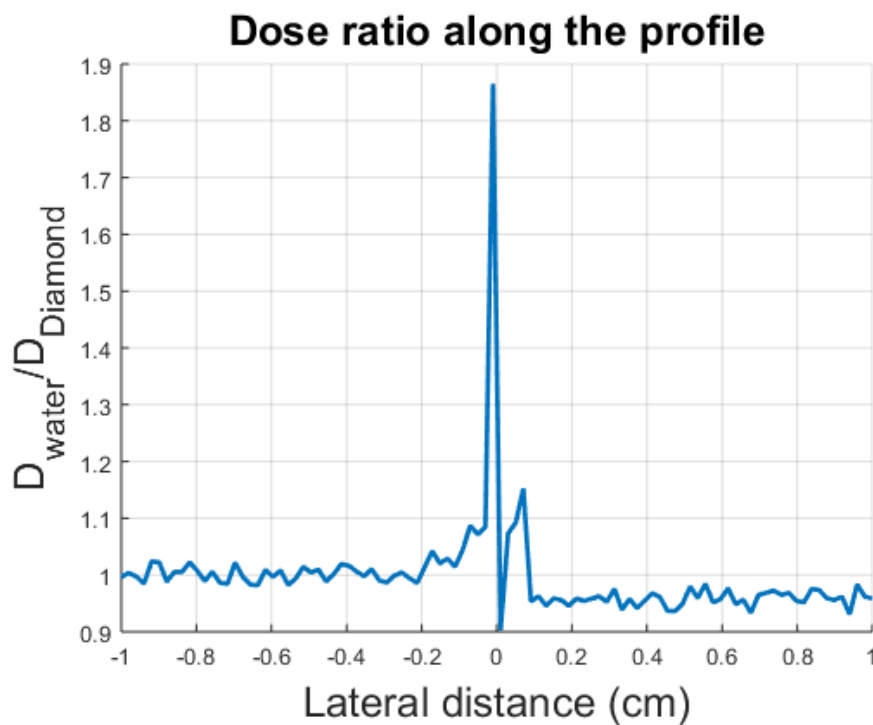


Figure 48: Ratio of doses in water and diamond.

Regarding dosimetry, Table 12 shows the values of OF and PVDR measured in both diamond and water. The microDiamond underresponds when measuring PVDR because of the increase at close distance of the scattered radiation and the underestimation of the peak dose. On the other hand, these effects seems to cancel each other in this irradiation condition for the measurement of the OF.

Correction factors are extracted and confirm the observations previously made. The value of the PVDR in the microDiamond is influenced by both an underestimation of the peak value of 10% and an overestimation of the valley dose by 3.5%. The OF, on the other hand, requires approximately the same correction factor for the peak dose and the

| | |
|-------------------|--------------------|
| PVDR microDiamond | 24.53 ± 0.01 |
| PVDR water | 28.07 ± 0.02 |
| OF microDiamond | 0.7219 ± 0.005 |
| OF water | 0.7284 ± 0.006 |

Table 12: PVDR and OF calculated in microDiamond and water

| | |
|---------------------------|------------------------------|
| PVDR | Correction factor |
| Peak | 1.1032 ± 0.0069 |
| Valley | 0.9642 ± 0.01 |
| $f(PVDR)$ | 1.1442 ± 0.0131 (1.15%) |
| OF | |
| Peak | 1.10 ± 0.006 |
| $2 \times 2 \text{ cm}^2$ | 1.0977 ± 0.01 |
| $f(OF)$ | 1.0089 ± 0.0102 (1.06 %) |

Table 13: Correction factors for absolute dose measurements in microDiamond compared to water.

maximum dose in the $2 \times 2 \text{ cm}^2$ field.

4.3.3 Conclusion

The calculation of correction factors for OF and PVDR with the PTW microDiamond at 2 cm depths in MRT highlight 3 different behaviours: When the sensitive volume is irradiated by a direct flux of primary photons the detector seems to under-respond, compared to a regime dominated by scattered electrons where it over-responds at short range due to a shorter mean free path of the electrons, and finally a one sided under-response at large distances due to a shielding of the electrons by the carbons substrate. The measured PVDR at 2 cm depth in water for $50 \mu\text{m}$ wide microbeams spaced with $400 \mu\text{m}$ should therefore be multiplied by 1.144 and the OF by 1.0089: Using the experimental values presented in section 3.1.2 (PVDR = 22.23 OF= 0.68) the corrected PVDR and OF are respectively 25.18 and 0.686.

4.4 Bridging the gap between MC and experiments

So far, the influence of the wobble of the goniometric table on PVDR and OF has been quantified and the correction factors accounting for the PTW microDiamond's intrinsic characteristics were calculated, but for convenience microbeams have been simulated as one parallel photon beam added up to create the full irradiation field. Although convenient, this method does not account for the beam divergence passing through the entire MSC collimator. As a matter of fact, the further from the beam axis the greater the incidence angle of the primary photons on the inner surfaces of the MSC. The influence of the air gap between the MSC and the phantom has been ignored and will be quantified in this section along side the influence of the beam divergence and MSC presence which will be presented as one global correction factor. In addition, when the microDiamond is utilized experimentally, the dose is acquired by scanning the detector through the beam. The centre of the sensitive volume is at the centre of the field at rest. When the scan starts, at the upper and lower position, half of the detector's sensitive volume is out of the field (Figure 49) thus integrating a dose which is not accounted for in any other simulation of this work.

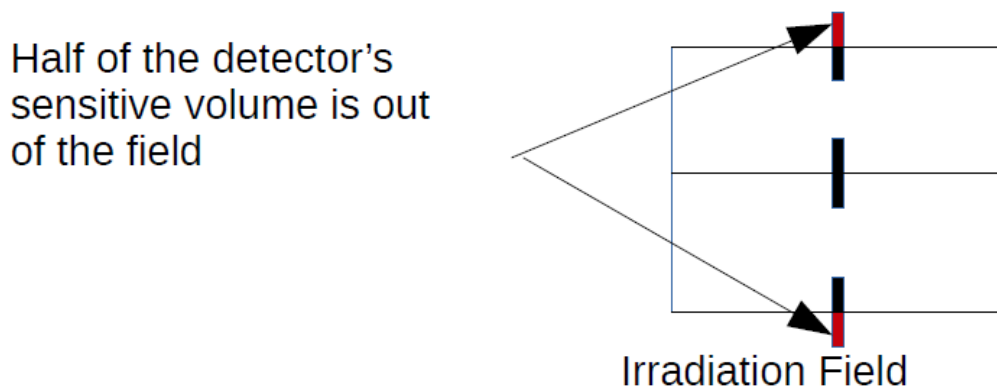


Figure 49: microDiamond sensitive volume at the edges of the irradiation field.

4.4.1 Methods

The geometry of the ID 17 MRT hutch has been coded by Martínez-Rovira *et al.* [12] in 2011 in a format readable by PENELOPE. In this study, the authors modelled the photons

source from the wiggler up to the patient position. A dedicated program called SHADOW generated the synchrotron radiation from the wiggler up to the entrance of the MRT hutch and photon positions and energies were stored in a PSF. This PSF used as an input source in PENELOPE was used to propagate the photons in the MRT hutch. Figure 50 displays the diagram of the elements inserted on the path of primary photons that are present in the geometry file. We gathered from the authors this input geometry file and used it to extract dosimetric quantities in close to real conditions.

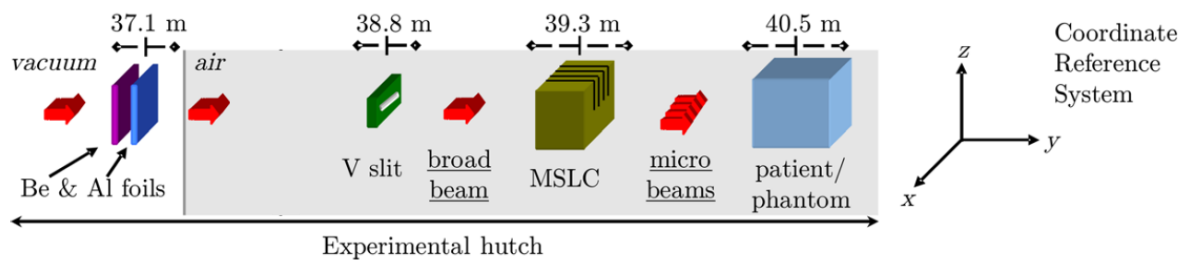


Figure 50: Geometry of the experimental hutch adapted from Martínez-Rovira and al [12].

When entering the hutch, photons pass through successive layers of materials starting with Beryllium and aluminium foils, air, then the vertical slit that defines the beam height, the MSC, a last air gap and finally the water phantom.

The source is located 40 metres upstream the phantom and defined as a point source emitting a rectangular beam using the following declaration:

```
SPOSIT 0.0 -4058 0.0 [Coordinates of the source]
SBOX 0.0 0.0 0.0
SRECTA 90.0007 89.9993 90.014 89.9860
```

In the MSC the electron cut-offs is set to 600 keV to disregard their evolution as electrons generated in the MSC cannot reach the phantom. In air, electrons have 1 keV cut-offs as they can influence the entrance dose. Electron cut-off is also set to 1 keV in the water tank. 3D-Dose distribution is acquired in the following dose grid.

>>>>>>> Dose distribution in a box for HDV2.

| | | | | |
|-------|------|-----|------|--|
| GRIDX | -1 | 1 | 4001 | [X coords of the box vertices , no. of bins] |
| GRIDY | 165 | 169 | 25 | [Y coords of the box vertices , no. of bins] |
| GRIDZ | -1.1 | 1.1 | 43 | [Z coords of the box vertices , no. of bins] |

The grid along the Z axis is slightly larger than in the other cases, to account for the integration effect of the detector. In this case, the dose is integrated over 2.2 cm instead of 2 cm. The geometry file is used for 2 different calculations, one for the OF and the other one for the PVDR as the main difference between them is the width of the incoming beam. In the case of the OF, the beam is 51 μm wide and centred on the central slit of the MSC, for the PVDR, the beam is 2 cm wide and irradiating 48 slits. Preliminary calculations to evaluate the time needed to reach the desired uncertainty of 1 % highlight a total calculation time of more than 1700 days (600 for the OF 1100 for the PVDR). One reason for this is that uncertainties at large distances from the beam axis are big. When the statistical uncertainty of the central peak dose is 4.5% the uncertainty of the valley dose is 50 %. Reducing the error on scattered dose is the challenge of these calculations. The other reason is the presence of large distances over several metres. Many histories will be generated and won't produce any relevant signal in the 3D dose box, and the particles that pass through may undergo multiple interactions before reaching the phantom. The geometry file provided by Martínez-Rovira does not include regions in the different bodies to adapt the cut-offs like in section **2.3.1.b**. One major drawback with geometry definition in PENELOPE is that an existing geometry file is difficult to modify, this is why we use it as it is.

To overcome this problem, the homemade parallel PENELOPE described in section **2.3.3** is used over 200 processors for 72 hours for OF and 2 times 72 hours for the PVDR. When a 3 days run finishes, results from all the processors are gathered to produce a global 'dump' file that records the current state of the simulation. Manually, the calculation is restarted using the global dump file as new starting point.

4.4.2 Results

As a result, the contribution of the presence of the different inserted devices such as the MSC, the air and taking into account the beam divergence and the integration effect lowers both OF and PVDR at a 2 cm depth. The OF is lowered by 2.3 % and the PVDR by 4.75%. This difference can be explained by the fact that for the OF calculation, the beam is limited in width, therefore remains close to the ideal calculation despite the

| Condition | OF | PVDR | $\frac{\Delta OF}{OF_{ref}}$ | $\frac{\Delta PVDR}{PVDR_{ref}}$ | $\frac{\delta OF}{OF}$ | $\frac{\delta PVDR}{PVDR}$ |
|----------------|--------------------|-------------------|------------------------------|----------------------------------|------------------------|----------------------------|
| Reference (MC) | 0.7285 ± 0.008 | 28.59 ± 0.60 | | | 1.1% | 2.1% |
| Integration | 0.7284 ± 0.02 | 28.44 ± 1.08 | ↵ 1.8% | 3.8% | 2.56% | 3.8% |
| AIR+MSC+div | 0.7153 ± 0.01 | 27.35 ± 0.74 | ↵ 2.3% | 4.75% | 1.8% | 2.7% |
| Wobble | 0.6985 ± 0.01 | 26.001 ± 0.62 | ↵ 1.72% | 2.87% | 1.45% | 2.39% |
| Bouchard | 0.6860 ± 0.07 | 25.18 ± 0.28 | ↵ 0.89% | 14.46% | 1.06% | 1.15% |
| Experimental | 0.68 | 22.23 | | | | |

Table 14: Summarize of all the different effect quantified in this work and the associated magnitudes.

presence of air and the MSC. In the case of the PVDR, parts of the MSC in between the slits are irradiated as well, as some of the photons can thus pass through and generate and increase in the valley which does not exist in the ideal simulation. Unfortunately, this simulation does not allow the differentiation of the effect of the MSC and the beam divergence, it gives however a global influence of the whole system on dose profiles at 2 cm depth.

The integration over 2.2 cm influence both OF and PVDR in different ways. The OF is lowered by 1.8% and the PVDR by 3.8%. Table 16 summarizes the magnitudes of the influences of inserted devices, wobble and the Bouchard method with respect to the ideal MC simulation. The different contributions are added up together from the experimental results obtained with the microDiamond. If the effect accounts for X% on the OF_i , the resulting OF_{i+1} is $OF_i + OF_i \frac{X}{100}$. This way, the experimental values are successively corrected for the quantified effects of this study.

As a result, combining the accurate geometry of the experimental hutch, accounting for the wobble of the goniometric table and considering the intrinsic characteristics of the microDiamond through the Bouchard method allow the correction of experimental

measurement that lead to an OF of 0.7284 ± 0.02 and a PVDR of 28.44 ± 1.08 . The agreement is within the error bars for the OF and the PVDR with respective uncertainties of 2.56% and 3.8%. The main source of uncertainty is from the wobble study, but the number of particles in the PSF is limited. Despite the splitting, the PSF has a latent uncertainty that is unknown to the user if a dedicated study is not performed [95]. This means that this unknown uncertainty is a limit that cannot be exceeded even with a large splitting.

5 Conclusion

The use of small fields in radiotherapy techniques has increased substantially, in particular in stereotactic treatments and large uniform or nonuniform fields that are composed of small fields such as for intensity modulated radiation therapy (IMRT) or Microbeam Radiation Therapy. For these irradiation fields, dosimetric errors have increased compared to conventional beams. The main reason for this is that no standard dosimetric protocol exists. In the case of MRT, a dedicated protocol has been developed based on a broad beam measurement with a PinPoint chamber combined with the multiplication with an OF to predict the peak dose. This protocol is handy in the sense that it allows to overcome the lack of spatial resolution of the detector and to move forward with pre-clinical procedures for enabling the calculation of the peak dose. The valley dose is then retrieved using the PVDR also based on MC calculations.

Over the last decade, detectors with high spatial resolution allowing measurements at the micron scale became available. Among them, the PTW microDiamond detector, HDV2 films combined with the appropriate read-out system and FNTD have been examined in this research. Measurements performed at the ID 17 biomedical beamline with these three dosimeters highlighted discrepancies between the MC simulated values of OF and PVDR and experimental data which addresses an issue regarding the validity of the current dosimetry protocol. Moreover, it has been highlighted that OF and PVDR values differ between the different MC codes which represents a problem when associated with the dosimetry protocol. Obtaining reliable values of OF and PVDR for both experimental and numerical measurement represents the principle challenge of this study.

The first output of this thesis is the benchmark of the MC codes EGSnrc, Geant4 and PENELOPE. This study highlights a maximum of 2% in difference in the OF value in water between EGSnrc and PENELOPE. This difference is due to a difference in the way scattered radiation is handled in PENELOPE as the dose a long way away from the beam axis is increased compared to EGSnrc and Geant4. A located short range increase in the dose deposition at 2 cm depth for PENELOPE is to be noted as well and suggests a difference in the way the photoelectric effect is handled.

A piece of the answer to this problem is addressed in "A Survey of Photon Cross Section

Data for use in EPICS2017” by Dermott.E Cullen published in February 2018 [96]. In PENELOPE, the ”normalization screening correction” [97] is applied at low energy cross-sections. This has for consequence to lower the photoelectric cross section and increase the Compton cross-section which explains the increase in scatter radiation in the case of PENELOPE. But the presence of the re-normalization is under debate between Jim Scofield, Paul Bergstrom and Francesc Salvat in private communications with Dermott Cullen. Salvat claims that the measurements at low energy are too rare to conclude on the absence of re-normalization. The theory allows its use, and it therefore remains in the code PENELOPE. The discussion about including the re-normalization at low energies leads to the emergence of the need for accurate cross-section measurements. An idea to lead this study forward is to use the MRT technique as a high accuracy measuring tool instead of a radiotherapy treatment modality. The modelled MRT irradiation conditions lead the different MC codes to disagree with each other, it is therefore a reasonable assumption to consider a similar behaviour in real conditions. There is a need for an answer in this range of energies and using the MRT for this wider application would be beneficial to both the MRT project and the radiation transport communities.

MC simulations are a representation of the reality that is often not free of errors. The use of simplifications regarding the geometry, or beam characteristics are performed to usually reduce the calculation time and the real-time required for the modelling. In some cases, a simpler model is used because the more complicated aspects are unknown. This is the case of the wobble of the goniometric table that was revealed by Paolo Pelicioli using HDV2 films. The amplitude of the motion requires a spatial resolution at the micron scale to be noticeable and a 2D mapping of the dose to characterize the wobble which HDV2 can provide. As a consequence, the wobble plays a role in the dose measurement of 1.72% in the OF measurement and 2.87% for the PVDR. The quantification of the impact of the wobble is a long process that involves numerous different steps for the extraction of the information about the oscillation, and the creation of input files for the MC calculation. The most comfortable scenario for the future of the dosimetry protocol would be to get rid of the wobble as its impact on dosimetric quantities depends on the scan speed. If the wobble remains, Figure 53 can be used to estimate the uncertainty on the OF and PVDR measurements at 2 cm depth in the range of the tested scan speeds.

The use of alternative geometries to capitalize on symmetries of the system to decrease the calculation time was used very often in this thesis. Nevertheless, these techniques represent an approximation that is quantified in this work. The beam divergence, the presence of the MSC and the air between before the patient, among with the presence of beryllium windows and aluminium foils have an impact on dosimetric quantities. The calculation in such large geometries is very long which justifies the use of the semi-adjoint theorem. But the error made using such approximation is up to 4.75 % for the PVDR and 2.3% for the OF at 2 cm depth. Working on the geometry file provided by Martínez-Rovira by adding sub-volumes with chosen cut-offs would be a great added value to increase to efficiency of the calculation. Importance sampling can be added to the code `penmain` itself to simulate relevant events and disregard those that will not contribute to the result. As an example, a primary photon that interacts with the MSC and is deviated out of the limits of the 3D dose box could be killed. Important particles could, on the contrary, be split.

The detector benchmark involving the microDiamond detector, HDV2 films and FNTD reveals a difference in PVDR measurements. The simple comparison of the result does not give any information about where the difference comes from. In order to point out the reasons of such differences, the detector characteristics have to be accounted for. The Bouchard method is an elegant way to access this information. As a result, this method allows the calculation of correction factors for each dosimeters and to quantify the response to an irradiation. The FNTD shows a difference in the response between the peak and the valley due mainly due to atomic properties. HDV2 films on the other hand, behave the same in both peak and valley. Applying the Bouchard method on HDV2 and FNTD is straightforward and can be executed with one single processor in a reasonable amount of time. The microDiamond detector realizes point measurements, therefore the application of the Bouchard method is more difficult. As a result, the microDiamond highlights three different behaviours depending on the irradiation conditions, first a very good response to scattered radiation if primary photons are irradiated above the carbon substrate, secondly an under-response of 10% when primary photons irradiate the sensitive volume and finally an under-response of approximately 3% for primary photons irradiated below the carbon substrate. These result show an influence of the non-sensitive components of the detector

when used in MRT irradiation conditions.

Present work realized by Paolo Pelicioli with HDV2 films shows that attention should be paid on the way films are used when combined with a PMMA tank. Films are taped on slabs of PMMA and inserted in the tank at the desired depth. It was demonstrated that the roughness of the films and the PMMA slabs creates air gaps of a few tenth of microns. These air gaps create a fluctuation in the OF and PVDR measurements.

The challenge of this PhD was to bridge the gap between MC simulations and experimental measurements. The identification and the quantification of the different processes involved allow it. Calculations remain very long but are mandatory to accurately account for all these effects. Similar calculations should be performed on any dosimeter used in MRT.

6 Scientific production

Oral presentations in international conferences

D. Reynard, R.P. Hugtenburg, I. Al-Affan, F.Estève, E. Braueur-Krish. Monte Carlo intercomparison of EGSnrc, Geant4 and Penelope for MRT . *Monte Carlo Neutron, Hadron, Electron and Gamma radiation transport codes* , January 2018, Surrey, UK

D. Reynard, R.P. Hugtenburg, I. Al-Affan, F.Estève, E. Braueur-Krish. Accurate dosimetry for microbeam radiation therapy. *ABMU PhD students workshop*, December 2017, Swansea, UK

D. Reynard, R.P. Hugtenburg, I. Al-Affan, F.Estève, E. Braueur-Krish. Accurate dosimetry for MRT. *Monte Carlo Neutron, Hadron, Electron and Gamma radiation transport codes* , Decembre 2016, Manchester, UK

D. Reynard, H. Elleaume, T. Brochard, J.F. Adam. In vivo dosimetry for synchrotron stereotactic radiation therapy. *8th Medical Applications of Synchrotron Radiation conference*, 5-8 october 2015, Villard de Lans, France

M. Ruat, J.F. Adam, C. Nemoz, **D. Reynard**, P. Deman, T. Brochard, C. Ponchut. Synchrotron Radiation Computed Tomography with combined high spatial and temporal resolutions. *8th Medical Applications of Synchrotron Radiation conference*, 5-8 october 2015, Villard de Lans, France

Poster presentations

D. Reynard, R.P. Hugtenburg, I. Al-Affan, F.Estève, E. Braueur-Krish. Accurate dosimetry for microbeam radiation therapy. *Journée de l'EDISCE*, Juillet 2017, Grenoble, France

Articles in peer-reviewed international journals

D. Reynard, R.P. Hugtenburg, François Estève, J.F. Adam. Towards in vivo dosimetry for contrast enhanced synchrotron stereotactic radiation therapy based on iodine x-ray spectroscopy. *Biomedical Physics & Engineering Express* 4 (4), 2018

7 Résumé du travail de thèse en français

7.1 Contexte du projet de thèse

Ce travail est centré sur le développement d'une dosimétrie précise en MRT au moyen d'un détecteur microDiamond développé par PTW et de simulations Monte-Carlo (MC). Le détecteur PTW microDiamond a un volume sensible cylindrique de $0,004 \text{ mm}^3$, avec un rayon de $1,1 \text{ mm}$ et une épaisseur de $1 \text{ }\mu\text{m}$. Ce détecteur présente l'avantage d'être presque équivalent aux tissus biologiques et sa géométrie permet des mesures à haute résolution. La résolution la plus élevée est obtenue lorsque la plus grande dimension du volume sensible du détecteur est parallèle à la direction du faisceau (mode 'edge-on') [45], et, en outre, cette configuration réduit l'effet de moyennage dû au volume [46]. En utilisant le détecteur de cette façon, nous pouvons mesurer la dose déposée à l'intérieur du microfaisceau (dose pic) et à l'extérieur (vallée) à une résolution micrométrique et calculer le rapport de dose pic à vallée (PVDR).

Le PVDR est une valeur relative, par conséquent, ne devient important que lorsque les valeurs de dose sont converties du plan de traitement pour calculer la dose absolue dans la vallée pour le tissu normal, ce qui correspond à la valeur de dose maximale admissible par rapport au NTCP [44]. Des protocoles de dosimétrie absolue ont été proposés pour les faisceaux synchrotron utilisant des chambres d'ionisation (CI) pour les mesures de débit de dose en faisceau large [47]. Actuellement, la détermination de la dose absolue à l'ESRF pour les champs MRT est effectuée pour des champs de $2 \times 2 \text{ cm}^2$ en utilisant des mesures de débit de dose en faisceaux larges avec une chambre d'ionisation PinPoint [48].

Ce protocole de dosimétrie est limité pour les faisceaux synchrotron spatialement fractionnés, car la chambre d'ionisation PinPoint ne répond pas aux exigences d'une dosimétrie appropriée en termes de résolution spatiale. Néanmoins, les profils de dose relative en profondeur peuvent être déterminés à l'aide de plusieurs types de détecteurs, chacun avec leurs propres avantages et inconvénients. Les résultats les plus prometteurs jusqu'à présent ont été obtenus avec des films Gafchromic, soit en combinaison avec un microdensitomètre ou un microscope. Les films fournissent des informations importantes sur les gradients de dose et la distribution 2D, mais la résolution du densitomètre limite la précision spatiale. De plus, l'acquisition est très bruitée et les films ne peuvent pas être lus en temps réel. D'autres dosimètres potentiels à haute résolution sont de bons candidats pour la dosimétrie des MRT, parmi eux les fluorescent nuclear track detector (FNFD) de Landauer (détecteurs Al_2O_3) et les dosimètres à thermoluminescence 2D (TLD), tous

deux incapables d'effectuer une mesure de dose en temps réel et nécessitant une forte calibration.

7.1.1 Challenges

Dans n'importe quel type de dosimétrie, pas spécialement en MRT, la mesure du dépôt de dose absolue dans un milieu, même homogène, reste une tâche délicate. Ceci est dû à quatre effets clés décrits par Bouchard et al. [49] qui se produisent dès que l'on place un détecteur dans un milieu. (i) Les propriétés atomiques du volume sensible du détecteur peuvent être différentes de celles de l'eau, ce qui affecte la réponse à la dose et perturbe la fluence des particules (ii) la densité électronique du milieu de détection par rapport celle de l'eau est différente donc perturbe également la fluence des particules (iii) la présence de composants non sensibles dans le détecteur (y compris les parois, électrodes, fils) fait que les interactions des particules sont différentes de la situation où le détecteur est une cavité nue (iv) la taille finie du détecteur, même fait d'eau, provoque un effet de moyenne volumique. Ces quatre effets clés doivent être corrigés pour chaque qualité de faisceau. Par qualité du faisceau, on entend ici l'ensemble des conditions d'irradiation qui dépend du spectre du faisceau, de la géométrie du fantôme, de la position de mesure et de la présence de gradients latéraux de dose .

En MRT, le spectre de photons et d'électrons varie entre le pic et la vallée, et l'obtention de profils de dose est obtenue en balayant le détecteur à travers le faisceau, un ensemble complet de facteurs de correction doit être appliqué pour chaque point de mesure. Nos mesures de profils de dose avec le microDiamond PTW démontrent également l'influence non négligeable des composants non sensibles, car le profil du pic est asymétrique et reflète la géométrie du détecteur (Figure 51). Cet aspect sera discuté plus tard dans ce travail.

L'ensemble des facteurs de correction proposés par Bouchard et al. pour chaque qualité de faisceau peut être déterminé analytiquement en utilisant l'intégrale de cavité Spencer-Attix-Nahum [51] pour les détecteurs à gaz ou la théorie de Burlin [52] pour les détecteurs à semi-conducteurs. Mais ces deux approches s'appuient sur la connaissance de la fluence des photons et des électrons dans l'eau et du détecteur pour chaque qualité de faisceau. En dosimétrie de petit champ, le principal défi consiste à déterminer la fluence des électrons en fonction de la qualité. A l'origine, le calcul a été effectué analytiquement pour les faisceaux de référence en supposant un équilibre des particules de chargées (CPE) qui permet d'estimer les facteurs de perturbation. Cependant, dans les petits champs, ces

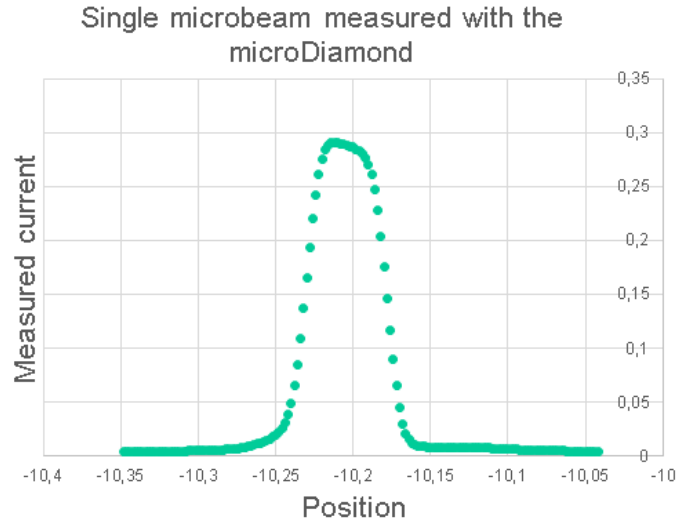


Figure 51: Single microbeam measured with the PTW microDiamond detector. The asymmetry in the lateral dose gradient and the inclined top are the due to the non-sensitive components in the detector.

approches ne conviennent pas et nous devons nous fier aux simulations MC [49]. Notre capacité à corriger correctement la mesure de dose par rapport à la qualité du faisceau dépend fortement de notre aptitude à modéliser avec précision les conditions d'irradiation et la géométrie du détecteur. Pour ce faire, la source de rayons X ID 17 a été modélisée avec le code de traçage synchrotron SHADOW. Les photons du wiggler ont été simulés avec le code MC PENELOPE/PENEASY à travers un fichier de géométrie contenant toute la structure de la ligne de lumière jusqu'à un plan vertical en amont de la position du patient [12].

Les distributions de dose dans des milieux homogènes ont été vérifiées expérimentalement à l'aide de films gafchromic dans un fantôme d'eau solide pour les gradients de dose latéraux et les courbes de dose en profondeur pour un faisceau large. Les PVDR ont également été simulés et comparés aux mesures gafchromic et étaient en accord. Malgré le fait que les données expérimentales actuelles ne reproduisent pas les valeurs de PVDR prédites par Rovira et al. avec les films Gafchromic et le PTW microDiamond. De plus, certaines caractéristiques du profil de microfaisceaux combinées à notre incapacité à mesurer expérimentalement le PVDR nous amènent à supposer que le MC n'est pas complet.

7.1.2 Présentation du microDiamond

Le détecteur PTW microDiamond est un détecteur monocristallin synthétique développé pour la dosimétrie des petits champs. Le procédé utilisé pour la fabrication est le dépôt chimique en phase vapeur d'une structure multicouche de diamant de type p hautement conducteur/diamant intrinsèque sur un substrat de diamant monocristallin à haute pression et haute température (HPHT) tel que décrit par Almaviva, et al. [53].

Semblable aux diodes de silicium, ce détecteur à diode Schottky ne nécessite aucune polarité appliquée pour collecter les charges. Son volume sensible est un cylindre de 2,2 mm de diamètre et de 1 μm d'épaisseur. Le volume actif du diamant est dominé par un mince contact circulaire en aluminium d'un diamètre de 2,2 mm qui a été déposé en phase vapeur sur la surface du substrat de diamant.

| | |
|--------------------------|--|
| Detector type | Synthetic single crystal diamond detector |
| Dimensions | Diameter 7 mm, length 45.5 mm |
| Nominal sensitive volume | 0.004 mm ³ , radius 1.1 mm, thickness 1 μm |
| Detector Bias | 0 V |
| Energy Response | $\leq \pm 8 \%$ (100 keV- ⁶⁰ Co) |

Table 15: PTW microDiamond detector specificities.



Figure 52: Radiographie à haute résolution de la structure interne du microDiamond. [8].

Le tableau 15 énumère les principales caractéristiques du détecteur PTW microDiamond.

Le paramètre clé pour atteindre la microdosimétrie est son volume sensible de 1 μm d'épaisseur. Figure 52 affiche la structure interne du microDiamond. Le volume sensible est situé à l'extrême droite de la structure prise dans la pince métallique. Marinelli *et al.* [54] a étudié la surface sensible moyenne et l'épaisseur sensible sur 10 détecteurs de microdiamants PTW. Afin d'évaluer le volume actif du microDiamond, l'épaisseur de la couche de détection du diamant a été évaluée indépendamment par des mesures de capacité et des expériences de détection de particules alpha. Un diamètre moyen de surface active de $2,19 \pm 0,02$ mm a été mesuré. Les épaisseurs moyennes de volume actif de $1,01 \pm 0,13$ μm et $0,97 \pm 0,14$ μm ont été dérivées par des mesures de capacité et de sensibilité, respectivement. Les résultats obtenus sont en accord avec les valeurs nominales indiquées dans les spécifications du dosimètre du fabricant. Une réponse homogène a également été observée sur l'ensemble de la zone active de l'appareil.

Livingstone *et al.* [8] a caractérisé le détecteur de microdiamants PTW pour les champs fractionnés spatialement à l'IMBL (Imaging and Medical Beamline) au synchrotron australien et a rapporté une dépendance énergétique dans la gamme d'énergie 30-120 keV avec un facteur K_Q de $1,05 \pm 0,09$. De plus, l'indépendance du débit de dose de 1 à 700 Gy/s a également été mise en évidence. Le détecteur microDiamond semble convenir à la dosimétrie en MRT en raison de sa faible dépendance à l'égard du débit de dose. Le fabricant annonce une faible dépendance énergétique et angulaire dans une gamme d'énergie de 100 keV à 1,25 MeV et des angles de 0 à 40 degrés.

7.2 Présentation des principaux résultats

7.2.1 Comparaison des principaux codes MC utilisés en MRT

Trois codes MC largement utilisés ont été comparés pour la dosimétrie à l'échelle du micron afin de déterminer la cause des écarts entre les résultats expérimentaux et les résultats simulés. Notre enquête a mené à la conclusion que les codes s'accordent les uns avec les autres dans l'eau pour la mesure du PVDR. Il existe un écart entre PENELOPE et EGSnrc pour le calcul de l'OF dans l'eau que les auteurs attribuent à une différence potentielle de diffusion Compton combinée à une façon différente de manipuler les photoélectrons. Cette différence loin de l'axe du faisceau est importante pour PENELOPE par rapport aux autres, mais ce travail est effectué pour prédire les mesures expérimentales d'OF et de PVDR dans les conditions de référence utilisées en MRT qui est limité à $2 \times 2 \text{cm}^2$, donc

cela n'affecte pas l'évaluation des OF et PVDR. Les codes ne concordent pas dans l'os, ce qui n'est pas un problème dans ce travail, car l'évaluation expérimentale des quantités dosimétriques est effectuée dans un fantôme PMMA. Malgré la différence de 30% dans le profil de dose dans les plages 25-75 μm dans l'eau (20% rapporté par De Felici [85] entre 10-100 microns pour 25 μm microbeams larges), l'OF et le PVDR dans l'eau restent corrects.

7.2.2 Influence de l'oscillation de la table goniométrique sur la dosimétrie

L'oscillation de la table goniométrique a une influence sur les mesures OF et PVDR. Le déplacement du maximum du pic de 50 μm diminue la mesure de D_{50} par rapport à la valeur attendue sans oscillation. La figure 53 affiche les fluctuations des valeurs PVDR et OF à des profondeurs de 2 cm dues à l'oscillation. L'amplitude des fluctuations augmente avec la vitesse de balayage, ce qui entraîne une fluctuation moyenne du PVDR de 2,87 % et de 1,72 % pour l'OF. Pour des vitesses de balayage inférieures à 45 mm/s, la fluctuation causée par l'oscillation est inférieure aux incertitudes statistiques du calcul pour le PVDR et l'OF. Les incertitudes sur les PVDR sont plus grandes que celles des OF en raison de leurs définitions. Les deux quantités impliquent D_{50} la dose maximale d'un microfaisceau de 50 μm de largeur, mais dans le cas de l'OF, cette valeur est contenue dans un seul voxel. Pour le calcul du PVDR, la dose maximale est mesurée à l'intérieur d'un réseau de microfaisceaux; il faut donc additionner les contributions des autres microfaisceaux dans le champ. Plus le microfaisceau est éloigné, plus l'incertitude est grande. Il en résulte une incertitude accrue sur le PVDR par rapport à l'OF.

L'impact de l'oscillation de la table goniométrique sur l'OF et le PVDR à 2 cm de profondeur a été quantifié. La dépendance quasi linéaire de la fluctuation par rapport à la vitesse de balayage suggère que le choix de vitesses de balayage plus faibles pour l'irradiation permettrait de mieux contrôler la délivrance de l'irradiation. Néanmoins, la vitesse de balayage dépend du courant de la machine qui n'est pas accordable. Dans le cas de l'administration d'une forte dose, une irradiation lente fonctionne, mais pourrait poser un problème de mouvement du cerveau. Par contre, une irradiation rapide est préférable, car elle permet un meilleur contrôle de la quantité de dose délivrée. Il serait utile d'identifier la source de l'oscillation pour s'en débarrasser, ou du moins la réduire de manière à ce que la fluctuation reste inférieure à l'incertitude statistique pour toute vitesse de balayage dans la plage pertinente.

Fluctuation of OF and PVDR with scanspeed in presence of wobbling

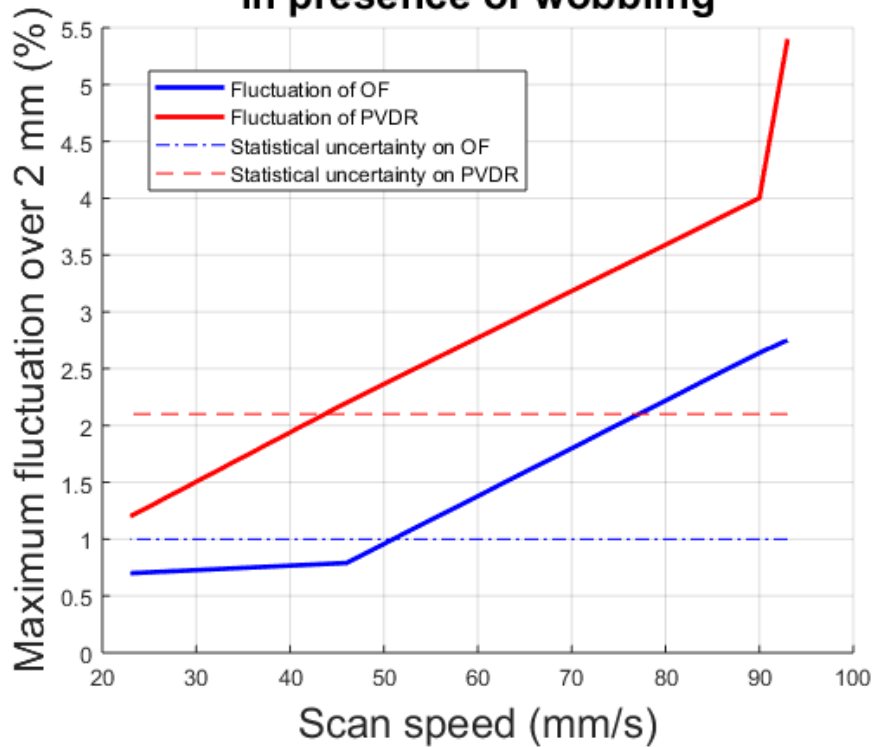


Figure 53: Fluctuation de la mesure de l'OF et du PVDR avec la vitesse de balayage due à l'oscillation de la table goniométrique. Fluctuation of the measurement of OF and PVDR with scan speed due to the oscillation of the goniometric table.

7.2.3 Quantification de l'influence du détecteur et des éléments sur le trajet du faisceau sur la dosimétrie

La contribution de la présence des différents dispositifs insérés tels que le MSC, l'air et la prise en compte de la divergence du faisceau et de l'effet d'intégration abaisse à la fois l'OF et le PVDR à 2 cm de profondeur. L'OF est abaissé de 2,3 % et le PVDR de 4,75 %. Cette différence s'explique par le fait que pour le calcul de l'OF, le faisceau est limité en largeur, donc reste proche du calcul idéal malgré la présence d'air et du MSC. Dans le cas du PVDR, des parties du MSC entre les fentes sont également irradiées là où certains photons peuvent passer à travers et générer une augmentation de dose dans la vallée, ce qui n'existe pas dans la simulation idéale. Malheureusement, cette simulation ne permet pas de différencier l'effet du MSC et la divergence du faisceau, mais a une influence globale sur l'ensemble du système. L'intégration sur 2,2 cm influence OF et PVDR de différentes manières. L'OF est abaissé de 1,8% et le PVDR de 3,8%. Le

| Condition | OF | PVDR | $\frac{\Delta OF}{OF_{ref}}$ | $\frac{\Delta PVDR}{PVDR_{ref}}$ | $\frac{\delta OF}{OF}$ | $\frac{\delta PVDR}{PVDR}$ |
|----------------|--------------------|-------------------|------------------------------|----------------------------------|------------------------|----------------------------|
| Reference (MC) | 0.7285 ± 0.008 | 28.59 ± 0.60 | | | 1.1 % | 2.1 % |
| Integration | $0,728 4 \pm 0,02$ | $28,44 \pm 1,08$ | \hookleftarrow 1,8% | 3,8% | 2,56% | 3,8% |
| AIR+MSC+div | $0.7153 \pm 0,01$ | $27,35 \pm 0,74$ | \hookleftarrow 2,3% | 4,75% | 1,8% | 2,7% |
| Wobble | 0.6985 ± 0.01 | $26,001 \pm 0.62$ | \hookleftarrow 1.72 % | 2.87 % | 1.45 % | 2.39 % |
| Bouchard | $0.6860 \pm 0,07$ | $25,18 \pm 0,28$ | \hookleftarrow 0,89% | 14,46% | 1,06% | 1,15% |
| Experimental | 0,68 | 22,23 | | | | |

Table 16: Résumé de tous les différents effets quantifiés dans ce travail et les grandeurs associées.

tableau 16 résume les amplitudes des influences des dispositifs insérés, de l'oscillation de la table goniométrique et de la méthode de Bouchard par rapport à la simulation MC idéale. Les différentes contributions sont additionnées à partir des résultats expérimentaux obtenus avec le microDiamond. Si un effet compte pour X% sur OF_i , OF_{i+1} résultant est $OF_i + OF_i \frac{X}{100}$. De cette façon, les valeurs expérimentales sont successivement corrigées des effets quantifiés de cette étude.

La combinaison de la géométrie précise de la hutch expérimentale, la prise en compte de l'oscillation de la table goniométrique et la prise en compte des caractéristiques intrinsèques du microDiamond par la méthode de Bouchard permettent de corriger les mesures expérimentales qui conduisent à un OF de $0,728 4 \pm 0,02$ et un PVDR de $28,44 \pm 1,08$. L'accord se situe à l'intérieur des barres d'erreur pour l'OF et le PVDR avec des incertitudes respectives de 2,56% et 3,8%. La principale source d'incertitude est l'étude des oscillations, mais le nombre de particules dans les fichier d'espace des phases (PSF) est limité. Le PSF présente une incertitude latente qui est inconnue de l'utilisateur si une étude spécifique n'est pas réalisée [95]. Cela signifie que cette incertitude inconnue est

une limite qui ne peut pas être améliorée sans ajouter de particules dans le PSF.

7.3 Conclusion

L'utilisation de petits champs dans les techniques de radiothérapie a considérablement augmenté, en particulier dans les traitements stéréotaxiques et les grands champs uniformes ou non uniformes qui sont composés de petits champs tels que la radiothérapie à modulation d'intensité (IMRT) ou la radiothérapie par microfaisceaux. Pour ces champs d'irradiation, les erreurs dosimétriques ont augmenté par rapport aux faisceaux conventionnels. La raison principale en est qu'il n'existe pas de protocole dosimétrique standard. Dans le cas de la MRT, un protocole dédié a été développé sur la base d'une mesure de faisceau large avec une chambre d'ionisation PinPoint combinée à la multiplication avec un OF pour prédire la dose dans le pic. Ce protocole est pratique en ce sens qu'il permet de surmonter le manque de résolution spatiale du détecteur et de toute façon d'aller de l'avant avec les procédures pré-cliniques en permettant le calcul de la dose pic. La dose dans la vallée est ensuite récupérée à l'aide du PVDR, également basé sur des calculs MC.

Au cours de la dernière décennie, des détecteurs à haute résolution spatiale permettant des mesures à l'échelle du micron sont devenus disponibles. Parmi eux, le détecteur de microdiamants PTW, les films HDV2 combinés avec le système de lecture approprié et le FNTD. Les mesures effectuées sur la ligne de lumière biomédical ID 17 avec ces trois dosimètres ont mis en évidence des divergences entre les valeurs simulées MC de OF et PVDR et les données expérimentales qui traitent d'un problème concernant la validité du protocole de dosimétrie actuel. En outre, il a été souligné que les valeurs OF et PVDR diffèrent entre les différents codes MC, ce qui représente un problème lorsque ces valeurs sont associées au protocole de dosimétrie. Obtenir des valeurs fiables d'OF et de PVDR pour les mesures expérimentales et numériques représente le défi de ce travail.

Le premier résultat de cette thèse est la comparaison des codes MC EGSnrc, Geant4 et PENELOPE. Cette étude met en évidence une différence maximale de 2% dans la valeur de l'OF dans l'eau entre EGSnrc et PENELOPE. Cette différence est due à une différence dans la façon dont le rayonnement dispersé est traité dans le code PENELOPE car la dose loin de l'axe du faisceau est augmentée par rapport EGSnrc et à Geant4. Une augmentation localisée à courte distance de l'axe du faisceau à une profondeur de 2 cm pour le code PENELOPE doit également être notée et suggère une différence dans la

façon dont l'effet photoélectrique est traité. Une partie de la réponse à ce problème est abordée dans "A Survey of Photon Cross Section Data for the use in EPICS2017" par Dermott.E Cullen publié en février 2018 [96]. Dans PENELOPE, la "normalisation de la correction d'écrantage" [97] est appliquée aux sections efficaces de faible énergie. Ceci a pour conséquence d'abaisser la section efficace photoélectrique et d'augmenter la section efficace Compton, ce qui explique l'augmentation du rayonnement diffusé dans le cas de PENELOPE. Mais la présence de la renormalisation fait l'objet d'un débat entre Jim Scofield, Paul Bergstrom et Francesc Salvat dans des communications privées avec Dermott Cullen. Salvat affirme que les mesures à faible énergie sont trop rares pour conclure sur l'absence de renormalisation. La théorie permet son utilisation, donc reste dans le code PENELOPE. La discussion sur l'inclusion de la re-normalisation aux basses énergies conduit à l'émergence du besoin de mesures précises. Une idée pour faire avancer cette étude est d'utiliser la MRT comme outil de mesure de haute précision au lieu d'une modalité de traitement de radiothérapie. Les conditions d'irradiation de MRT modélisées amènent les différents codes MC à être en désaccord les uns avec les autres, il est donc raisonnable de considérer un comportement similaire dans des conditions réelles. Il y a besoin d'une réponse dans cette gamme d'énergies et l'utilisation de la MRT pour une application plus large serait bénéfique à la fois pour le projet MRT et pour les utilisateurs de MC en transport de radiation.

Les simulations MC sont une représentation de la réalité souvent non exempte d'erreurs. L'utilisation de simplifications concernant la géométrie, ou les caractéristiques du faisceau sont généralement effectuées pour réduire le temps de calcul et le temps de travail requis pour la modélisation. Dans certains cas, un modèle plus simple est utilisé parce que le plus compliqué est inconnu. C'est le cas de l'ondulation de la table goniométrique révélée par Paolo Pelicoli à l'aide de films HDV2. L'amplitude du mouvement nécessite une résolution spatiale à l'échelle du micron pour être perceptible et une cartographie 2D de la dose pour caractériser l'oscillation que seuls les détecteurs 2D peuvent fournir. Par conséquent, l'oscillation joue un rôle dans la mesure de la dose de 1,72 % dans la mesure de l'OF et de 2,87 % pour le PVDR. La quantification de l'impact de l'oscillation est un long processus qui implique de nombreuses étapes différentes pour l'extraction de l'information sur l'oscillation, et la création de fichiers d'entrée pour le calcul MC. Le scénario le plus confortable pour l'avenir du protocole de dosimétrie serait de se débarrasser de l'oscillation, car son impact sur les grandeurs dosimétriques dépend de la vitesse de balayage. Si l'oscillation doit rester, la figure 53 peut être utilisée pour es-

timer l'incertitude sur les mesures des OF et PVDR à une profondeur de 2 cm dans la plage des vitesses de balayage testées.

L'utilisation de géométries alternatives pour bénéficier des symétries du système pour diminuer le temps de calcul a été utilisée très souvent dans cette thèse. Néanmoins, ces techniques représentent une approximation qui est quantifiée dans ce travail. La divergence du faisceau, la présence du MSC et l'air entre avant le patient, entre autres avec la présence de fenêtres en béryllium et de feuilles d'aluminium ont un impact sur les quantités dosimétriques. Le calcul dans de telles grandes géométries est très long, ce qui justifie l'utilisation du théorème semi-adjoint. Mais l'erreur faite en utilisant une telle approximation est jusqu'à 4,75 % pour le PVDR et 2,3% pour l'OF à 2 cm de profondeur. Travailler sur le fichier de géométrie fourni par Martínez-Rovira en ajoutant des sous-volumes avec des seuils choisis serait une grande valeur ajoutée pour augmenter l'efficacité du calcul. Un échantillonnage important peut être ajouté au code `penmain` lui-même pour simuler des événements pertinents et ignorer ceux qui ne contribueront pas au résultat. Par exemple, un photon primaire qui interagit avec le MSC et qui est dévié hors des limites de la zone d'intérêt pourrait être supprimé. Les particules importantes pourraient au contraire être dupliquées.

L'analyse comparative entre le détecteur `dmicroDiamond`, les films HDV2 et le FNTD révèle une différence dans les mesures de PVDR. La simple comparaison du résultat ne donne aucune information sur l'origine de la différence. Afin de mettre en évidence les raisons de ces différences, les caractéristiques du détecteur doivent être prises en compte. La méthode de Bouchard est un moyen élégant d'accéder à cette information. Par conséquent, cette méthode permet de calculer les facteurs de correction pour chaque dosimètre et de quantifier leur réponse à une irradiation. Les FNTD montrent une différence de réponse entre le pic et la vallée due principalement aux propriétés atomiques. Les films HDV2, d'autre part, se comportent de la même manière dans les pics et les vallées. L'application de la méthode Bouchard sur HDV2 et FNTD est simple et peut être exécutée avec un seul processeur dans un délai raisonnable. Le détecteur `microDiamond` réalise des mesures ponctuelles, donc l'application de la méthode Bouchard est plus difficile. Ainsi, le `microDiamond` met en évidence 3 comportements différents en fonction des conditions d'irradiation. D'abord une très bonne réponse au rayonnement dispersé si les photons primaires irradient au-dessus du substrat de carbone, une sous-réponse de 10% lorsque les photons primaires irradient le volume sensible et enfin une sous-réponse d'environ 3% quand les photons primaires rayonnent sous le substrat de carbone. Ces

résultats montrent une influence des composants non sensibles du détecteur lorsqu'il est utilisé dans des conditions d'irradiation MRT.

Les travaux actuels réalisés par Paolo Pelicioli avec des films HDV2 montrent qu'il faut prêter attention à la façon dont les films sont utilisés lorsqu'ils sont combinés avec un réservoir de PMMA. Les films sont collés sur des plaques de PMMA et insérés dans le réservoir à la profondeur désirée. Paolo a démontré que la rugosité des films et des dalles PMMA crée des espaces d'air de quelques dixièmes de microns. Ces entrefer créent une fluctuation dans les mesures des OF et PVDR.

Le défi de cette thèse était de combler l'écart entre les simulations MC et les mesures expérimentales. L'identification et la quantification des différents processus impliqués le permettent. Les calculs restent très longs, mais sont obligatoires pour rendre compte avec précision de tous ces effets. Un travail similaire devrait être effectué sur n'importe quel dosimètre utilisé en MRT.

References

- [1] Daniel N Slatkin, Per Spanne, FA Dilmanian, and Michael Sandborg. Microbeam radiation therapy. *Medical physics*, 19(6):1395–1400, 1992.
- [2] Wolfgang Zeman, HJ Curtis, EL Gebhard, and Webb Haymaker. Tolerance of mouse-brain tissue to high-energy deuterons. *Science*, 130(3391):1760–1761, 1959.
- [3] EA Siegbahn, J Stepanek, E Bräuer-Krisch, and A Bravin. Determination of dosimetric quantities used in microbeam radiation therapy (mrt) with monte carlo simulations. *Medical Physics*, 33(9):3248–3259, 2006.
- [4] Jean A Laissue, Hans Blattmann, Marco Di Michiel, Daniel N Slatkin, Nadia Lyubimova, Raphael Guzman, Werner Zimmermann, Stephan Birrer, Tim Bley, Patrick Kircher, et al. Weanling piglet cerebellum: a surrogate for tolerance to mrt (microbeam radiation therapy) in pediatric neuro-oncology. In *Penetrating Radiation Systems and Applications III*, volume 4508, pages 65–74. International Society for Optics and Photonics, 2001.
- [5] Francesc Salvat, José M Fernández-Varea, and Josep Sempau. Penelope-2008: A code system for monte carlo simulation of electron and photon transport. In *the Workshop Proceedings, June*, 2008.
- [6] M Renier, T Brochard, C Nemoz, and W Thomlinson. A white-beam fast-shutter for microbeam radiation therapy at the esrf. *Nuclear Instruments and Methods in Physics Research Section A: Accelerators, Spectrometers, Detectors and Associated Equipment*, 479(2-3):656–660, 2002.
- [7] E Bräuer-Krisch, H Requardt, T Brochard, G Berruyer, M Renier, JA Laissue, and A Bravin. New technology enables high precision multislit collimators for microbeam radiation therapy. *Review of scientific instruments*, 80(7):074301, 2009.
- [8] Jayde Livingstone, Andrew W Stevenson, Duncan J Butler, Daniel Häusermann, and Jean-François Adam. Characterization of a synthetic single crystal diamond detector for dosimetry in spatially fractionated synchrotron x-ray fields. *Medical physics*, 43(7):4283–4293, 2016.

- [9] Martin J Berger and JH Hubbell. Xcom: Photon cross sections on a personal computer. Technical report, National Bureau of Standards, Washington, DC (USA). Center for Radiation Research, 1987.
- [10] Stefan Bartzsch. *Microbeam Radiation Therapy—physical and biological aspects of a new cancer therapy and development of a treatment planning system*. PhD thesis, 2014.
- [11] Pauline Fournier. Dosimetry in synchrotron microbeam radiation therapy. 2016.
- [12] I Martínez-Rovira, J Sempau, and Y Prezado. Development and commissioning of a monte carlo photon beam model for the forthcoming clinical trials in microbeam radiation therapy. *Medical physics*, 39(1):119–131, 2012.
- [13] Jean-François Adam, Hélène Elleaume, Géraldine Le Duc, Stéphanie Corde, Anne-Marie Charvet, Irene Tropres, Jean-François Le Bas, and François Estève. Absolute cerebral blood volume and blood flow measurements based on synchrotron radiation quantitative computed tomography. *Journal of Cerebral Blood Flow & Metabolism*, 23(4):499–512, 2003.
- [14] Renato Santos Mello. Radiation dose enhancement in tumors with iodine. *Medical Physics*, 10(1):75, January 1983.
- [15] Jean A Laissue, Hans Blattmann, and Daniel N Slatkin. Alban köhler (1874-1947): inventor of grid therapy, 2012.
- [16] Mohammed Mohiuddin, Mihoko Fujita, William F Regine, Ali S Megooni, Goeffrey S Ibbott, and Mansoor M Ahmed. High-dose spatially-fractionated radiation (grid): a new paradigm in the management of advanced cancers. *International Journal of Radiation Oncology* Biology* Physics*, 45(3):721–727, 1999.
- [17] José A Peñagaricano, Eduardo G Moros, Vaneerat Ratanatharathorn, Yulong Yan, and Peter Corry. Evaluation of spatially fractionated radiotherapy (grid) and definitive chemoradiotherapy with curative intent for locally advanced squamous cell carcinoma of the head and neck: initial response rates and toxicity. *International Journal of Radiation Oncology* Biology* Physics*, 76(5):1369–1375, 2010.
- [18] Howard J Curtis. The use of a deuteron microbeam for simulating the biological effects of heavy cosmic-ray particles. *Radiation Research Supplement*, 7:250–257, 1967.

- [19] W Zeman, HJ Curtis, and CP Baker. Histopathologic effect of high-energy-particle microbeams on the visual cortex of the mouse brain. *Radiation research*, 15(4):496–514, 1961.
- [20] Daniel N Slatkin, F Avraham Dilmanian, and Per O Spanne. Method for microbeam radiation therapy, August 16 1994. US Patent 5,339,347.
- [21] Elke Bräuer-Krisch, Raphaël Serduc, EA Siegbahn, Géraldine Le Duc, Yolanda Prezado, Alberto Bravin, Hans Blattmann, and JA Laissue. Effects of pulsed, spatially fractionated, microscopic synchrotron x-ray beams on normal and tumoral brain tissue. *Mutation Research/Reviews in Mutation Research*, 704(1):160–166, 2010.
- [22] DN Slatkin, P Spanne, FA Dilmanian, JO Gebbers, and JA Laissue. Subacute neuropathological effects of microplanar beams of x-rays from a synchrotron wiggler. *Proceedings of the National Academy of Sciences*, 92(19):8783–8787, 1995.
- [23] Jean A Laissue, Gabrielle Geiser, Per O Spanne, F Avraham Dilmanian, Jan-Olaf Gebbers, Marianne Geiser, Xiao-Ye Wu, Michael S Makar, Peggy L Micca, Marta M Nawrocky, et al. Neuropathology of ablation of rat gliosarcomas and contiguous brain tissues using a microplanar beam of synchrotron-wiggler-generated x rays. *International journal of cancer*, 78(5):654–660, 1998.
- [24] Jean A Laissue, Nadia Lyubimova, Hans-Peter Wagner, David W Archer, Daniel N Slatkin, Marco Di Michiel, Christian Nemoz, Michel Renier, Elke Brauer, Per O Spanne, et al. Microbeam radiation therapy. In *Medical Applications of Penetrating Radiation*, volume 3770, pages 38–46. International Society for Optics and Photonics, 1999.
- [25] K Ribi, C Relly, MA Landolt, FD Alber, E Boltshauser, and MA Grotzer. Outcome of medulloblastoma in children: long-term complications and quality of life. *Neuropediatrics*, 36(06):357–365, 2005.
- [26] F Avraham Dilmanian, Terry M Button, Géraldine Le Duc, Nan Zhong, Louis A Peña, Jennifer AL Smith, Steve R Martinez, Tigran Bacarian, Jennifer Tammam, Baorui Ren, et al. Response of rat intracranial 9l gliosarcoma to microbeam radiation therapy. *Neuro-oncology*, 4(1):26–38, 2002.

- [27] Raphaël Serduc, Audrey Bouchet, Elke Bräuer-Krisch, Jean A Laissue, Jenny Spiga, Sukhéna Sarun, Alberto Bravin, Caroline Fonta, Luc Renaud, Jean Boutonnat, et al. Synchrotron microbeam radiation therapy for rat brain tumor palliation—influence of the microbeam width at constant valley dose. *Physics in Medicine & Biology*, 54(21):6711, 2009.
- [28] Robert J Griffin, Nathan A Koonce, Ruud P M Dings, Eric Siegel, Eduardo G Moros, Elke Bräuer-Krisch, and Peter M Corry. Microbeam radiation therapy alters vascular architecture and tumor oxygenation and is enhanced by a galectin-1 targeted anti-angiogenic peptide. *Radiation research*, 177(6):804–812, 2012.
- [29] Atsushi Uyama, Takeshi Kondoh, Nobuteru Nariyama, Keiji Umetani, Manabu Fukumoto, Kunio Shinohara, and Eiji Kohmura. A narrow microbeam is more effective for tumor growth suppression than a wide microbeam: an in vivo study using implanted human glioma cells. *Journal of synchrotron radiation*, 18(4):671–678, 2011.
- [30] Ervin B Podgorsak et al. Radiation oncology physics. *Vienna: International Atomic Energy Agency*, pages 123–271, 2005.
- [31] Jun John Sakurai. *Advanced quantum mechanics*. Pearson Education India, 1967.
- [32] Dermott E Cullen, John H Hubbell, Lynn Kissel, et al. Epdl97: the evaluated photon data library, '97 version. *UCRL-50400*, 6(5):1–28, 1997.
- [33] P Andreo, DT Burns, K Hohlfeld, M Saiful Huq, T Kanai, F Laitano, V Smyth, and S Vynckier. Absorbed dose determination in external beam radiotherapy: an international code of practice for dosimetry based on standards of absorbed dose to water. *IAEA TRS*, 398, 2000.
- [34] JC Barrett and Cory Knill. Monte carlo calculated correction factors for the ptw microdiamond detector in the gamma knife-model c. *Medical physics*, 43(3):1035–1044, 2016.
- [35] Indra J Das, George X Ding, and Anders Ahnesjö. Small fields: nonequilibrium radiation dosimetry. *Medical physics*, 35(1):206–215, 2008.
- [36] AE Nahum. Perturbation effects in dosimetry: Part i. kilovoltage x-rays and electrons. *Physics in medicine and biology*, 41(9):1531, 1996.

- [37] Irmgard Griessbach, Markus Lapp, Jörg Bohsung, Günther Gademann, and Dietrich Harder. Dosimetric characteristics of a new unshielded silicon diode and its application in clinical photon and electron beams. *Medical physics*, 32(12):3750–3754, 2005.
- [38] Y Prezado, I Martínez-Rovira, and M Sánchez. Scatter factors assessment in microbeam radiation therapy. *Medical physics*, 39(3):1234–1238, 2012.
- [39] Philip Willmott. *An introduction to synchrotron radiation: techniques and applications*. John Wiley & Sons, 2011.
- [40] J. F. Adam, M. C. Biston, J. Rousseau, C. Boudou, a. M. Charvet, J. Balosso, F. Estève, and H. Elleaume. Heavy element enhanced synchrotron stereotactic radiotherapy as a promising brain tumour treatment. *Physica Medica*, 24(2):92–97, 2008.
- [41] Layal Obeid, Pierre Deman, Alexandre Tessier, Jacques Balosso, François Estève, and Jean-François Adam. Absolute perfusion measurements and associated iodinated contrast agent time course in brain metastasis: a study for contrast-enhanced radiotherapy. *Journal of cerebral blood flow and metabolism : official journal of the International Society of Cerebral Blood Flow and Metabolism*, 34(4):638–45, 2014.
- [42] M Baumann and Cordula Petersen. Tc_p and ntc_p: a basic introduction. *Rays*, 30(2):99–104, 2005.
- [43] John P Kirkpatrick, Jeffrey J Meyer, and Lawrence B Marks. The linear-quadratic model is inappropriate to model high dose per fraction effects in radiosurgery. In *Seminars in radiation oncology*, volume 18, pages 240–243. Elsevier, 2008.
- [44] Elke Bräuer-Krisch, Jean-Francois Adam, Enver Alagoz, Stefan Bartzsch, Jeff Crossbie, Carlos DeWagter, Andrew Dipuglia, Mattia Donzelli, Simon Doran, Pauline Fournier, et al. Medical physics aspects of the synchrotron radiation therapies: Microbeam radiation therapy (mrt) and synchrotron stereotactic radiotherapy (ssrt). *Physica Medica*, 31(6):568–583, 2015.
- [45] Greg I Kaplan, Anatoly B Rosenfeld, Barry J Allen, Jeremy T Booth, Martin G Carolan, and Andrew Holmes-Siedle. Improved spatial resolution by mosfet dosimetry of an x-ray microbeam. *Medical physics*, 27(1):239–244, 2000.

- [46] A Chalkley and G Heyes. Evaluation of a synthetic single-crystal diamond detector for relative dosimetry measurements on a cyberknife™. *The British journal of radiology*, 87(1035):20130768, 2014.
- [47] Yolanda Prezado, Mathias Vautrin, I Martínez-Rovira, Alberto Bravin, François Estève, Hélène Elleaume, P Berkvens, and Jean-François Adam. Dosimetry protocol for the forthcoming clinical trials in synchrotron stereotactic radiation therapy (ssrt). *Medical physics*, 38(3):1709–1717, 2011.
- [48] Y Prezado, I Martínez-Rovira, S Thengumpallil, and P Deman. Dosimetry protocol for the preclinical trials in white-beam minibeam radiation therapy. *Medical physics*, 38(9):5012–5020, 2011.
- [49] Hugo Bouchard, Jan Seuntjens, Simon Duane, Yuji Kamio, and Hugo Palmans. Detector dose response in megavoltage small photon beams. i. theoretical concepts. *Medical physics*, 42(10):6033–6047, 2015.
- [50] Hugo Bouchard, Jan Seuntjens, Jean-Francois Carrier, and Iwan Kawrakow. Ionization chamber gradient effects in nonstandard beam configurations. *Medical physics*, 36(10):4654–4663, 2009.
- [51] LV Spencer and FH Attix. A theory of cavity ionization. *Radiation research*, 3(3):239–254, 1955.
- [52] TE Burlin. A general theory of cavity ionisation. *The British journal of radiology*, 39(466):727–734, 1966.
- [53] S Almviva, Marco Marinelli, E Milani, G Prestopino, A Tucciarone, C Verona, G Verona-Rinati, M Angelone, M Pillon, I Dolbnya, et al. Chemical vapor deposition diamond based multilayered radiation detector: Physical analysis of detection properties. *Journal of applied physics*, 107(1):014511, 2010.
- [54] Marco Marinelli, G Prestopino, C Verona, and G Verona-Rinati. Experimental determination of the ptw 60019 microdiamond dosimeter active area and volume. *Medical physics*, 43(9):5205–5212, 2016.
- [55] James P Sethna. Entropy, order parameters, and complexity. *Statistical Mechanics, Laboratory of Atomic and Solid State Physics, Cornell University, Ithaca, NY*, pages 14853–2501, 2006.

- [56] Peter Hellekalek. Good random number generators are (not so) easy to find. *Mathematics and Computers in Simulation*, 46(5-6):485–505, 1998.
- [57] MH Kalos and PA Whitlock. Monte carlo methods, vol. 1. *Basics: Wiley & Sons, New York, USA*, 1986.
- [58] William H Press, Saul A Teukolsky, William T Vetterling, and Brian P Flannery. Numerical recipes in c++. *The art of scientific computing*, 1992.
- [59] Julio Almansa, Francesc Salvat-Pujol, Gloria Díaz-Londoño, Artur Carnicer, Antonio M Lallena, and Francesc Salvat. Pengeom—a general-purpose geometry package for monte carlo simulation of radiation transport in material systems defined by quadric surfaces. *Computer Physics Communications*, 199:102–113, 2016.
- [60] DC Irving. The adjoint boltzmann equation and its simulation by monte carlo. *Nuclear Engineering and Design*, 15:273–293, 1971.
- [61] Ivan Lux and László Koblinger. *Monte Carlo particle transport methods: neutron and photon calculations*, volume 102. CRC press Boca Raton, Florida, 1991.
- [62] RB Cruise, RW Sheppard, and VP Moskvina. Parallelization of the penelope monte carlo particle transport simulation package. *Nuclear Mathematical and Computational Sciences: A Century in Review, A Century Anew*, pages 6–11, 2003.
- [63] C Bernard. C. bernard (milc collaboration), phys. rev. d 65, 054031 (2002). *Phys. Rev. D*, 65:054031, 2002.
- [64] W Keith Hastings. Monte carlo sampling methods using markov chains and their applications. 1970.
- [65] Y Namito, S Ban, and Ho Hirayama. Implementation of the doppler broadening of a compton-scattered photon into the egs4 code. *Nuclear Instruments and Methods in Physics Research Section A: Accelerators, Spectrometers, Detectors and Associated Equipment*, 349(2-3):489–494, 1994.
- [66] Dermott E Cullen. A simple model of photon transport. *Nuclear Instruments and Methods in Physics Research Section B: Beam Interactions with Materials and Atoms*, 101(4):499–510, 1995.

- [67] D Brusa, G Stutz, JA Riveros, JM Fernández-Varea, and F Salvat. Fast sampling algorithm for the simulation of photon compton scattering. *Nuclear Instruments and Methods in Physics Research Section A: Accelerators, Spectrometers, Detectors and Associated Equipment*, 379(1):167–175, 1996.
- [68] JM Fernández-Varea, D Liljequist, S Csillag, R Rätty, and F Salvat. Monte carlo simulation of 0.1–100 keV electron and positron transport in solids using optical data and partial wave methods. *Nuclear Instruments and Methods in Physics Research Section B: Beam Interactions with Materials and Atoms*, 108(1-2):35–50, 1996.
- [69] R Ribberfors. X-ray incoherent scattering total cross sections and energy-absorption cross sections by means of simple calculation routines. *Physical Review A*, 27(6):3061, 1983.
- [70] Martin J Berger. Monte carlo calculation of the penetration and diffusion of fast charged particles. Technical report, 1963.
- [71] Alex F Bielajew and DWO Rogers. Presta: The parameter reduced electron-step transport algorithm for electron monte carlo transport. *Nuclear Instruments and Methods in Physics Research Section B: Beam Interactions with Materials and Atoms*, 18(1-6):165–181, 1986.
- [72] Edward W Larsen. A theoretical derivation of the condensed history algorithm. *Annals of Nuclear Energy*, 19(10-12):701–714, 1992.
- [73] Iwan Kawrakow and Alex F Bielajew. On the representation of electron multiple elastic-scattering distributions for monte carlo calculations. *Nuclear Instruments and Methods in Physics Research Section B: Beam Interactions with Materials and Atoms*, 134(3):325–336, 1998.
- [74] Iwan Kawrakow and Alex F Bielajew. On the condensed history technique for electron transport. *Nuclear Instruments and Methods in Physics Research Section B: Beam Interactions with Materials and Atoms*, 142(3):253–280, 1998.
- [75] Iwan Kawrakow. Accurate condensed history monte carlo simulation of electron transport. i. egsnrc, the new egs4 version. *Medical physics*, 27(3):485–498, 2000.
- [76] Hugo Bouchard, Yuji Kamio, Hugo Palmans, Jan Seuntjens, and Simon Duane. Detector dose response in megavoltage small photon beams. ii. pencil beam perturbation effects. *Medical physics*, 42(10):6048–6061, 2015.

- [77] J Sempau, JM Fernandez-Varea, E Acosta, and F Salvat. Experimental benchmarks of the monte carlo code penelope. *Nuclear Instruments and Methods in Physics Research Section B: Beam Interactions with Materials and Atoms*, 207(2):107–123, 2003.
- [78] JMC Brown, MR Dimmock, JE Gillam, and DM Paganin. A low energy bound atomic electron compton scattering model for geant4. *Nuclear Instruments and Methods in Physics Research Section B: Beam Interactions with Materials and Atoms*, 338:77–88, 2014.
- [79] I Orion, AB Rosenfeld, FA Dilmanian, F Telang, B Ren, and Y Namito. Monte carlo simulation of dose distributions from a synchrotron-produced microplanar beam array using the egs4 code system4. *Physics in Medicine & Biology*, 45(9):2497, 2000.
- [80] EA Siegbahn, E Bräuer-Krisch, J Stepanek, H Blattmann, JA Laissue, and A Bravin. Dosimetric studies of microbeam radiation therapy (mrt) with monte carlo simulations. *Nuclear Instruments and Methods in Physics Research Section A: Accelerators, Spectrometers, Detectors and Associated Equipment*, 548(1-2):54–58, 2005.
- [81] J Stepanek, H Blattmann, JA Laissue, N Lyubimova, M Di Michiel, and DN Slatkin. Physics study of microbeam radiation therapy with psi-version of monte carlo code geant as a new computational tool. *Medical physics*, 27(7):1664–1675, 2000.
- [82] Iwan Cornelius, Susanna Guatelli, Pauline Fournier, Jeffrey C Crosbie, Manuel Sanchez del Rio, Elke Bräuer-Krisch, Anatoly Rosenfeld, and Michael Lerch. Benchmarking and validation of a geant4–shadow monte carlo simulation for dose calculations in microbeam radiation therapy. *Journal of synchrotron radiation*, 21(3):518–528, 2014.
- [83] M De Felici, R Felici, C Ferrero, A Bravin, A Tartari, and M Gambaccini. Monte carlo assessment of peak-to-valley dose ratio for mrt. *Nuclear Instruments and Methods in Physics Research Section A: Accelerators, Spectrometers, Detectors and Associated Equipment*, 580(1):489–492, 2007.
- [84] Richard P Hugtenburg, AS Adegunloye, and David A Bradley. X-ray microbeam radiation therapy calculations, including polarisation effects, with the monte carlo code egs5. *Nuclear Instruments and Methods in Physics Research Section A: Accelerators, Spectrometers, Detectors and Associated Equipment*, 619(1-3):221–224, 2010.

- [85] M De Felici, EA Siegbahn, Jenny Spiga, AL Hanson, R Felici, C Ferrero, A Tartari, M Gambaccini, J Keyriläinen, E Bräuer-Krisch, et al. Monte carlo code comparison of dose delivery prediction for microbeam radiation therapy. In *Journal of Physics: Conference Series*, volume 102, page 012005. IOP Publishing, 2008.
- [86] KE Goldstone. Tissue substitutes in radiation dosimetry and measurement, in: ICRU report 44. international commission on radiation units and measurements, usa (1989), 1990.
- [87] GM Akselrod, MS Akselrod, ER Benton, and N Yasuda. A novel al 2 o 3 fluorescent nuclear track detector for heavy charged particles and neutrons. *Nuclear Instruments and Methods in Physics Research Section B: Beam Interactions with Materials and Atoms*, 247(2):295–306, 2006.
- [88] Christelle Huet, Cyril Moignier, Victor Barraux, Cédric Loiseau, Karine Sebe-Mercier, Alain Batalla, and Isabelle Clairand. Study of commercial detector responses in non-equilibrium small photon fields of a 1000mu/min cyberknife system. *Physica Medica*, 32(6):818–825, 2016.
- [89] KA Johansson, LO Mattsson, L Lindborg, and H Svensson. Absorbed-dose determination with ionization chambers in electron and photon beams having energies between 1 and 50 mev. In *National and international standardization of radiation dosimetry*. 1978.
- [90] Nordic Association of Clinical Physics (NACP). Procedures in external radiation therapy dosimetry with electron and photon beams with maximum energies between 1 and 50 mev. *Acta radiol. Oncology*, 19:55, 1980.
- [91] Ravinder Nath and RJ Schulz. Calculated response and wall correction factors for ionization chambers exposed to 60co gamma-rays. *Medical Physics*, 8(1):85–93, 1981.
- [92] AAPM Task Group 21, Radiation Therapy Committee. A protocol for the determination of absorbed dose from high-energy photon and electron beams. *Medical Physics*, 10(6):741–771, 1983.
- [93] DWO Rogers, AF Bielajew, and AE Nahum. Ion chamber response and a wall correction factors in a 60co beam by monte carlo simulation. *Physics in Medicine & Biology*, 30(5):429, 1985.

- [94] Alex F Bielajew. Ionisation cavity theory: a formal derivation of perturbation factors for thick-walled ion chambers in photon beams. *Physics in Medicine & Biology*, 31(2):161, 1986.
- [95] J Sempau, A Sanchez-Reyes, F Salvat, H Oulad ben Tahar, SB Jiang, and JM Fernández-Varea. Monte carlo simulation of electron beams from an accelerator head using penelope. *Physics in Medicine & Biology*, 46(4):1163, 2001.
- [96] Dermott E. Cullen. A survey of photon cross section data for use in epics2017. *IAEA Nuclear Data Services*, IAEA-NDS-225(rev.1):30, 2018.
- [97] Lorenzo Sabbatucci and Francesc Salvat. Theory and calculation of the atomic photoeffect. *Radiation Physics and Chemistry*, 121:122–140, 2016.

Appendices

A Towards *in vivo* dosimetry for contrast enhanced synchrotron stereotactic radiation therapy based on iodine x-ray spectroscopy

PAPER


Towards *in vivo* dosimetry for contrast enhanced synchrotron stereotactic radiation therapy based on iodine x-ray spectroscopy

To cite this article: Dimitri Reynard *et al* 2018 *Biomed. Phys. Eng. Express* **4** 045015

View the [article online](#) for updates and enhancements.



PAPER

Towards *in vivo* dosimetry for contrast enhanced synchrotron stereotactic radiation therapy based on iodine x-ray spectroscopyRECEIVED
31 January 2018REVISED
30 April 2018ACCEPTED FOR PUBLICATION
8 May 2018PUBLISHED
17 May 2018Dimitri Reynard^{1,2} , Richard P. Hugtenburg^{2,3}, François Estève⁴ and Jean-François Adam⁴¹ Université Grenoble Alpes, 15 rue des Universités, St Martin D'Herès, 38400, France² Swansea University, Singleton Park Campus, Sketty, Swansea SA2 8PP, United Kingdom³ Singleton Hospital, Abertawe Bro Morgannwg University Health Board, Singleton Park, Swansea SA2 8QA⁴ E.A. Rayonnement Synchrotron et Recherche Médicale, Université Grenoble Alpes, Grenoble, FranceE-mail: jean_francois.adam@esrf.frKeywords: *In-Vivo* dosimetry, Contrast enhanced radiation therapy, fluorescence, tomography

Abstract

The first trial applications of Contrast-Enhanced Synchrotron Stereotactic Radiation Therapy (SSRT) is underway since June 2012 at the European Synchrotron Radiation Facility (ESRF) in Grenoble (France). The phase I-II clinical trial is designed to test the feasibility and safety of SSRT through a dose escalation protocol. Contrast enhanced radiotherapy achieves localized dose enhancement due to higher photoelectric effect rate in the target. This increase is obtained through the preferential uptake of high-Z media (iodine) in the tumoral area combined with irradiations with medium energy synchrotron x-rays. *In vivo* dosimetry (i.e. experimental dosimetry in real time during the treatment) would be a serious added value to the project, in terms of online dose monitoring and quality control. It is challenging to perform *in vivo* dosimetry with the currently available conventional clinical techniques. In this work we investigated a method using x-ray fluorescence detection to derive the iodine concentration contained in a tumor during the treatment of a patient, as a first step towards *in vivo* dosimetry. A mean iodine concentration of 0.33 ± 0.22 mg/ml has been retrieved in the tumor of the patient compared to 2 mg/ml expected would correspond to 3% local dose enhancement in the tumor. Further work will be performed to improve the attenuation correction method. The expected amount of iodine should be 2 mg/ml in the tumor (20% dose enhancement). This method is suitable to detect iodine in the target but has some problem in quantifying the real amount of iodine present during the irradiation.

This study takes place within the scope of phase I/II clinical trials of Stereotactic Synchrotron Radiation Therapy (SSRT). The trial is designed to prove the feasibility and safety of SSRT through a dose escalation protocol. The patients who benefits from this modality suffer from brain metastasis of medium to small volume.

SSRT consists in loading a tumor with an iodinated contrast agent (CA) through intravenous injections. The CA selectively leaches into the tumor because of the localised blood brain barrier (BBB) permeabilisation [1]. The impaired BBB and hence iodine biodistribution is directly related to the tumor presence. Moreover the iodine is located in the interstitial space and in the vessels so the dose will be delivered to the target cells and neovasculature, under the assumption of an homogeneous emission of the secondary

particle [2]. The combination of CA and a stereotactic irradiation with mono-energetic kilovoltage x-rays produces a gradient in the absorption cross-section leading to an increased dose deposition [3]. A differential effect is produced between the tumor and the healthy brain depending on the iodine uptake, leading to a difference in the photon interaction mechanisms. The photoelectrons produced in the target volume deposit their energy over a sub-millimetric distance in the vicinity of heavy atoms, whereas Compton scattering predominates in the surrounding healthy tissues. As a consequence, the dose deposition upstream and downstream the tumor is further reduced while the dose in the tumoral tissue is reinforced. This differential effect is a substantial added value to the high energy treatments performed nowadays. Robar *et al* studied the use of iodine as a radiosensitizer in

conventional SRT (energy beam ranging from 2 MV to 18 MV) and reported a dose enhancement factor (DEF) for iodine concentration around 3 mg/ml of iodine of less than 1.6% [4]. On the other hand Edouard *et al* reported a DEF of 10% per mg/ml of iodine during the SSRT treatment [5]. At high energy, the DEF is then negligible, hence the necessity of using a low-medium energy x-ray source. In order to achieve a satisfying DEF a synchrotron source is not mandatory, only the photon energy matters. A first clinical trial performed in the 90's [6] used a modified x-ray tube and presented a total treatment time of 45 min (3×15 min with cooling periods in between) because of the need of cooling down the x-ray tube. However, a synchrotron offers significant advantages compared to a conventional x-ray tube, in offering tunable monochromatic high flux x-ray beam, and a substantial reduction of the treatment time (20 min including positioning), and the optimal energy between high DEF and low dose to the bone can be chosen [5]. The iodine injection is thus only used for the SSRT fraction of the treatment.

There is a linear relationship between the localized dose enhancement and the iodine concentration, as shown by [7]. A localized 10% increase per mg/ml is achieved in the tumor when compared to an irradiation at the same energy, without contrast agent. The treatment planning system is taking the iodine presence into account for the calculation (Monte Carlo based treatment planning system). As well as radiotherapy programs, innovative x-ray imaging techniques using the inherent properties of synchrotron radiation such as the high photon flux density, the broad energy spectrum, the natural collimation and the linear polarization are under active development.

Fluorescence spectroscopy is commonly used to detect low contents of specific heavy atomic number elements in material science. Until now fluorescence hadn't been used to assess the iodine concentration and its resulting dose enhancement. Applying this technique to medical imaging, it becomes conceivable to track down the iodine uptake of an organ without the low sensitivity of conventional CT acquisitions [8]. The measurement of the distribution of iodine within the thyroid gland [9] has been made using Fluorescence x-ray Computed Tomography (FXCT) [10]. Later in 2005 the cerebral perfusion of a living mouse has been retrieved using FXCT [11]. Nevertheless, FXCT is not appropriate for the purpose of SSRT for reasons linked to the irradiation time, and scale problems due to the brain and skull thicknesses in human. Moreover, the small detection volume in the detector makes the measurement of fluorescence x-rays a rare event due to small detection solid angle, so compromise between spatial resolution and measurement's statistical reliability has to be found.

During SSRT treatment, the irradiated iodine atoms emit characteristic x-rays (K_{α} line at 28.5 keV) whose amount depends directly on the iodine

concentration in the tumor. The exact measurement of the tumor's CA uptake would be a serious added value in terms of on line dose monitoring and quality assurance. In any case, it should be noted that the irradiation in SSRT consists on 3 to 10 weighted beams distributed around the patient's skull, which is an other reason why FXCT as commonly used is not appropriate. The substantial thickness of tissue in human skull and the low number of beams incidence are technical rationales sufficient to investigate a simpler alternative to FXCT, in which 3D iodine average concentration can be retrieved.

Therefore the aim of this work is to examine the feasibility retrieving absolute iodine concentration in real time during the SSRT treatment as a first step towards *in vivo* dosimetry in SSRT. The feasibility of fluorescence detection was examined by preliminary Monte-Carlo simulations using the code PENELOPE (Penetration and ENERGY LOSS of Positrons and Electrons) involving an analytical human head phantom as the geometry used for parametric study [7]. A calibration data of iodine content was obtained from tubes filled with various concentrations of iodine and irradiated with synchrotron monochromatic low-energy x-rays. A model was then developed to relate the fluorescence rate detected to the iodine amount. Finally this model was used to determine the average iodine concentration in patients tumors during treatments. This is the first mandatory step to propose an *in vivo* dosimetry modality in SSRT.

1. Material and methods

1.1. Monte-Carlo simulation

The aim is to retrieve the signal generated by the K_{α} line of iodine which is at an average energy of 28.5 keV composed of $K_{\alpha 1}$ (28.61 keV) and $K_{\alpha 2}$ (28.32 keV) and accounts for about 85% of the lines produced after a K-shell ionisation [12], the other 15% are coming from Auger emission. At these energies the average mass attenuation coefficient of the brain tissue is around $0.381 \text{ l cm}^2/\text{g}$ ($1.331 \text{ cm}^2/\text{g}$ for the skull, bone, ICRU-44 [13]). By considering a tumor 5 cm in depth behind a skull of 1 cm thick, we can simply calculate the amount of fluorescence that comes out from the head using the Beer-Lambert law in a given direction. It is less than 0.05% of the fluorescence generated. Moreover, the detector receives only photons emitted in a well defined solid angle which results in a further fall of the count rate due to the isotropic fluorescence emission.

The environment of the tumor (brain, skull, skin) and its size enlarges the scattered photon rate which could in a sense worsen the signal to noise ratio (SNR). As a consequence, the first point that is investigated is the feasibility of the spectrometric measurement in SSRT by the mean of Monte-Carlo simulations. For this purpose, the Monte-Carlo code PENELOPE is

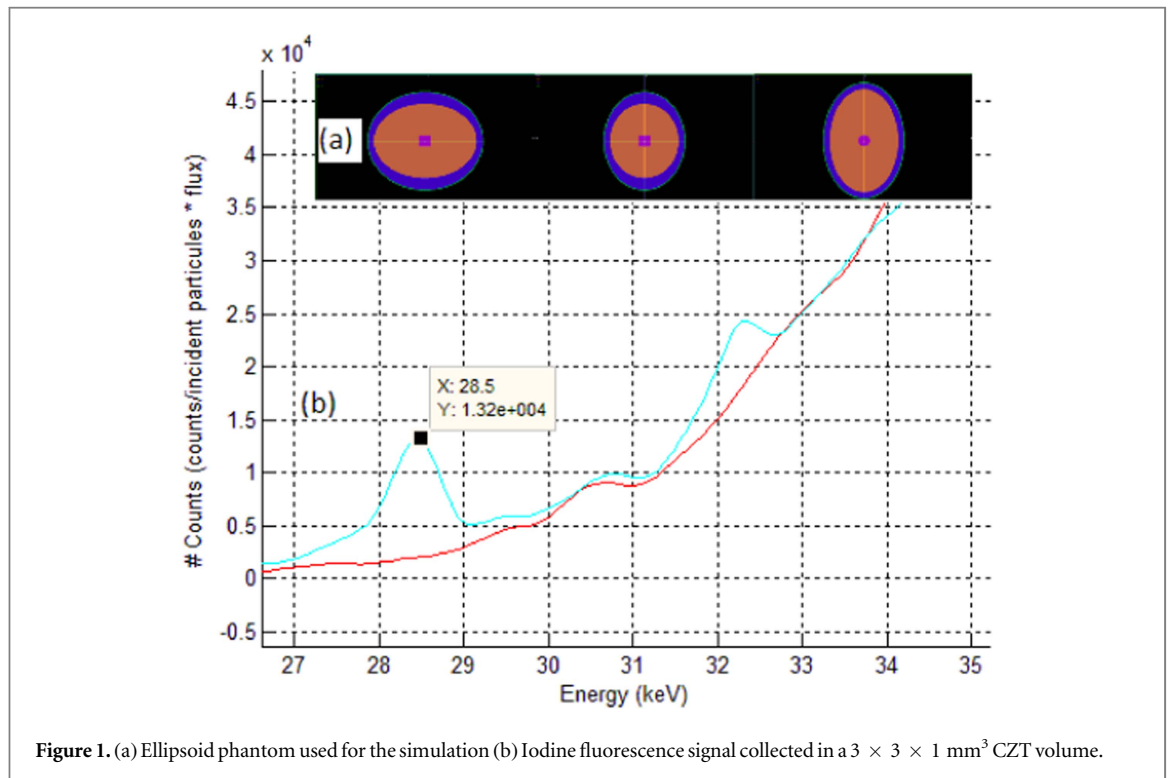


Figure 1. (a) Ellipsoid phantom used for the simulation (b) Iodine fluorescence signal collected in a $3 \times 3 \times 1 \text{ mm}^3$ CZT volume.

used together with code PENGEOm to define geometry files (bodies).

An analytical human head phantom is used, described by Bouchet and al [14] adapted from nuclear medicine studies using the MIRD formalism. A tumor is modeled by a cylinder (2 cm height, 2 cm diameter) filled with a homogeneous mixture of brain material and iodine at various concentrations ranking from 0 to 20 mg/ml. The tumor is positioned at the center of the brain as shown in figure 1. The materials that fill the bodies are adapted from the database of the ESTAR program of Berger [15] for the brain, skull and skin. As far as mixtures and compounds are concerned, the weighted sum method is adopted to define the material cross sections, which means that the corresponding molecular cross section is set equal to the sum of atomic cross sections weighted with the stoichiometric index of the element.

A small CdZnTe (CZT) cuboid of $3 \times 3 \times 1 \text{ mm}^3$ is set as an energy deposition detector and placed according to the x -axis. Finally, the simulated beam is a $2 \times 2 \text{ cm}^2$ square field, polarized, parallel and monochromatic at the energy of 80 keV emitting photons along the y -axis to form a 90 degrees angle with the detector. The irradiation is performed in the xy -plane and the number of photons simulated accounts for 10^9 . Electron and photon cut-off are both set at 25 keV as this value is lower than the $K_{\alpha 1}$ and $K_{\alpha 2}$ for iodine and particles with such energy cannot produce fluorescence from the iodine K edge which is of interest here. Coefficients C1 and C2 are both set at 0 for a fully detailed simulation of the scattered radiation. The spectra obtained are then processed to simulate a real spectrum acquired with a CZT detector [16]. This

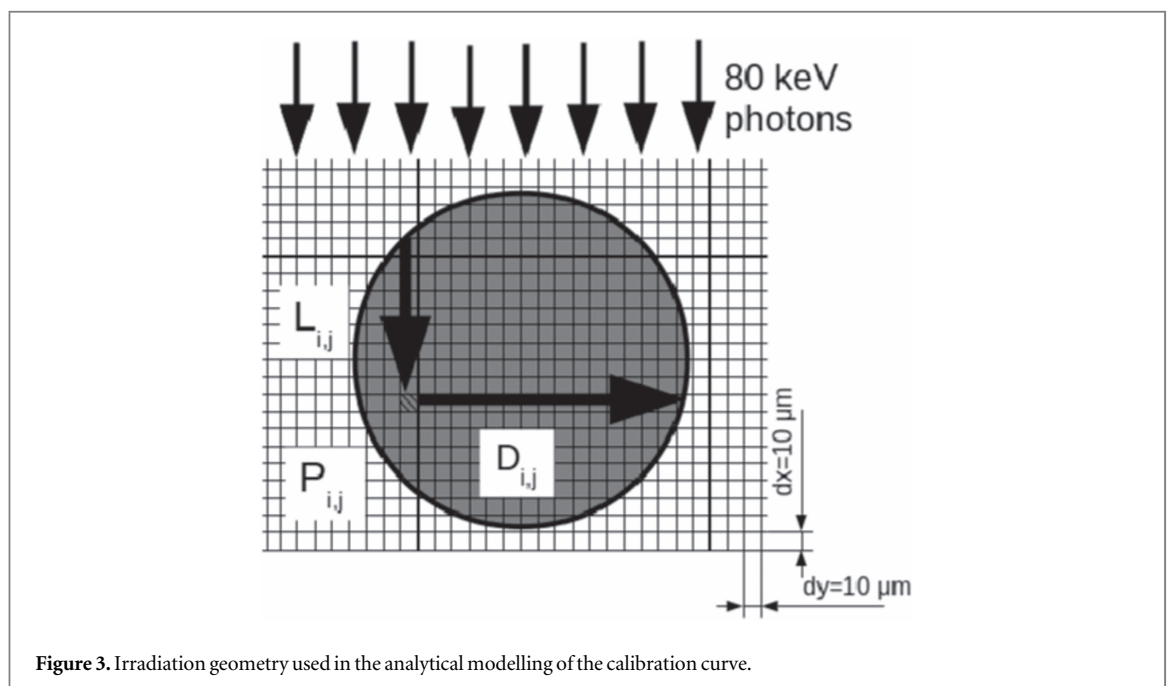
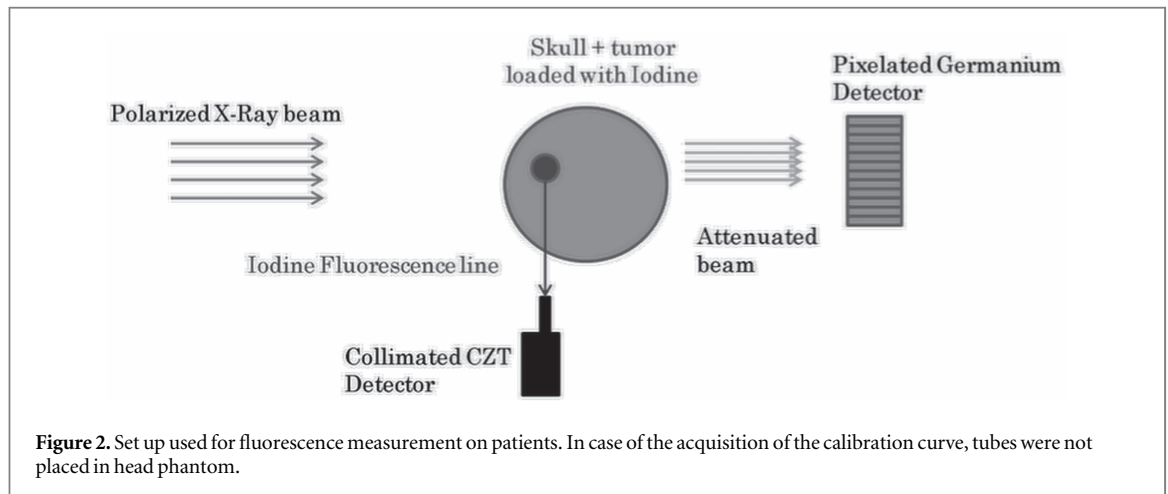
numerical treatment distributes a certain amount of counts from the full energy peak at lower energy channels, and the peak is enlarged as a Gaussian distribution. In other words, the procedure considers the statistical spread in the number of charge carriers and charge collection phenomena. The MC simulations are performed to evaluate the fluorescence detection feasibility in a clinical case.

1.2. Analytical model for iodine concentration quantification

As the fluorescence rate depends on the iodine concentration, the volume irradiated, the incident flux and the irradiation time, a calibration curve is realized to characterize the iodine concentration in the tumor.

The set up used is basically an FXCT set up as described on figure 2 with a Amptek CZT detector with a detection volume of $3 \times 3 \times 1 \text{ mm}^3$ placed at 90 degrees of the incident beam and at 155.2 cm from the isocenter. This way of positioning the fluorescence detector reduces the background from Compton scattering. This improves the detectability of the fluorescence x-rays by taking advantage of the linear polarisation of the synchrotron beam [17]. A 2 millimeters pinhole is used to geometrically select the photons coming from the isocenter and to reduce the amount of scattered photons detected. Despite these collimation elements a significant aperture remains and represents a circle of 15 cm in radius at the level of the isocenter.

An array of solutions with concentrations varying from 0 to 20 mg/ml are prepared and placed into cylindrical plastic tubes of 3 cm in diameter and 3 cm high. Absolute iodine concentrations is derived from



monochromatic computed tomography (CT) images of the tubes using the subtraction of a CT image of a tube filled with pure water [18]. The tubes are thus irradiated with a 2 mm thick beam at 80 keV using 2 irradiation modes, static and bottom to top scanning with the same irradiation time. Finally, the spectrum acquired are processed to remove the background from scattered photons using the 3 channels method [19] and to extract the fluorescence rate.

This simple experiment is also simulated using MatLab (MATLAB 9.1, The MathWorks Inc., Natick, MA, 2000). The tube is divided into pixels $10 \mu\text{m} \times 10 \mu\text{m}$ ($dx \times dy$) as shown of figure 3. The emitted fluorescence $f_{i,j}$ in a given pixel $P_{i,j}$ is calculated with equation (1). If we assume an equal iodine concentration $[I]$ for each pixel of the target, the amount of fluorescence delivered by a given pixel $P_{i,j}$ depends only on the amount of pixels filled with iodine that the photon flux Φ impacts before the interaction with the pixel emitter. This number multiplied by dx defines

the depth $L_{i,j}$ for each pixel $P_{i,j}$ with regards to the entrance beam.

$$f_{i,j} = \tau \mu_{pe80} dx \cdot \Phi e^{-\mu_{80} L_{i,j}} \quad (1)$$

With τ the fluorescence yield of the K_{α} line of iodine μ_{pe80} and μ_{80} the linear attenuation coefficient of the photoelectric effect at 80 keV for the solution in a given voxel, dx the length of the pixel and total attenuation coefficient respectively, Φ the ESRF photon fluence, $L_{i,j}$ the depth of the pixel $P_{i,j}$. Considering the distance $D_{i,j}$ of the emitted fluorescence $f_{i,j}$ in the direction of the detector inside the tube, the detected fluorescence is calculated using equation (2).

$$f_{det}(I) = \frac{\Omega}{n} \sum_{i,j} f_{i,j} e^{-\frac{\mu_{tot}(I)}{\rho} \rho \cdot D_{i,j}} \quad (2)$$

with $\frac{\mu_{tot}(I)}{\rho}$ as the total linear attenuation coefficient of the iodine mixture calculated in the diluted approximation solution using equation (3).

Table 1. Irradiation/Simulation parameters.

| | |
|-------------|--|
| Φ | $3 \cdot 10^{12} \text{ ph/cm}^2/\text{s}$ |
| Beam width | 3 cm |
| Beam height | 2 mm |
| τ | 0.8 |
| Ω | $3.18 \cdot 10^{-7} \text{ sr}$ |

$$\frac{\mu_{tot}([I])}{\rho} = \left[\frac{\mu}{\rho} \right]_{H_2O} \times (1 - [I] \cdot 10^{-3}) + \left[\frac{\mu}{\rho} \right]_I \times [I] \cdot 10^{-3} \quad (3)$$

Where Ω the solid angle defined by the emitting pixel to the aperture of the detector, n is the number of pixels in the tube. Using the irradiation parameters described by table 1. The results of the calculation are compared to the fluorescence measurement to validate the calibration curve.

1.3. Measurement during patient treatment

The experimental set up is exactly the same as in the previous part (figure 2). The tumor of the patient is placed at the isocenter of the treatment room and the irradiation is performed using several incidences (3 to 8 for the 3 patients studied here).

In order to maximise the spare of healthy tissue, every beam is shaped by a Cerobend mask placed between the x-ray source and the patient, according to the limits of the Plan Target Volume (PTV) plus a 3 mm margin. The fluorescence spectrums are acquired for every beam incidences and processed to retrieve the iodine concentration in the tumor. Figure 4 shows a print screen of the treatment plan used in SSRT and allows the visualisation of the beam incidences.

Firstly, spectrums are filtered using a low pass filter in the Fourier space to remove the statistical noise which is expressed through fast oscillations. Both the peak stripping method and the 3 channels method are used to remove the background and return the same results. Peak stripping method is a way of spectrum calculation that detects peaks and iteratively merges them to the background line [19]. As for the 3 channels method, it geometrically adjusts a trapezium under the peak and removes it.

For the spectrum calculation only the 3 channels method is used because this technique is the fastest.

In the general case, when the fluorescence rate is retrieved for each beam incidence, a normalisation procedure could be applied. The idea is that the total irradiated volume is set by the Cerobend masks which shapes come directly from the TPS and is not depending on the irradiation incidence. Therefore the iodinated irradiated volume remains the same during the whole treatment. Retrieving the iodine concentration in the tumor would require the normalization of the

fluorescence rate to the same irradiation conditions as the tubes in order to compare directly the fluorescence rate in both cases. Such normalization should account for the irradiation time, the photon flux which decreases with time and tissue attenuation. But in SSRT one can benefit from the fact that each of the irradiation port delivers the same dose to the isocenter ($\frac{1}{8}$ of 7Gy). One key aspect that is investigated is how the measured fluorescence varies with the dose to the medium. In the case where the dependence is proportional, the normalization to the incoming fluence becomes pointless and the only remaining step between fluorescence measurement and iodine concentration retrieval is tissue attenuation correction for 28.5 keV photons (Iodine's K_{alpha} line). For this purpose, a serie of MC simulations involving tubes 3 cm in diameter 3 cm high filled with 5 mg/ml of iodinated solution and 1 cm thick slabs of brain material is used. The brain slabs are positioned between the 80 keV photon source and the tube. The brain thickness ranges from 1 cm to 4 cm. In the mean time the same experiment is realized with a tube filled with 5 mg/ml of iodinated solution and brain slabs from the CIRS (CIRS, Norfolk, VA, USA), radiosurgery phantom MODEL605.

The beam used for the imaging procedure is the same used for the treatment which is a monoenergetic 80 keV beam. At the ESRF the tomography reconstruction algorithm generates CT scans where pixel values are the linear attenuation coefficient at the scanning energy.

Therefore, tissue attenuation correction for 28.5 keV photons is computed from a patient specific CT scan realized between the iodine injection and the patient irradiation. The resolution of the CT scan is 841×841 with a pixel size of $336 \times 336 \mu\text{m}^2$. The extrapolation of mass attenuation coefficient obtained on the CT image to the value required for 28.5 keV photons is calculated using the method described by Schneider and al [20]. In this method the Hounsfield units (in our case the grey values of the image) at a given energy of each material are sorted. Any in between Hounsfield unit present in the image is then described as a mixture of the two elements matching two closest material Hounsfield unit values. The mass attenuation coefficient at 28.5 keV from the NIST database for each material is finally used to extrapolate the CT image at 28.5 keV.

For the purpose of this work 3 regions are defined. The first one is a mixture of brain tissue and iodine [8] has stated that a small amount of iodine remains in the brain tumoral tissue after the injection so this segmentation is applied for Hounsfield units close to the tumoral tissue. For regions close to the bone, materials are described as a mixture of brain and spongy bone. The skull being a sequence of spongy bone and cortical bone, any Hounsfield unit around the spongy bone value will be treated as a mixture of spongy bone and cortical bone. The last region is treated as cortical bone

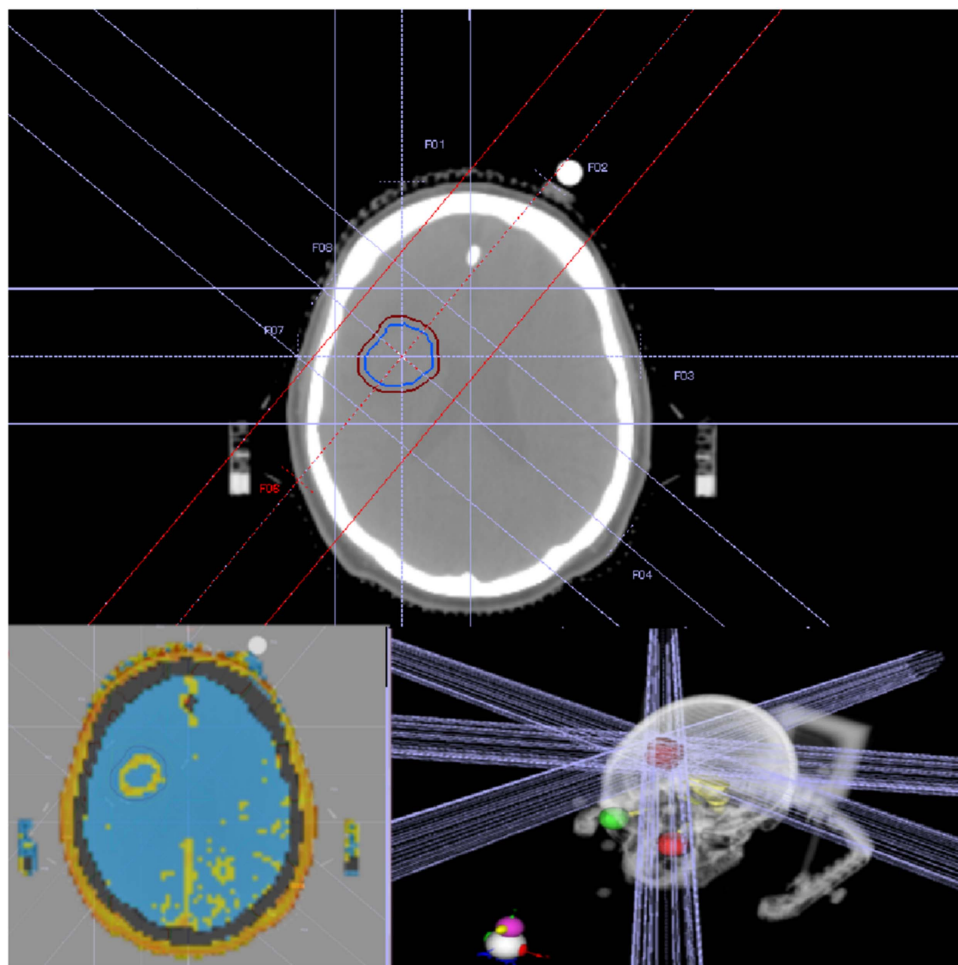


Figure 4. CT Scan extracted from the TPS. The tumor is irradiated with 8 weighted beams (bottom right hand corner). The material segmentation (bottom left hand corner) shows the ring shaped iodine uptake at the isocenter height.

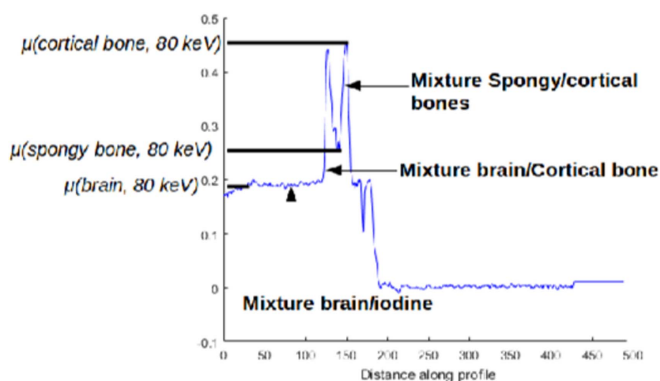


Figure 5. Profile from the 80 keV CT scan. Distance 0 is at the isocenter and the profile crosses the brain and the skull.

only. Figure 5 shows a profile from the 80 keV CT scan. The values of the linear attenuation coefficient for each material is extracted from the NIST database. The mixtures are calculated as a weighted sum of two materials. Considering μ_1 and μ_2 the linear attenuation coefficient at 80 keV from the NIST database of two materials composing the mixture and α and β the mass fractions. Any $\mu_1 < \mu_{ib} < \mu_2$ in between (ib) linear attenuation coefficient in the image be written

as:

$$\begin{cases} \mu_{ib} = \alpha\mu_1 + \beta\mu_2 \\ 1 = \alpha + \beta \end{cases} \quad (4)$$

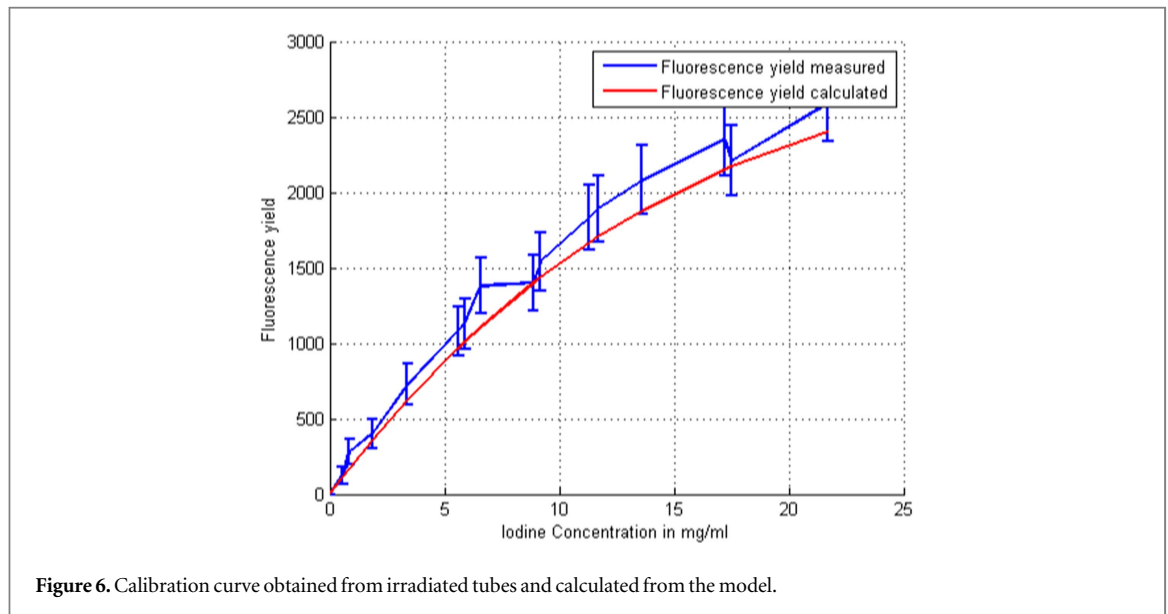


Figure 6. Calibration curve obtained from irradiated tubes and calculated from the model.

Solving the equation leads to:

$$\begin{cases} \beta = \frac{\mu_{ib} - \mu_1}{\mu_2 - \mu_1} \\ \alpha = 1 - \beta \end{cases} \quad (5)$$

The coefficients α and β are then used for each pixels to attribute an extrapolated value of the linear attenuation coefficient at 28.5 keV $\mu_{e,28.5 \text{ keV}}$ as given by equation (6) where are the linear attenuation coefficient of the materials at 28.5 keV from the NIST database.

$$\mu_{e,28.5 \text{ keV}} = \alpha \mu_{1,28.5} + \beta \mu_{2,28.5} \quad (6)$$

The linear attenuation coefficient used at 28.5 keV are $\mu_{tot} - \mu_{\text{Rayleigh}}$. As a matter of fact, including Rayleigh scattering in the linear attenuation coefficient means that a photon that interact through Rayleigh mechanism will not be detected. The 15 cm in radius aperture at the level of the isocenter makes Rayleigh photons detectable by the CZT detector. The tissue attenuation is finally corrected using the extrapolated 28.5 keV CT scan. For each irradiation port the attenuation coefficient is calculated as the mean coefficient in a cone from the isocenter and limited by the size of the active volume area of the CZT detector which represents an average over 10 lines.

2. Results

2.1. Monte-Carlo simulation

The Monte-Carlo simulations provides results that confirm the feasibility of fluorescence detection in the case of a centered tumor. The mean concentration of iodine in the tumor volume is expected to be around 1.95 ± 0.12 mg/ml as measured on 12 patients by Obeid and al [8]. For the simulation, a concentration of 5 mg/ml is used and leads to a SNR of 5.28 as shown in figure 1. It is reasonably assumed that we can detect the iodine concentration in real patient. Building a calibration curve from the Monte-Carlo simulation is

unrealistic because of the low statistics in the small detection volume ($3 \times 3 \times 1$ mm³). As a consequence these simulations show that the detection of iodine on patients is feasible.

2.2. Calibration Curve

Results of the calibration are shown on figure 6 for an irradiated volume of 1.14 cm³ and a 1 s irradiation time. The model described in section 2.2 and the experimental data agree within the error bars for concentrations ranking from 0 to 20 mg/ml.

The calibration curve is bended which is due to the fact that the water absorbs less the photons than the iodine at a given energy. In the case of an equal absorption between the matrix and the analite the fluorescence would have a linear dependance with the analite concentration [19]. The simulated curve is slightly lower than the measured one as it comes from a calculation that only accounts for the primary interactions. Scattered radiation who's influence depends on the photon spectrum and irradiation geometry is not modelled here as its accurate quantification is not accessible analytically. The mean difference between the simulated and measured fluorescence is 15% which might correspond to the influence of the fluorescence emitted after interactions of scattered radiation in the tube. This simulation also allows the visualisation of the relative fluorescence intensity of each pixel and their contribution to the signal (figure 7). It should be noticed that the major part of the signal comes from pixels at the edge of the tube in the direction of the detector and not from the isocenter. This is due to the attenuation of the 80 keV photons inside the tube on one hand and self absorption of 28.5 keV photons within the medium combined with the irradiation geometry on the other hand.

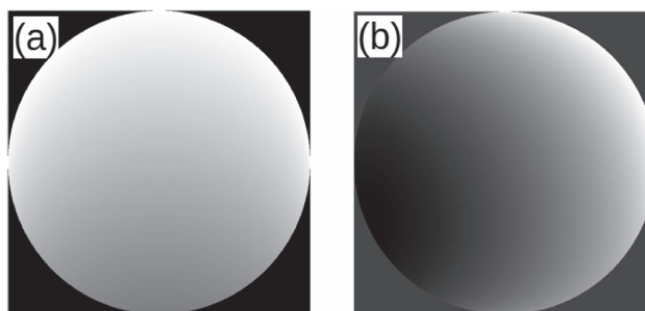


Figure 7. (a) Relative fluorescence isotropic emission intensity in the numerical tube. (b) Relative contribution of each pixel to the measured signal.

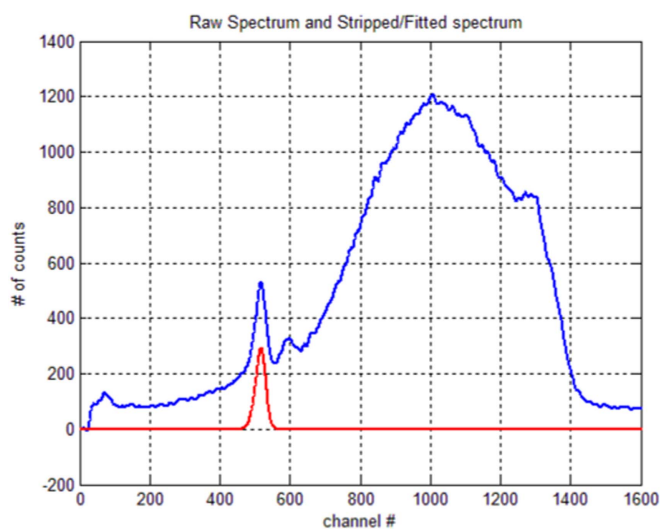


Figure 8. Spectrum detected for one irradiation incidence versus channel number. The blue line is the raw spectrum and the red line is the iodine K_{α} line obtained with background removal.

2.3. Measurement during patient treatment

Each spectrum acquired for each irradiation incidence is shaped like the spectrum provided by figure 8 which is the first one ever recorded in SSRT. The intensity of the K_{α} line depends on the irradiation time and both the distances between the isocenter and the beam entrance point (x_1) and the isocenter to the exit point (x_2).

The red curve on figure 8 is the result of the numerical process to remove the scattered radiation background. The correct fluorescence rate is extracted by fitting the peak with a 2 Gaussians function. The 2 Gaussians function is more appropriate to describe a photoelectric peak from a CZT detector because of its asymmetry due to incomplete charge collection. The content of every channel is then summed to obtain for each irradiation incidence the detected fluorescence rate.

In order to compare the fluorescence rate to the calibration curve, a normalisation procedure has to be applied. In SSRT, each irradiation incidence deliver the same dose to the isocenter. The results of the MC study about the assumption that the fluorescence rate

detected is proportional to the dose at the isocenter are shown on figure 9. The dose and the number of counts are normalised to the maximum measured for tubes filled with 5 mg/ml of iodine. The measured fluorescence and the dose calculated for tubes filled with 5 mg/ml follow the same trend as the brain thickness increases, i.e. the detected fluorescence rate is proportional to the dose to the isocenter. In addition, when normalising to the dose to water, the increase in dose deposition in a 5 mg/ml tube is around 50 percents which corresponds to values found in the litterature (10% increased dose per mg/ml iodine) [8].

Thanks to this calculation, the normalisation procedure becomes easier, irradiation parameters independent, but depends only on the patient geometry. The next step is then to numerically remove the tissue around the tumor by exploiting the CT image acquired with a 80 keV monochromatic beam for centering the patient, and extrapolate the mass attenuation coefficient to their value at 28.5 keV. The first attempt is realized on tubes filled with 5 mg/ml of iodine and the results are shown on the following table:

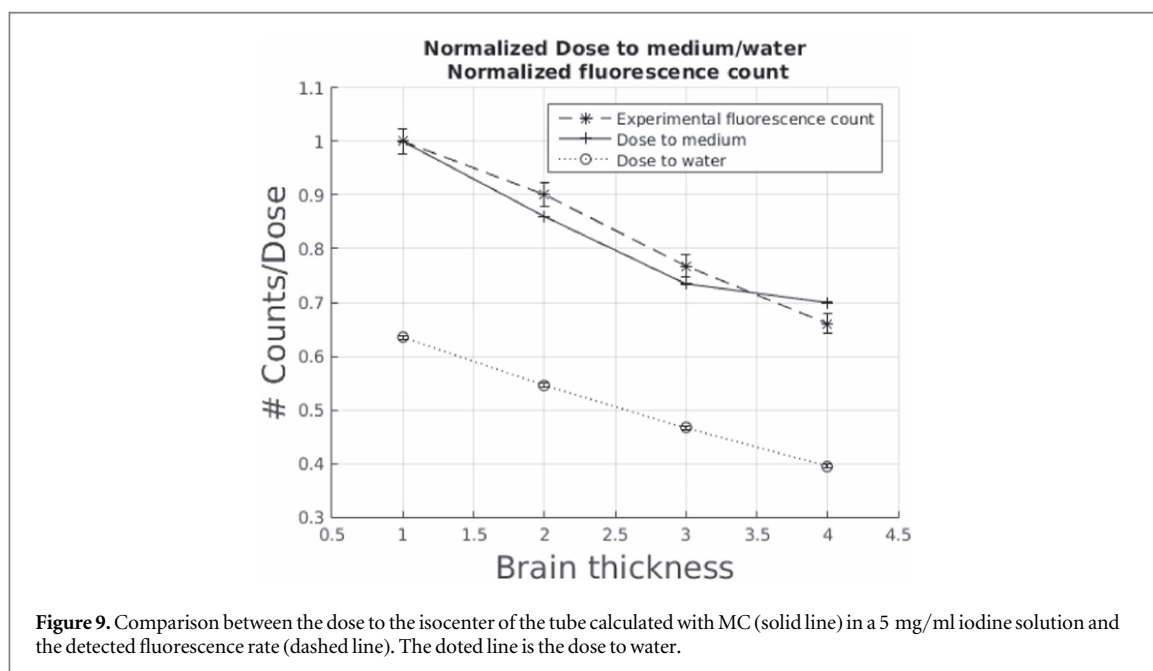


Table 2. Fluorescence normalized to the machine current for a bare tube and corrected for brain attenuation using extrapolation method.

| Irradiation conditions | Raw data /mA/s | Corrected data |
|------------------------|-------------------|-------------------|
| Bare Tube | $52 \pm 1.5\%$ | $52 \pm 1.5\%$ |
| Tube + 1 cm brain | $37.53 \pm 1.8\%$ | $53.53 \pm 1.8\%$ |
| Tube + 2 cm brain | $25.53 \pm 2\%$ | $51.60 \pm 3\%$ |
| Tube + 3 cm brain | $18.01 \pm 2\%$ | $53.80 \pm 3\%$ |
| Tube + 2 cm brain | $13.72 \pm 2\%$ | $51.85 \pm 3\%$ |

In this case of very simple geometry, the extrapolation of the Hounsfield units from a 80 keV CT scan to 28.5 keV allows retrieving the expected fluorescence rate. The brain thickness removal produces fluorescence values in agreement with the data acquired on the bare tube within the error bars as shown in table 2. Finally, the attenuation coefficient extrapolation is tested on a CT scan from a real patient, performed after the irradiation. As described in section 2.3 (figure 4), the 80 keV CT scan is extrapolated to 28.5 keV to obtain a map of linear attenuation coefficient at this energy. The tissue thickness is then removed by acquiring pixels values on the lines from the isocenter to the detector and 10 other adjacent lines which are representative of the aperture of the detector. Figure 10 displays the corrected fluorescence rate versus the irradiation incidence. The procedure is supposed to produce the same number of counts for each irradiation port, but as shown on figure 10, the difference between the calculated fluorescence for the incidence ports can be up to a factor of 10. The additional source of uncertainties can be the detection noise, the error made using the 3 channel method and the standard deviation over the 10 lines in the CT scan and varies between 4% and 15%.

3. Discussion

The results of the MC combined with the analytical study highlight the fact that the iodine fluorescence detection using a CZT detector is achievable. Previous studies [8] found a mean iodine uptake for 5 patients of 1.54 ± 0.19 for one protocol and 1.94 ± 0.12 for an other. But in this case, the iodine uptake is not homogeneous and is ring shaped around what appears to be a necrotic core (figure 4). The signal coming from the edge of the tumor may be averaged because the numerical procedure assumes an emission from the isocenter and finally lowers the iodine concentration retrieval. Moreover, the CT scan being acquired after the irradiation causes the iodine to be partially washed out of the tumor.

The patient specific procedure based on the CT scan can be quantify using the linear attenuation coefficient at 28.5 keV of brain and two types of bones (ICRU-44) [13]. Assuming an error of 10% on the extrapolation of both brain and skull attenuation coefficient, one can calculate the error made once used in the Beer–Lambert law. Considering a 1 cm thick brain slab and a 1 cm thick bone as a combination of 2×1 mm of cortical bone and 8 mm of spongy bone, such error will lead respectively to 3.4%/cm and 16%/cm in difference in the calculated fluorescence rate. It has also been pointed out by Verhaegen *et al* that the uncertainty in the tissue composition could lead to large errors in the dose deposition. Whereas the probability of the Compton effect for different tissues depends only on the electron density, the probability of photoelectric effects depends very strongly on the effective atomic number Z^{3-4} of the tissues [21]. The model used in this paper utilizes artificial mixtures that are correct for high energy photon beams but leads to large fluctuations in the retrieved fluorescence

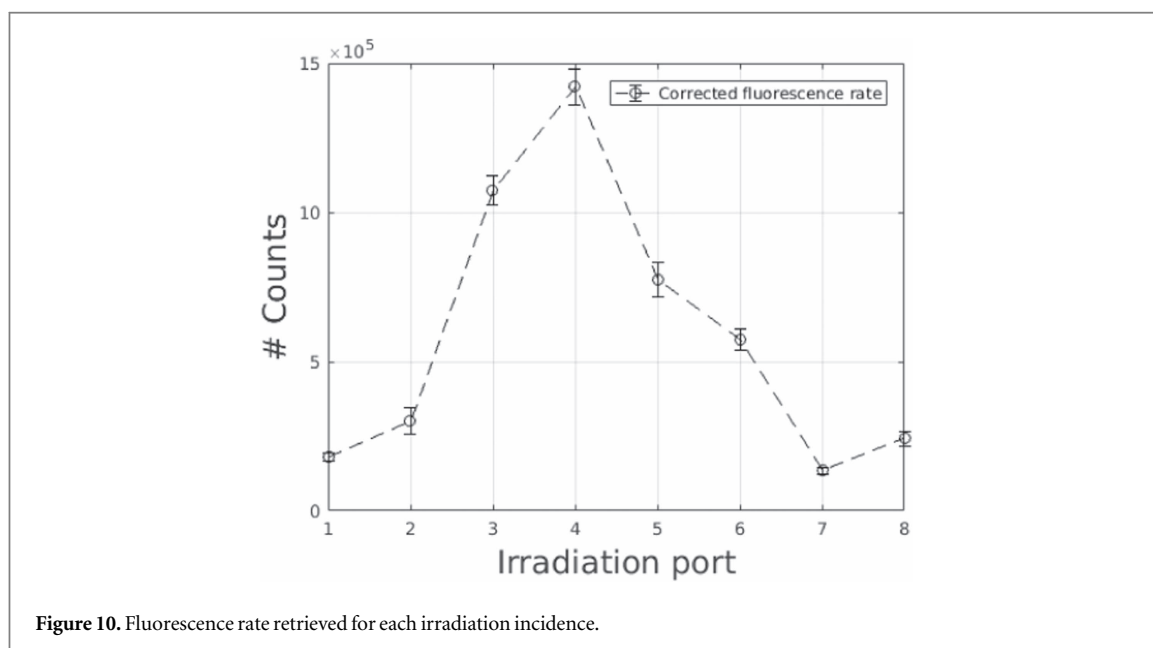


Figure 10. Fluorescence rate retrieved for each irradiation incidence.

rate because the photoelectric effect is responsible for the fluorescence emission. As a consequence the retrieved fluorescence is underestimated due to an overcorrection of the number of photons when large bone thicknesses are involved. Despite difference in the retrieved fluorescence rate, using the calibration curve previously obtained the iodine concentrations are in the range, between 0.1 mg/ml and 0.8 mg/ml (table 3).

The major part of the uncertainties comes from the extrapolation procedure. In the range of energies between 28.5 keV and 80 keV the difference in photon interaction mechanism is huge for materials such as bones. Interfaces (brain/bone etc) are handled by the mean of thresholds applied depending on the pixel values. Those thresholds remain user dependant and can lead to differences in the results.

The improvement of the collimation should suppress the detection of fluorescence photons from above and below the isocenter level, and increase the accuracy of the correction based on one single CT slice at the isocenter level. One advantage of the technique is that the calculation is instantaneous, which is an added value for real *in vivo* detection.

4. Conclusion

This study is a proof of concept of detecting iodine fluorescence emission during a SSRT treatment and is a first step towards *in vivo* dosimetry in SSRT using x-ray spectroscopy. The approach in this paper helped us to point out the quantification issues in the technique. Though sensitive to the material segmentation, the technique proposed here retrieves a rough estimate of the iodine concentration in the tumor instantaneously. A range of iodine concentration ranging from 0.1 to 0.8 mg/ml has been retrieved

Table 3. Caption to table.

| Irradiation port | [I]mg/ml | Δ [I] mg/ml |
|------------------|----------|--------------------|
| 1 | 0.102 | ± 0.008 |
| 2 | 0.170 | ± 0.025 |
| 3 | 0.605 | ± 0.028 |
| 4 | 0.801 | ± 0.034 |
| 5 | 0.430 | ± 0.033 |
| 6 | 0.322 | ± 0.019 |
| 7 | 0.073 | ± 0.007 |
| 8 | 0.138 | ± 0.013 |

compared to the 2 mg/ml expected. Improvements of the collimation should enhance the accuracy of the technique that can become a great added value to the SSRT project in terms of quality insurance.

Acknowledgments

This research was undertaken on the Medical beam-line at the European Synchrotron Radiation Facility, Grenoble, France. The Grenoble Alpes University scientists acknowledge the financial support from LabEx Primes (ANR-11-LABX-0063/ANR-11-IDEX-0007).

ORCID iDs

Dimitri Reynard  <https://orcid.org/0000-0002-2578-1662>

References

- [1] Adam J-F, Elleaume H, Le Duc G, Corde S, Charvet A-M, Tropres I, Le Bas J-F and Estève F 2003 Absolute cerebral blood volume and blood flow measurements based on synchrotron radiation quantitative computed tomography *Journal of Cerebral Blood Flow & Metabolism* **23** 499–512

- [2] Carmeliet P and Jain R K 2000 Angiogenesis in cancer and other diseases *Nature* **407** 249
- [3] Mello R S 1983 Radiation dose enhancement in tumors with iodine *Med. Phys.* **10** 75
- [4] Robar J, Martin M and Riccio S 2004 Tumor dose enhancement using modified photon beams and contrast media *US Patent App.* 10/621,575
- [5] Edouard M, Broggio D, Prezado Y, Estève F, Elleaume H and Adam J-F 2010 Treatment plans optimization for contrast-enhanced synchrotron stereotactic radiotherapy *Med. Phys.* **37** 2445–56
- [6] Rose J H, Norman A, Ingram M, Aoki C, Solberg T and Mesa A 1999 First radiotherapy of human metastatic brain tumors delivered by a computerized tomography scanner (ctrx) *Int. J. Radiat. Oncol. Biol. Phys.* **45** 1127–32
- [7] Edouard M, Broggio D, Prezado Y, Estève F, Elleaume H and Adam J F 2010 Treatment plans optimization for contrast-enhanced synchrotron stereotactic radiotherapy *Med. Phys.* **37** 2445–56
- [8] Obeid L, Deman P, Tessier A, Balosso J, Estève F and Adam J-F 2014 Absolute perfusion measurements and associated iodinated contrast agent time course in brain metastasis: a study for contrast-enhanced radiotherapy *Journal of Cerebral Blood Flow and Metabolism: Official Journal of the International Society of Cerebral Blood Flow and Metabolism* **34** 638–45
- [9] Rust G-F and Weigelt J 1998 x-ray fluorescent computer tomography with synchrotron radiation *Nuclear Science, IEEE Transactions on* **45** 75–88
- [10] Hogan J P, Gonsalves R A and Krieger A S 1991 Fluorescent computer tomography: a model for correction of x-ray absorption *IEEE Trans. Nucl. Sci.* **38** 1721–7
- [11] Takeda T, Wu J W J, Thet-Thet-Lwin T-T-L, Sunaguchi N, Yuasa T, Hyodo K, Dilmanian F A, Minami M and Akatsuka T 2005 Cerebral perfusion imaging of live mice by fluorescent x-ray CT *IEEE International Conf. on Image Processing 2005 3* (OCTOBER) (<https://doi.org/10.1109/ICIP.2005.1530461>)
- [12] Hoffer P B, Jones W B, Crawford R B, Beck R and Gottschalk A 1968 Fluorescent thyroid scanning: a new method of imaging the thyroid I *Radiology* **90** 342–4
- [13] Goldstone K E 1990 Tissue substitutes in radiation dosimetry and measurement, in: ICRU report 44. International commission on radiation units and measurements, USA (1989)
- [14] Bouchet L G, Bolch W E, Weber D A, Atkins H L and Poston J W Sr 1996 A revised dosimetric model of the adult head and brain *The Journal of Nuclear Medicine* **37** 1226
- [15] Berger M J and Estar P 1992 Astar: computer programs for calculating stopping-power and ranges for electrons *Protons, and Helium Ions, NIST Report NISTIR-4999, Washington, DC*
- [16] Fernández J E, Scot V and Sabbatucci L 2015 A modeling tool for detector resolution and incomplete charge collection *X-Ray Spectrometry*. **44** 177–82
- [17] Hall C 2013 Combined x-ray fluorescence and absorption computed tomography using a synchrotron beam *Journal of Instrumentation* **8** C06007
- [18] Elleaume H, Charvet A M, Corde S, Esteve F and Le Bas J F 2002 Performance of computed tomography for contrast agent concentration measurements with monochromatic x-ray beams: comparison of k-edge versus temporal subtraction *Phys. Med. Biol.* **47** 3369
- [19] Van Grieken R and Markowicz A 2001 *Handbook of x-ray Spectrometry* (Boca Raton, FL: CRC Press)
- [20] Schneider W, Bortfeld T and Schlegel W 2000 Correlation between ct numbers and tissue parameters needed for Monte Carlo simulations of clinical dose distributions *Phys. Med. Biol.* **45** 459
- [21] Verhaegen F, van Hoof S, Granton P V and Trani D 2014 A review of treatment planning for precision image-guided photon beam pre-clinical animal radiation studies *Zeitschrift für Medizinische Physik* **24** 323–34

B Flow chart for the Parallelized Penelope

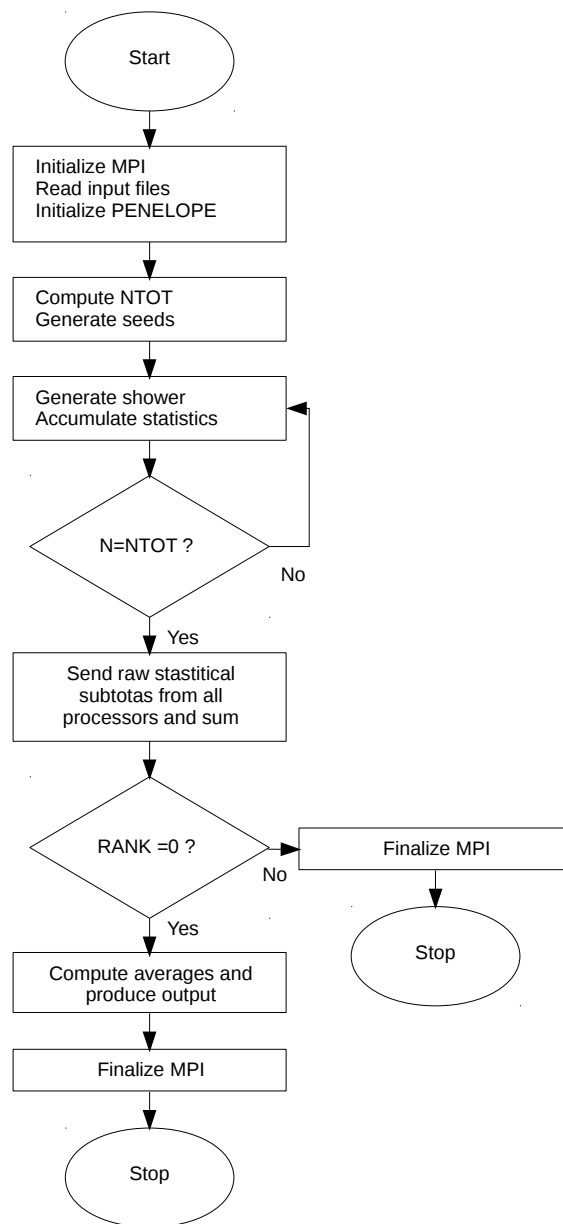


Figure 54: Flow Chart for Parallelized PENELOPE